

Dynamic Models for Liquid Rocket Engines with Health Monitoring Application

by

Paulo César Lozano-Tovar

M.Sc., Physics (1996)

Centro de Investigación y Estudios Avanzados del I.P.N., México

B.S., Physics Engineering (1993)

Instituto Tecnológico y de Estudios Superiores de Monterrey, México

Submitted to the Department of Aeronautics and Astronautics in partial
fulfillment of the requirements for the degree of

Master of Science in Aeronautics and Astronautics

at the

MASSACHUSETTS INSTITUTE OF TECHNOLOGY

June 1998

© Massachusetts Institute of Technology, 1998. All Rights Reserved.

Author
.....
Department of Aeronautics and Astronautics
May 22, 1998

Certified by
.....
Manuel Martinez-Sanchez
Professor of Aeronautics and Astronautics
Thesis Supervisor

Certified by
.....
Rami Mangoubi
Senior Member of the Technical Staff, C. S. Draper Laboratory
Thesis Co-supervisor

Accepted by
.....
Jaime Peraire
Associate Professor
Chairman, Department Graduate Committee

JUL 08 1998

LIBRARIES

Abstract

Dynamic models for liquid rocket engines are developed. The particular case of the Space Shuttle Main Engine (SSME) is considered and reviewed, taking as a reference the thermodynamic model introduced by Rocketdyne, subcontractor in charge of the SSME production. Most of the possibilities involved in the design of dynamic models are shown from first principles. Rotordynamic models are also presented with emphasis in rotor-casing vibrational response. An overview of health monitoring (i.e., monitoring of the general operational condition of the engine) based on such models is introduced as well, stressing the importance of such analysis in reusable launch vehicle's (RLV's) engine development.

Acknowledgments

This work is dedicated to my parents, Alfredo and Vicky, for their unconditional support throughout my life, their love and strength allowed me to grow and reach for my dreams, reach for the stars; to my brother Jorge and my sister Wendy, you are poetry, you are passion, thank you for permitting me to take a piece of that; to Juan and Anabella and their little children, Juanito and Bellita, my four soul companions; to the Schulz family, for giving me the greatest gift of all; and specially to my wife, Marcela, for allowing her happiness and tenderness enter into my life, you are my motive and inspiration.

Special thanks to my advisor, Manuel, for his patience along this time of study and reflection, your way of teaching and working is an inspiration for those who crave to improve this world. Thanks also to Rami Mangoubi for his help and consideration. It would be impossible the include the names of all my friends and colleagues at MIT who were always there to nurture fabulous discussions and ideas, thanks to them all.

Finally, I am particularly grateful with the National Council for Science and Technology in México, and the Charles Stark Draper Laboratory in Cambridge, for providing me with financial support to complete my master's graduate program at MIT.

*Es verdad, es verdad,
que no hemos venido a vivir a este mundo,
llegamos a dormir, a soñar...*

*It is true, it is true,
that we came to this world not to live,
but we came to sleep, to dream...*

- Nezahualcoyotl -

Table of Contents

Chapter 1: INTRODUCTION.....	9
Chapter 2: SSME DESCRIPTION	13
Chapter 3: SSME THERMODYNAMIC MODEL	17
3.1 Generalized Dynamic Equations.....	18
3.1.1 Rotational Dynamics	18
3.1.2 Inertia Under Pressure Fluctuations	19
3.1.3 Fluid Capacitance Under Pressure Variations	20
3.1.4 Fluid Capacitance Under Density Variations at Constant Pressure.....	21
3.1.5 Energy Balance in Heat Exchangers	21
3.1.6 Heat Transfer Temperature Equations	22
3.1.7 Time Delay Equations	23
3.2 Complete Model.....	24
3.2.1 High Pressure Fuel Turbopump Speed	25
3.2.1.1 HPFTP Turbine Torque Analysis	26
3.2.1.2 Fuel Preburner Combustion Gas Characteristics	38
3.2.1.3 HPFTP Turbine Mass Flow Rate Calculation	41
3.2.1.4 HPFTP Additional Parameters	46
3.2.1.5 HPFTP Centrifugal Pump Analysis	47
3.2.2 High Pressure Oxidizer Turbopump Speed	51
3.2.2.1 HPOTP Turbine Section	52
3.2.2.2 HPOTP Turbine Mass Flow Rate	55
3.2.2.3 HPOTP Additional Parameters	56
3.2.2.4 HPOTP Pump Section	56
3.2.2.5 HPOTP Boost Pump Section	58
3.2.3 Low Pressure Fuel Turbopump Speed	59
3.2.3.1 LPFTP Turbine Section	61
3.2.3.2 LPFTP Turbine Mass Flow Rate	63
3.2.3.3 LPFTP Pump Section	64
3.2.4 Low Pressure Oxidizer Turbopump Speed	66
3.2.4.1 LPOTP Turbine Section	67
3.2.4.2 LPOTP Pump Section	69
3.2.5 HPOTP Boost Pump Oxidizer Flow Rate	70
3.2.6 Main Oxidizer Valve Flow Rate	73
3.2.7 Fuel Preburner Oxidizer Flow Rate	77
3.2.8 Oxidizer Preburner Oxidizer Flow Rate	79
3.2.9 Coolant Liner Inlet Flow Rate	80
3.2.10 Coolant Liner Outlet Flow Rate	82
3.2.11 Fuel Preburner Fuel Flow Rate	83
3.2.12 Oxidizer Preburner Fuel Flow Rate	84
3.2.13 Main Combustion Chamber Heat Exchanger Fuel Flow Rate	85
3.2.14 Nozzle Heat Exchanger Outlet Fuel Flow Rate	87
3.2.15 Nozzle Heat Exchanger Outlet Fuel Flow Rate	88
3.2.16 Nozzle Heat Exchanger Bypass Fuel Flow Rate	90
3.2.17 LPOTP Pump Inlet Oxidizer Flow Rate	91
3.2.18 LPOTP Hydraulic Turbine Flow Rate	93
3.2.19 Fuel Preburner Augmented Spark Igniter Flow Rate	95

3.2.20	Oxidizer Preburner Augmented Spark Igniter Flow Rate	96
3.2.21	Main Combustion Chamber Augmented Spark Igniter Flow Rate	96
3.2.22	Preburners Oxidizer Supply Line Pressure	97
3.2.23	Oxidizer Preburner Pressure	99
3.2.24	Fuel Preburner Pressure	100
3.2.25	Coolant Liner Pressure	101
3.2.26	Preburners Fuel Supply Line Pressure	102
3.2.27	LPOTP Pump Inlet Pressure	103
3.2.28	Fuel Injector Pressure	104
3.2.29	Main Combustor Chamber Pressure	105
3.2.30	Fuel Density at the Main Combustion Chamber Heat Exchanger	109
3.2.31	Fuel Density at the Nozzle Heat Exchanger	110
3.2.32	Fuel Specific Internal Energy at the MCC Heat Exchanger	111
3.2.33	Fuel Specific Internal Energy at the Nozzle Heat Exchanger	114
3.2.34	Main Combustor Chamber Heat Exchanger Hot Wall Temperature	116
3.2.35	Main Combustor Chamber Heat Exchanger Cold Wall Temperature	117
3.2.36	Nozzle Heat Exchanger Hot Wall Temperature	118
3.2.37	Nozzle Heat Exchanger Cold Wall Temperature	119
3.2.38	Main Fuel Injector Flow Rate	119
Chapter 4: SSME ROTORDYNAMIC MODELING	123
4.1	Synchronous or Forced Vibration.....	124
4.2	Sub-synchronous or Self-excited Vibration	125
4.3	Calculation of Critical or Natural Frequencies	128
4.3.1	HPFTP Simplified Rotor Model	129
4.3.2	Lagrange Formulation of the Simplified Dynamic Problem.....	130
4.3.2.1	Calculation of the Potential Energy in the Simplified Model	131
4.3.2.2	Calculation of the Kinetic Energy in the Simplified Model	132
4.3.3	Calculation of the Normal Modes of Vibration	133
4.3.4	Numerical Calculation	135
Chapter 5: HEALTH MONITORING	139
5.1	Historical Context	140
5.2	Health Monitoring for Reusable Launch Vehicles	141
5.3	Failure Detection and Isolation	143
5.4	The Use of Liquid Rocket Engine Vibration Data	147
Chapter 6: CONCLUSIONS	159
Appendix A.	Glossary of useful abbreviations	161
Appendix B.	Steady State Values from the SSME Thermodynamic Model	163
Appendix C.	State Variables in a Simulated Throttling Sequence	165
Appendix D.	Characteristic Times (approx.) for the SSME Dynamic Model	171
Appendix E.	Stability Criteria for the Problem of the Simple Disc	173
References	177

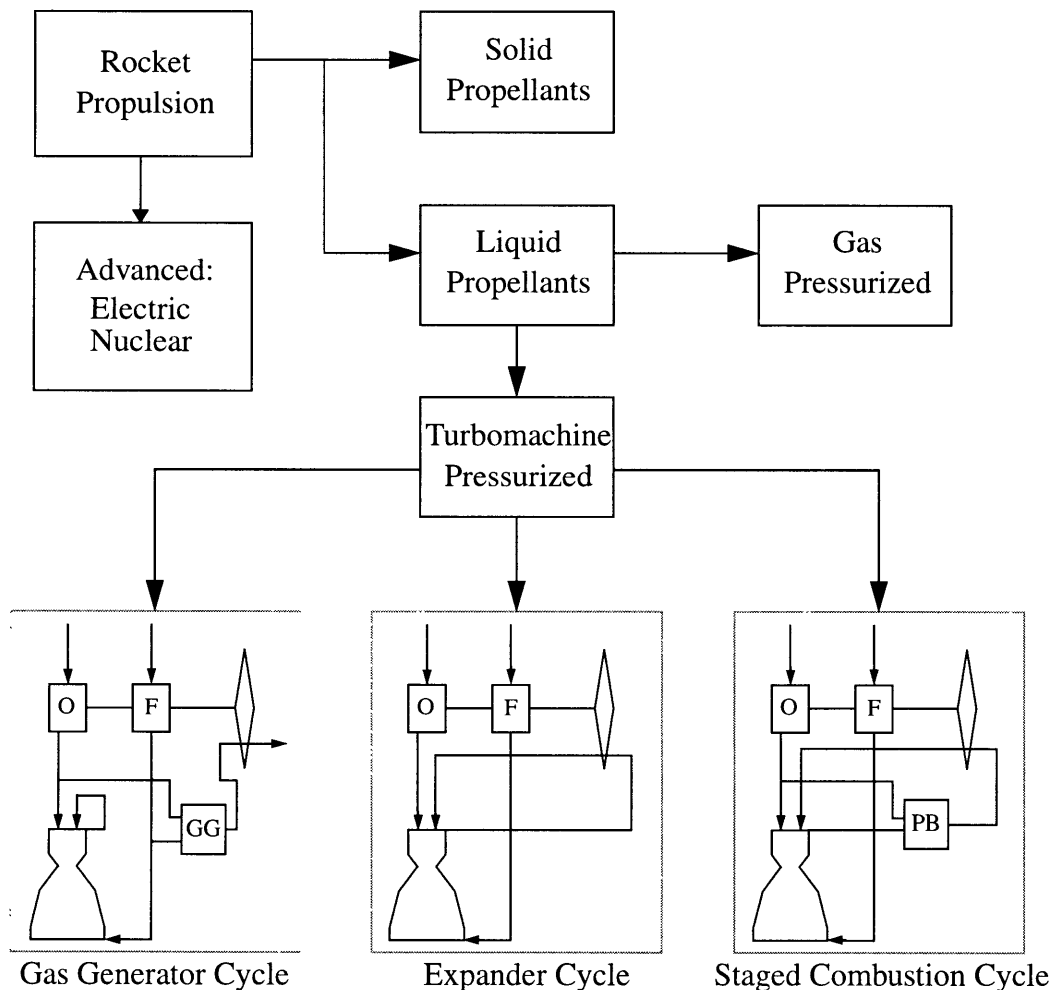
Chapter 1

Introduction

Rocket propulsion is acknowledged as one of the most basic applications of energy conversion; maybe that is the reason for its invention many centuries ago in China, where small, mostly ornamental rockets were found to be a simple by-product powered by the then newly discovered gunpowder. Rocket simplicity can be deceiving, however, as hundreds of years would need to pass until a relatively large propulsion system could be developed. In fact, modern rocket age began in the early 20th century with pioneer researchers, such as Robert Goddard (1882-1945) who constructed and operated the first rocket that used liquid propellants in 1926, or Konstantin Tsiolkovsky (1857-1935) who published for the first time the basics of rocket motion in 1903 and the theory of multi-stage rockets in 1929, and always dreamed about the possibilities for human kind to explore places beyond Earth; one of Tsiolkovsky's most famous quote is, "Earth is the cradle of humanity, but one cannot remain in the cradle forever." Beyond them, several research groups created associations which were involved in rocket development focused on space exploration; with time, most of them disappeared because of the lack of financial resources. Governments were not fully convinced of the rocket utility until war superiority became an issue. During the final years of World War II, a group of german rocket scientists, led by Werner von Braun (1912-1977) designed and constructed the first heavy launch vehicle, which by the way was also the first line production rocket, the A4, later known as the V2. Its objective was the long range bombarding of allied positions, mainly

on the United Kingdom. Many key technologies concerning launch vehicles were rapidly developed for this project. Fortunately, the war was over before a fully scale development of Hitler's secret "vengeance" weapon was achieved; overall, the impact of the V2 in the final result of the war was negligible; however, not small was the advancement of knowledge in rocket propulsion systems. Von Braun's group surrendered to the allied force and moved to the US where they transformed in the focus of the new space program. The V2 development installations located in Peenemunde were occupied by the russian army, acquiring enough knowledge from there to begin a space program by their own.

The following diagram shows, in a general way, the different types of rocket propulsion systems available today:



Solid propellant engines or “rocket motors” are the most basic propulsion system: a solid compound burns, creating hot gases inside a container opened at one extreme, causing a differential pressure that generates thrust. Once the propellant is ignited, burning cannot be stopped, unless the opposite extreme of the container is opened as well, reducing its gas pressure below the solid fuel combustion limit. Rocket motors cannot be throttled and are difficult to control; they are generally used to assist large vehicles to achieve an initial high velocity or to boost satellites from one orbit to another. They can only be fired once in a mission. The use of liquid propellant engines, on the contrary, provides more flexibility in their applications and have, in general, better performance. These type of engines can be designed to be throttled and fired more than once in each mission. In these engines, liquid propellants are mixed and burned in a controlled way in a combustion chamber, the thrust generated by these engines depend upon the quantity of fuel injected in the chamber along with their pressure. In this way, liquid engines can be categorized also by their pressurization method; the most basic form of pressurizing is using the pressure inside an independent container (gas pressurization) to literally “push” the propellants into the chamber injectors. This type of pressurization is mainly used in satellites and other spacecraft for station keeping purposes. If high thrust is required, then gas pressurization is not enough, in its place, specially built turbomachinery must be used to increase the pressure of the propellants prior to injection into the chamber. There are several thermodynamic cycles which perform such task; among the most popular are the gas generator, the expander and the staged combustion cycles [1, 2, 10].

Most launch vehicles in use today have, as their main propulsion system, a turbomachine pressurized liquid propellant rocket engine, which is, precisely, the focus of attention for this thesis. Our main objective is to reach a physical description of such engine while at the same time contributing with the required guidelines for the development of dynamic models which can be used for simulation purposes or, as it will be seen in the following chapters, as analytical approaches for real operational problems such as the ones involving safety and reliability. The principal reference for this work will be a thermodynamic model developed by Rocketdyne [3] for the Space Shuttle Main Engine (SSME). The SSME is maybe the most complex rocket engine in use today; we believe that a close inspection of each one of its components and their incorporation into a dynamic model derived from first principles results in a valuable tool that could help in the design or

adaptation of models for any other liquid rocket engine, including those to be used in the next generation of Reusable Launch Vehicles (RLVs), such as the XRS-2200 Linear Aerospike engine for the X-33 single-stage-to-orbit (SSTO) demonstrator.

A description of the SSME is provided in chapter 2, while its thermodynamic model is completely developed and compared with [3] in chapter 3. Chapter 4 involves the elaboration of rotordynamic models for the SSME's HPFTP turbomachine; as we will see, the information obtained from this other type of model will prove very useful to determine the best operational conditions for the engine in such a way that dynamic instabilities are avoided. Finally, in chapter 6, the models developed will be applied into a health monitoring (HM) scheme in which the state variables of the engine (obtained from the models) are observed via sensors and used to determine if degradation of the propulsion system occurs. Several strategies and algorithms for this purpose are reviewed and analyzed, in particular, failure detection and isolation (FDI) schemes are considered.

Appendix A contains a list of useful abbreviations used along this work.

Chapter 2

SSME Description

The overall design and development of the SSME in the mid 70's represented a huge leap in turbomachinery design and general rocket engineering. Before the SSME began operations, rocket engines were functioning with performance levels by far below those of the new engine. Since then, the SSME has been considered as one of the pieces of machinery with the highest power density ever built; each one delivers an average of 410,000 lb of thrust and achieves a main combustor chamber (MCC) pressure of 3,200 psi. The Space Shuttle makes use of three SSMEs as its main propulsion system for lift-off with the aid of a pair of 2.9 million lb thrust solid propellant motors. The SSMEs are fired approximately for eight and a half minutes until shut down occurs and the secondary propulsion (OMS - Orbital Maneuvering System) system of the orbiter inserts the vehicle in the desired circular orbit. The propellants used by the SSME are cryogenic hydrogen (LH) and oxygen (LOX), both kept in their liquid phase with careful insulation inside the orbiter's external tank. The tank itself provides the required pressure rise for the initial flow of propellants in order to start the ignition sequence. Once working, it has the ability of being throttled almost in a continuous way from a minimum power level of 65% rated power level (RPL) to a maximum of 109% RPL.¹

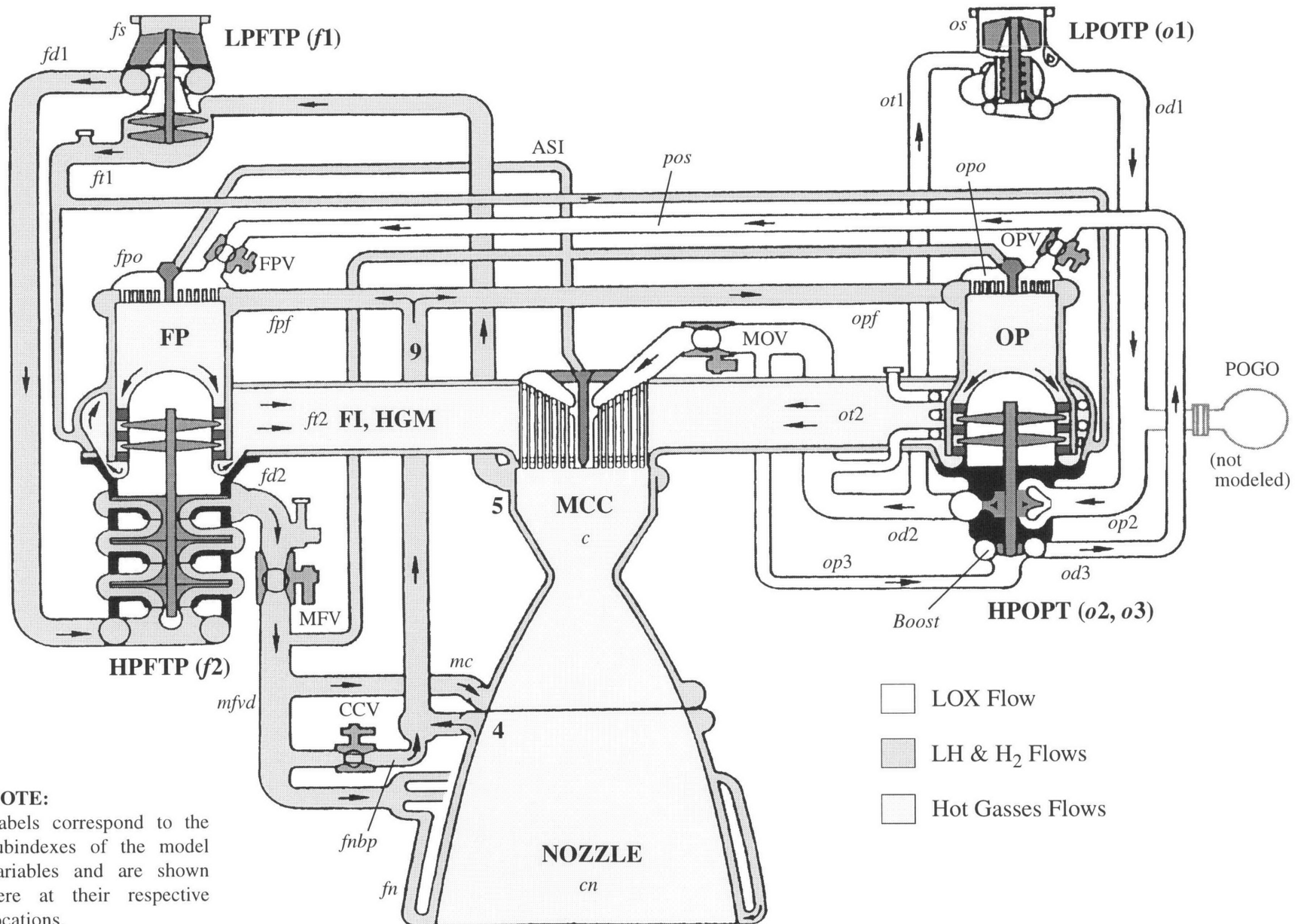
1. It however has been recently tested [13] at lower power levels that range from 17 to 50% RPL.

The combustion of propellants in the SSME is made in two serial type stages (Staged Combustion Cycle). In the first, a relatively small amount of LOX and almost all of the LH are diverted into two preburners. The combustion products are then used to drive the turbines which in turn drive the High Pressure Fuel Turbopump (HPFTP) and the High Pressure Oxidizer Turbopump (HPOTP). At this point the gases have suffered an expansion in their way through the turbines and therefore a decrease in pressure. In the second stage, these LH rich gases are injected into the MCC where they mix with the rest of the LOX and completes the combustion. The Staged Cycle provides the maximum performance since all of the combustion products are ultimately used for thrust generation in the MCC at the cost of operating the turbopumps at extremely high pressures given by the MCC pressure plus the pressure drops in turbines, injectors, pipes, etc.

In the design stage, it was found that the pressure requirements of the SSME were better covered with the use of four turbopumps. Two of them (LPFTP and LPOTP) increase the pressure head from the LH and LOX tanks, thus minimizing structural and weight concerns about the tanks and giving an adequate inlet working pressure for the two turbopumps (HPFTP and HPOTP) that provide the high pressures needed. **Figure 1** shows a simplified flow schematic of the SSME.

Control of the combustion process inside the SSME is achieved by the actions of five hydraulic valves. While in the ignition sequence phase (~4 sec), these valves actuate in a carefully predetermined fashion in order to provide a correct engine start-up. Once this phase ends, the Main Oxidizer Valve (MOV), the Main Fuel Valve (MFV) and the Chamber Coolant Valve (CCV) remain working in a scheduled way, while the Oxidizer Preburner Valve (OPV) and the Fuel Preburner Valve (FPV) enter in a closed-loop operation mode which control the thrust level and maintain the mixture ratio of 6:1 in the MCC. These valves operate with instructions from the SSME Controller which is a dual-redundant electronic device whose inputs are sensor measurements from the engine and commands from the shuttle computers. For a more complete outline of the SSME components and functioning, the reader is encouraged to review references [1] and [2].

FIGURE 1. Flow Schematic of the SSME



Chapter 3

SSME Thermodynamic Model

The dynamics of the SSME are governed by the interaction of a relatively large number of physical variables. Each one of these quantities represents inputs and outputs from all the subsystems and components of the engine. The SSME flow schematic of **Figure 1** can help us to understand the potential degree of complexity of these interactions.

The subsystems which dominate the dynamic behavior of the engine are, in order of increasing power density, the low pressure oxidizer turbopump (LPOTP), low pressure fuel turbopump (LPFTP), high pressure oxidizer turbopump (HPOTP) and the high pressure fuel turbopump (HPFTP). Besides this set of four turbomachines, the dynamics of the engine is complemented with pipes, valves, heat exchangers and so on.

The SSME dynamic model is described in Rocketdyne's documentation [3]. The core of this model is a set of 38 equations which need to be solved for 38 physical variables of the engine (pressures, temperatures, speeds, etc.)

In [3] the equations appear in a purely descriptive manner, there is no (or at most very little) insight on the physical phenomena that occurs in the engine. Each one of the equations includes at least one constant coefficient. Only their values are included in [3], and the origin of most of them is not clarified.

The first step to derive the SSME dynamic model from first principles will be to group and generalize the kind of equations to be used. It will be seen that almost all of the dynamics can be described in terms of these general equations. After that, those generalized equations will be applied to a specific subsystem of the engine, in this way their final form can be found and the coupling will become evident.

3.1 Generalized Dynamic Equations

There are seven types of dynamic equations to be considered:

1. Rotational dynamics of the turbopumps
2. Equations expressing the liquid inertia under pressure difference variations (analogous to inductance in electric circuits.)
3. Equations expressing the ability of cavities to store fluid due to its compressibility under pressure fluctuations (analogous to capacitive effects.)
4. Similar to type 3, but the effect is noted under density variations at constant pressure.
5. Energy balance equations for the heat exchanger elements of the engine.
6. Heat transfer temperature equations.
7. Equations that indicate a time delay between the change in the value of a variable and its recognition as a state variable.

These equations depict the most general form of any liquid propellant rocket engine dynamic model. Here we will present their derivation.

3.1.1 Rotational Dynamics

There are four equations in the model that describe the rotational dynamics of the engine; one for each turbopump. The following is the general form of this equation. If I_{tp} is the moment of inertia of the rotor, τ_t the torque produced by the turbine, and τ_p the torque absorbed by the pump, then the angular velocity Ω can be found after solving

$$I_{tp} \frac{d\Omega}{dt} = \tau_t - \tau_p \quad (1)$$

3.1.2 Inertia Under Pressure Fluctuations

This type of equation is just another application of Newton's second law. Take, for instance, a pipe of length L and cross section A , as the one shown in **Figure 2**. At the inlet of this pipe we have a pump discharging fluid at a pressure P_d the pipe has a mean pressure P_{pipe} . The flow through the pipe is not perfectly smooth, frictional forces in its interior cause a total pressure drop of $\lambda \left(\frac{1}{2} \rho v^2 \right)$, where ρ and v are the fluid density and velocity, and λ is a pressure loss coefficient which in general can be put in the following form (see, for example, ref. [8])

$$\lambda = f \frac{L}{D} \quad f = \frac{0.316}{Re^{0.25}} \quad Re = \frac{\rho v D}{\mu} \quad (2)$$

where D , f , Re and μ are the pipe diameter, a friction coefficient (turbulent flow), the Reynolds number and the fluid viscosity, respectively. In particular, λ is of order unity for the internal flows of the SSME.

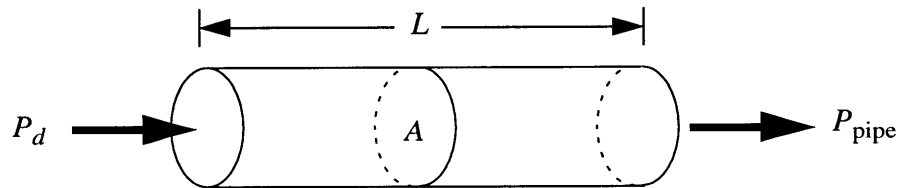


FIGURE 2. Pipe Fed by Pump

Due to the pressure gradient and the frictional term, there is a net force acting on the fluid

$$F_{\text{net}} = ma = (\rho A L) \frac{dv}{dt} = A \left(P_d - P_{\text{pipe}} - \frac{\lambda}{2} \rho v^2 \right) \quad (3)$$

From the continuity equation, the flow rate inside the pipe is $\dot{m} = \rho v A$, therefore we can write (3) as

$$\left(\frac{L}{A}\right)\frac{d}{dt}\dot{m} = P_d - P_{pipe} - \frac{\lambda}{2\rho A^2}\dot{m}^2 \quad (4)$$

3.1.3 Fluid Capacitance Under Pressure Variations

Suppose that our same pipe of **Figure 2** receives fluid flow at a rate \dot{m}_{in} from the pump, and discharges at one or more different places, each one of these with outflow $\dot{m}_1, \dot{m}_2, \dots$

In this way, we have a net inflow given by $\sum \dot{m} = \dot{m}_{in} - \dot{m}_1 - \dot{m}_2 - \dots$, therefore

$$\frac{dm}{dt} = \frac{d}{dt}(\rho A L) = \frac{d}{dt}(\rho V) = \sum \dot{m} = \dot{m}_{in} - \dot{m}_1 - \dot{m}_2 - \dots \quad (5)$$

Although the fluid discharged by the pump is a liquid (as in the SSME pumps), it still has finite compressibility (κ) whose effects become more appreciable as the pressure gradients increase to large values, which is the case of the turbomachinery we are dealing with. From the definition of compressibility

$$\kappa = \frac{1}{\rho} \frac{d\rho}{dP} \quad (6)$$

If we now consider that the volume V remains constant under the pressure fluctuations, then we can write

$$\frac{d}{dt}(\rho V) = V \frac{d\rho}{dt} = \kappa(\rho V) \frac{dP}{dt} \quad (7)$$

Finally, we can rewrite (5) as

$$\kappa(\rho V) \frac{dP}{dt} = \sum \dot{m} \quad (8)$$

3.1.4 Fluid Capacitance Under Density Variations at Constant Pressure

Some of the dynamics of the SSME are more sensitive to density variations than to pressure variations, this is true specially when we deal with heat transfer phenomena inside the chamber and nozzle walls. In any case, this type of equation is essentially the same as equation (5) considering that the volume V remains unchanged

$$V \frac{d\rho}{dt} = \sum \dot{m} \quad (9)$$

3.1.5 Energy Balance in Heat Exchangers

An important part of the dynamics in the turbomachinery deals with properties of gases used on heat transfer processes in the main heat exchangers (Nozzle and MCC). **Figure 3** shows a simplified diagram of the fluid flow between the walls of the heat exchanger.

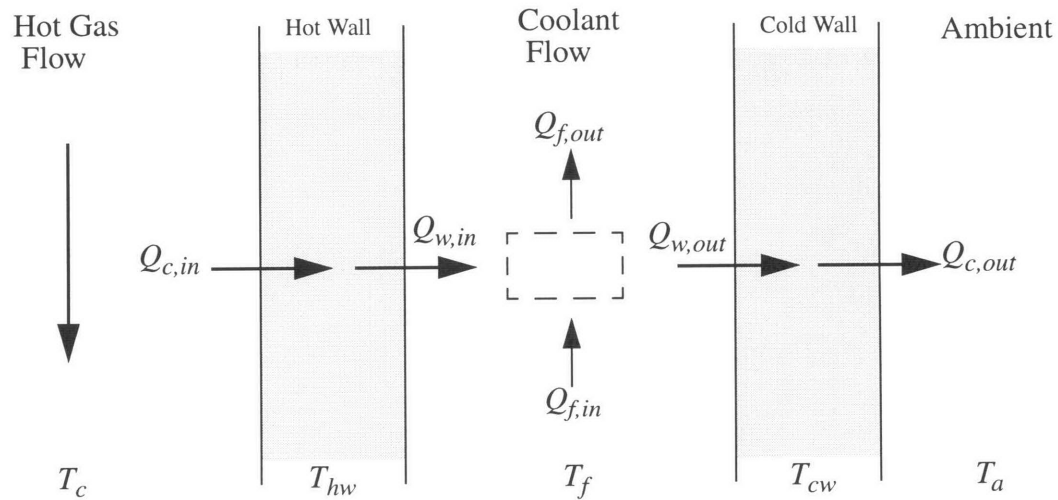


FIGURE 3. Heat Exchanger Fluid Flow

Let us focus our attention in the coolant fluid contained inside the cavity (of volume V) between the walls. Following from the first law of thermodynamics

$$\Delta U = Q - W \quad (10)$$

where Q is the heat absorbed by the fluid, W the mechanical work done by it and ΔU is the change in its internal energy. In terms of change rates, we can write the first law as

$$\frac{dU}{dt} = \dot{Q} - \dot{W} \quad (11)$$

Since there is no mechanical work done by the coolant (the volume remains constant, or at most there is just very little change due to the high pressures involved), equation (11) can be written as

$$\frac{dU}{dt} = m \frac{du}{dt} = \rho V \frac{du}{dt} = \dot{Q} \quad (12)$$

where we have made the approximation of constant density¹, and u is the specific internal energy of the fluid. If h is the specific enthalpy carried by the fluid, then the heat flow rate carried by the system is $\dot{Q}_f = \dot{m}h$. In this way, a simple heat flow balance for the fluid inside the dashed square in **Figure 3** gives

$$\rho V \frac{du}{dt} = \dot{Q}_{w,in} - \dot{Q}_{w,out} + (\dot{m}h)_{in} - (\dot{m}h)_{out} \quad (13)$$

where \dot{Q}_w is the heat flow rate between the walls and the coolant fluid.

3.1.6 Heat Transfer Temperature Equations

These kind of equations are the mathematical description of transient heat transfer phenomena inside the metal walls of the engine. Again, from the first law of thermodynamics (11), assuming that any volume change is negligible as to make the net work equal to zero, we have

$$dQ = dU = mc_v dT \quad (14)$$

1. At first this approximation appears a bold one. If we introduce variable density given by equation (9) into (13) the net result after solving the SSME dynamic model is a negligible difference in the calculated specific internal energy at a relatively greater computational cost. It seems reasonable to make this assumption for simplicity purposes only.

where m is the (effective) mass of the wall and c_v the specific heat of the wall material. Referring to **Figure 3**, none of the surfaces of the hot wall is insulated, therefore there is a net heat flux given by $\dot{Q}_{c, in} - \dot{Q}_{w, in}$. Writing (14) in terms of time increments

$$\frac{dQ_{net}}{dt} = mc_v \frac{dT_{hw}}{dt} = \dot{Q}_{c, in} - \dot{Q}_{w, in} \quad (15)$$

So we can calculate the average transient hot wall temperature as

$$\frac{dT_{hw}}{dt} = \frac{1}{mc_v} (\dot{Q}_{c, in} - \dot{Q}_{w, in}) \quad (16)$$

3.1.7 Time Delay Equations

Some of the variables used in the coupled dynamic model of the SSME do not have an immediate physical response to changes in the states of other variables. This delay can be categorized as a first order time lag.

Say that one of these variables is the mass flow rate through a narrow long pipe. There is a certain amount of time ϵ elapsed since the original signal \dot{m}_o is generated at one end of the pipe and is recognized as the output \dot{m} at the other end where it becomes the new state variable used in the coupled dynamic model. Intuitively, this time shift is such that the following relation applies at any given time t

$$\dot{m}_o(t) = \dot{m}(t + \epsilon) \quad (17)$$

Substracting in each side the output signal $\dot{m}(t)$ at time t and dividing by ϵ

$$\frac{\dot{m}_o(t) - \dot{m}(t)}{\epsilon} = \frac{\dot{m}(t + \epsilon) - \dot{m}(t)}{\epsilon} \quad (18)$$

If the time delay ε is small enough (as is likely to be), then the rhs of (18) can be approximated to its limit as ε approaches zero, which is the definition of the time derivative of the mass flow rate, therefore we can write it as

$$\frac{d}{dt}\dot{m}(t) = \frac{1}{\varepsilon}(\dot{m}_o(t) - \dot{m}(t)) \quad (19)$$

3.2 Complete Model

The seven types of equations of section 3.1 represent the most general case in the engine dynamics. Little coupling between them can be observed in their current form, however each one of their terms has a potential dependence on a considerable number of variables from the rest of the 38 equations involved in the SSME complete model. These dependences are obtained by a systematic analysis of each one of the components of the engine and translation of their function into equations that can be arranged in the form already described. The result is a somewhat complicated mathematical model comprised of 38 coupled variables. In the following sections we will try to make a derivation of each one of these equations.

In order for us to find the actual numerical values of the coefficients that will appear in the derived equations we would need a large amount of information about the engine configuration. Obtaining such information is difficult and the effort for doing so is secondary once the equations have been derived correctly. Therefore, numerical substitutions will be applied only to those components for which numerical data were available; these substitutions, however, will help us to verify the validity of the assumptions made to find the final form of the equations involved.

Appendix B contains a table of the steady state values for the 38 state variables plus a number of other interesting variables as computed with the complete model for different power levels. **Appendix C** shows the plots for the 38 state variables on a typical simulated sequence where the throttle is varied from 100% down to 65%, back up to 109% and down again to 100% RPL. The response times of the SSME dynamic equations were estimated

as well and are shown in **Appendix D**. These characteristic time constants are based on a steady state configuration obtained at 100% RPL. It is interesting to note that in general, the dynamics involved in the SSME thermodynamic model are quite fast.

3.2.1 High Pressure Fuel Turbopump Speed (Ω_{f2})

It seems to be logical to begin the analysis of the SSME with the HPFTP since it represented at the moment of its conception a unique breakthrough in the engineering of liquid rocket pressurization systems, no other engine has had the power density achieved by the HPFTP and because of the complexity involved on its design and development we will consider it in the first place. Furthermore, we have almost all the data needed to make numerical substitutions for the HPFTP and therefore we will be able to compare our derivation with that of [3]. The rotational speed of the turbopump shaft can be calculated using a type 1 equation:¹

$$I_{f2} \frac{d\Omega_{f2}}{dt} = \tau_{ft2} - \tau_{fp2} \quad (20)$$

where

I_{f2} is the moment of inertia of the HPFTP rotor (lbf-in-sec²)

Ω_{f2} is the angular velocity of the HPFTP shaft (rad/sec)

τ_{ft2} is the torque generated by the 2-stage HPFTP axial-flow turbine (lbf-in)

τ_{fp2} is the required torque of the 3-stage HPFTP centrifugal-flow pump (lbf-in)

When dealing with turbomachinery analysis, notation and conventions become important to reduce as much as possible the confusion factor. We have tried to follow the same notation as in [6] for the turbine analysis.

1. One pertinent note about units. The use of metric units would be preferable in the present discussion, however industry standards in the US are still using english engineering units and there is no indication that they will change their standards, at least in the near future. Anyway, with the proper use of conversion factors, metric units can be easily used as well.

From [4], we extracted the value for I_{f2}

$$I_{f2} = \frac{1}{0.3338} \text{ lbf-in-sec}^2$$

Rocketdyne in [3] use a value in the denominator of 0.3087, which is quite close to ours. The next step is to estimate the other two terms of the equation, we will begin with the torque generated by the turbine.

3.2.1.1 HPFTP Turbine Torque Analysis

First of all, let us define a nondimensional quantity usually called *velocity ratio*

$$v_r = \frac{u}{C_o} \quad (21)$$

where u is the tangential velocity of the rotor (in/sec) and C_o is the *spouting* velocity, which is defined as the velocity corresponding to an isentropic expansion from inlet total to exit static conditions across the turbine.

In this kind of problems, the sum of fluid enthalpy and kinetic energy appears frequently; this is the reason of considering it as a single quantity called *total* or *stagnation* specific enthalpy (per unit mass)

$$h' = h + \frac{1}{2}v^2$$

The stagnation or total enthalpy is the final enthalpy reached in a process where the working fluid is brought to rest isentropically from a velocity v . This definition can be directly applied to temperature and pressure, so we can talk also about total or stagnation temperatures and pressures.

We now are in position to define the *efficiency* of the turbine. In general, there are two types of efficiencies used in turbine analysis. If we consider that any kinetic energy of the fluid leaving the turbine is a waste since otherwise it could be used to increase the work done by it, then we will use the definition of *static* efficiency

$$\eta_{st} = \frac{\Delta h'}{\Delta h_s} = \frac{h'_{in} - h'_{out}}{h'_{in} - h'_{s,out}} \quad (22)$$

where $h_{s,out}$ is the exit total enthalpy the fluid would have if expanded ideally to the exit static pressure.¹ We can see that in the idealized case where the working fluid leaves the turbine with zero velocity after an isentropic expansion, $h'_{out} = h_{s,out}$, therefore the static efficiency would be unity.

On the other hand, if the exit kinetic energy is useful as in multi-turbine machinery or at in-between locations of multistage turbines, then the penalization included in the static efficiency definition is not fair at all. In this case it is better to consider the total enthalpy $h'_{s,out}$ the fluid would have if expanded ideally to the actual exit total pressure; this leads to the *total* efficiency definition

$$\eta_{tt} = \frac{\Delta h'}{\Delta h'_s} = \frac{h'_{in} - h'_{out}}{h'_{in} - h'_{s,out}} \quad (23)$$

This last definition is more rigorous in every sense since all losses are accounted for, however it is more practical to use the static efficiency in rocket turbine analysis because in general there is the intention of extracting the highest shaft power from the turbine; in the idealized case this means converting all kinetic energy into useful work. Another reason is that the measurement of total quantities at the turbine exit is difficult because of flow non-uniformities which cause variations of the fluid dynamic total conditions. Estimating static parameters is relatively easy as the static pressure does not vary heavily with flow non-uniformity.

Consider an isentropic expansion to condition $h'_{s,out} = h_{s,out} + \frac{1}{2} C_o^2$. It can be shown that for this kind of process in the absence of heat transfer and work, the total enthalpy remains constant $h'_{in} = h'_{s,out}$, therefore the spouting velocity is

1. It is important not to get confused with the notation at this point. The prime has been taken out from $h_{s,out}$ just to indicate the expansion of the gases to the exit *static* pressure.

$$C_o = \sqrt{2gJ(h_{in} - h_{s,out})} = \sqrt{2gJ\Delta h_s}$$

where g and J are conversion factors with value unity in SI metric units and the following in english engineering units

$$g = 386 \frac{\text{lbf-in}}{\text{lbf-sec}^2} \quad J = 9336 \frac{\text{in-lbf}}{\text{Btu}}$$

And with the static efficiency definition (22), we have

$$C_o = \sqrt{\frac{2gJ\Delta h'}{\eta_{st}}} \quad (24)$$

So finally, the velocity ratio can be written as

$$v_r = \frac{u}{C_o} = \sqrt{\frac{\eta_{st}}{2gJ}} \bar{R} \frac{\Omega_{F2}}{\sqrt{\Delta h'}} \quad (25)$$

where $u = \bar{R}\Omega_{F2}$ is the tangential blade velocity with respect to the mean radius of the turbine rotor \bar{R} .

Values for the HPFTP turbine were extracted from ref. [2] and ref. [5] respectively

$$\eta_{st} = 0.842 \quad \bar{R} = 5.07 \text{ in}$$

which gives us

$$v_r = \frac{u}{C_o} = 0.00173 \frac{\Omega_{F2}}{\sqrt{\Delta h'}} \quad (26)$$

Rocketdyne in [3] uses a value of 0.001693 for this coefficient. The values are close enough as to suggest that both analyses are similar.

The HPFTP is a two-stage low reaction turbine, **Figure 4** shows a simplified schematic side view of it. We can distinguish three regions of interest: the turbine inlet (*in*), the interstage (*int*), and the turbine exit (*out*). From **Figure 1** we can see that the inlet

conditions are very close to those at the Fuel Preburner (FP) and at the exit we have practically Fuel Injector (FI) conditions.

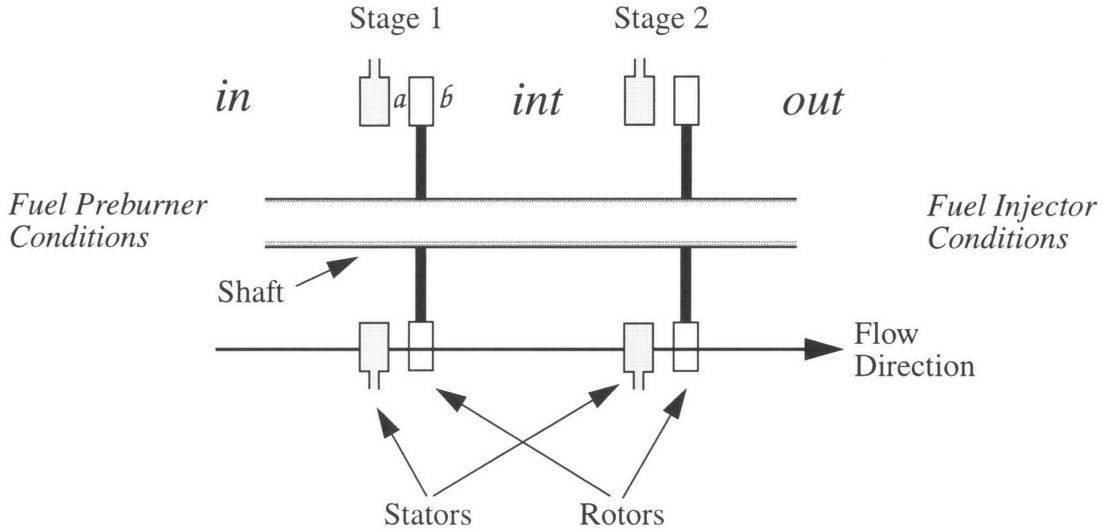


FIGURE 4. Cross Section Schematic of a Two-Stage Turbine

In this analysis we will assume that both stages have similar geometries and sustain the same pressure ratio. The power \mathcal{P} generated by a turbine is proportional to the drop of total enthalpy in the rotor

$$\mathcal{P} = \dot{m}_{ft2} \Delta h' \quad (27)$$

where \dot{m}_{ft2} is the mass flow rate through the turbine or stage. We can calculate the power generated by each stage:

$$\mathcal{P}_1 = \dot{m}_{ft2} (h'_{in} - h'_{int}) \quad \mathcal{P}_2 = \dot{m}_{ft2} (h'_{int} - h'_{out})$$

Since both stages deliver their power to the same shaft, the total power generated can be obtained by adding the individual contributions. By doing so, we see that the net power generated by the turbine depends only on the inlet and exit conditions

$$\mathcal{P} = \mathcal{P}_1 + \mathcal{P}_2 = \dot{m}_{ft2} (h'_{in} - h'_{out})$$

Now, from the specific heat per unit mass definition $dh = c_p dT$, and considering that we are dealing with a calorically perfect gas where \bar{c}_p can be taken as constant we have $h = \bar{c}_p T$. In practice this is not completely true, however as the work gases are generated at the fuel preburner with a fuel rich mixture far from stoichiometry, the combustion temperatures are not very high and remain almost unchanged while in the throttling phase. At these conditions the specific heat is relatively insensitive to temperature changes and can be taken as constant. With all this in mind, the power equation can be written as

$$\mathcal{P} = \dot{m}_{ft2} \bar{c}_p T'_{FP} \left(1 - \frac{T'_{FI}}{T'_{FP}} \right) \quad (28)$$

This equation is the same for metric and english units. In general for the latter we have

$$[\mathcal{P}] = \frac{\text{Btu}}{\text{sec}} \quad [\bar{c}_p] = \frac{\text{Btu}}{\text{lbm} \cdot ^\circ\text{R}} \quad [T] = ^\circ\text{R} \quad [\dot{m}] = \frac{\text{lbm}}{\text{sec}}$$

In order to continue with our analysis we need to define another quantity usually called the *infinitesimal-stage* or *polytropic efficiency*. Suppose that at the inlet of a turbine we have certain values of the total pressure and total temperature, P' and T' . After the working gas expands through the blades in the stator and rotor, it leaves with a relatively small decrement in total pressure and total temperature $P' - dP'$ and $T' - dT'$. Now let us introduce these conditions into the efficiency definition

$$\eta_p = \frac{h'_{in} - h'_{out}}{h'_{in} - h'_{s,out}} = \frac{T'_{in} - T'_{out}}{T'_{in} - T'_{s,out}} = \frac{T' - (T' - dT')}{T' - (T' - dT'_s)} = \frac{dT'}{dT'_s} \quad (29)$$

From the first law of thermodynamics and the enthalpy and entropy definitions, it can be shown that for an isentropic process the following relation applies to an ideal, calorically perfect gas

$$\frac{T'_{in}}{T'_{out}} = \left(\frac{P'_{in}}{P'_{out}} \right)^{\frac{\gamma-1}{\gamma}} \quad (30)$$

Where the quantity γ is the ratio of specific heat at constant pressure \bar{c}_p to the specific heat at constant volume \bar{c}_v . Written in terms of differential conditions we have

$$\frac{T'}{T' - dT_s} = \left(\frac{P'}{P' - dP'} \right)^{\frac{\gamma-1}{\gamma}}$$

combining this with definition (29) and arranging terms we see that

$$\frac{dT'}{T'} = \eta_p \left[1 - \left(1 - \frac{dP'}{P'} \right)^{\frac{\gamma-1}{\gamma}} \right] \quad (31)$$

As the quantity dP' is small compared to P' , we can expand the term inside parenthesis using the binomial expansion $(1+x)^n = 1 + nx + \dots$, taking only linear terms in x , (31) is approximated to

$$\frac{dT'}{T'} \approx \eta_p \left[1 - \left(1 - \left(\frac{\gamma-1}{\gamma} \right) \frac{dP'}{P'} \right) \right]$$

Rewriting it and integrating between inlet and exit conditions with the assumption that the η_p remains constant, we have

$$\int_{T'_{FP}}^{T'_{FI}} \frac{dT'}{T'} = \eta_p \left(\frac{\gamma-1}{\gamma} \right) \int_{P'_{FP}}^{P'_{FI}} \frac{dP'}{P'}$$

which leads to the result

$$\frac{T'_{FI}}{T'_{FP}} = \left(\frac{P'_{FI}}{P'_{FP}} \right)^{\eta_p \frac{\gamma-1}{\gamma}} \quad (32)$$

In this way we now can treat our real process described by (32) as a polytropic one of the form $p v^n = const.$, with

$$n = \frac{\gamma}{\eta_p + \gamma(1 - \eta_p)}$$

this is the reason for calling η_p the *polytropic efficiency*. The advantage of using this efficiency definition is that η_p does not change with operating conditions, remaining more or less constant for a multistaged turbine. In theory its application is justified when dealing with a very large number of infinitesimal stages. The HPFTP turbine has only two stages, however their pressure ratio is relatively small (about 1.192 per stage); the small pressure decrement results in a good approximation to an infinitesimal stage so the polytropic efficiency can be used.

Now, from the definition (23) of total efficiency and the isentropic relation (30) we note that for the first stage (see **Figure 4**)

$$T'_{FP} - T'_{int} = \eta_{tt} T'_{FP} \left[1 - \left(\frac{P'_{int}}{P'_{FP}} \right)^{\frac{\gamma-1}{\gamma}} \right] = \frac{\Delta h'_{stage}}{c_p} \quad (33)$$

but also from our infinitesimal-stage considerations

$$T'_{FP} - T'_{int} = T'_{FP} \left[1 - \left(\frac{P'_{int}}{P'_{FP}} \right)^{\eta_p \frac{\gamma-1}{\gamma}} \right]$$

Let us make the assumption that both stages hold the same pressure ratio, in other words

$$\frac{P'_{FI}}{P'_{int}} = \frac{P'_{int}}{P'_{FP}} \quad \text{or} \quad \frac{P'_{int}}{P'_{FP}} = \sqrt{\frac{P'_{FI}}{P'_{FP}}}$$

After combining these expressions we get a direct relationship between the total and the polytropic efficiencies

$$\eta_p = \frac{2 \ln \left(1 - \eta_{tt} \left[1 - \left(\frac{P'_{FI}}{P'_{FP}} \right)^{\frac{\gamma-1}{2\gamma}} \right] \right)}{\frac{\gamma-1}{\gamma} \ln \left(\frac{P'_{FI}}{P'_{FP}} \right)} \quad (34)$$

Finally, from the efficiency definitions (22) and (23) for the first stage (See **Figure 4**)

$$\eta_{st} = \frac{T'_{FP} - T'_{int}}{T'_{FP} - T'_{s,int}} \quad \text{and} \quad \eta_{tt} = \frac{T'_{FP} - T'_{int}}{T'_{FP} - T'_{s,int}}$$

where the isentropic relations can be used as

$$T_{s, int} = T'_{FP} \left(\frac{P_{int}}{P'_{FP}} \right)^{\frac{\gamma-1}{\gamma}} \quad \text{and} \quad T'_{s, int} = T'_{FP} \left(\frac{P'_{int}}{P'_{FP}} \right)^{\frac{\gamma-1}{\gamma}}$$

and also from the total or stagnation conditions definition, noting that between the stages the speed of sound is given by $a = \sqrt{\gamma R_g T_{s, int}}$; with the Mach number definition $M = v/a$, we can easily verify that

$$T'_{s, int} = T_{s, int} \left(1 + \frac{\gamma-1}{2} M^2 \right)$$

which can be used to find the total efficiency in terms of the static efficiency.

$$\eta_{tt} = T^* \left[1 - \left(1 + \frac{\gamma-1}{2} M^2 \right) \left(1 - \frac{T^*}{\eta_{st}} \right) \right]^{-1}$$

where (again, from definition (23) and the isentropic relations)

$$T^* = \frac{T'_{FP} - T'_{int}}{T'_{FP}} = \eta_{tt} \left[1 - \left(\frac{P'_{FI}}{P'_{FP}} \right)^{\frac{\gamma-1}{2\gamma}} \right]$$

As we can see T^* depends itself on the total efficiency which we are looking for, however an iterative calculation can be performed with $\eta_{tt} = 1$ for the first T^* estimation until convergence is obtained.

For the HPFTP turbine, we have a Mach number close to $M \sim 0.13$, and a pressure ratio of about 1.42. Taking the static efficiency as before, $\eta_{st} = 0.843$, and estimating the value for $\gamma = 1.375$ for a mixture ratio of 0.848, typical for the fuel preburner, with the specific heat taken at the correspondent temperature of $1780^\circ R$, then we find that the total efficiency takes a value of $\eta_{tt} = 0.896$, which corresponds to a polytropic efficiency of $\eta_p = 0.892$. This can be compared with the value of 0.884 used in [3].

With all these considerations in mind, the power equation (28) can be written as

$$\mathcal{P} = \dot{m}_{ft2} \bar{c}_p T'_{FP} \left[1 - \left(\frac{P'_{FI}}{P'_{FP}} \right)^{\eta_p} \frac{\gamma-1}{\gamma} \right]$$

The torque generated by the HPFTP turbine is therefore

$$\tau_{ft2} = J \frac{\mathcal{P}}{\Omega_{f2}} = \frac{J}{\Omega_{f2}} \dot{m}_{ft2} \bar{c}_p T'_{FP} \left[1 - \left(\frac{P'_{FI}}{P'_{FP}} \right)^{\eta_p} \frac{\gamma-1}{\gamma} \right] \quad (35)$$

To see how our torque estimation relates to that reported in [3], let us write the torque with respect to the power definition (27) as

$$\tau_{ft2} = J \frac{\dot{m}_{ft2} \Delta h'}{\Omega_{f2}} = J \frac{\dot{m}_{ft2} \sqrt{\Delta h'} \sqrt{\Delta h'}}{\Omega_{f2}}$$

From the spouting velocity definition (24), and because $u = \bar{R} \Omega_{F2}$, we can relate the torque generated to the velocity ratio v_r

$$\tau_{ft2} = J \bar{R} \sqrt{\frac{\eta_{st}}{2gJ}} \frac{\dot{m}_{ft2} \sqrt{\Delta h'}}{v_r} \quad (36)$$

Substituting the values that we have been using

$$\tau_{ft2} = 17.63 \sqrt{\eta_{st}} \frac{\dot{m}_{ft2} \sqrt{\Delta h'}}{v_r} \quad (37)$$

Now let us write this torque equation exactly in the same way as it is in [3]

$$\tau_{ft2} = 20.3 \dot{m}_{ft2} \sqrt{\Delta h'} \Gamma_{ft2}[v_r] \quad (38)$$

Comparing it with (37) and considering for a moment that the efficiency does not depend on the velocity ratio, then the function Γ_{ft2} , which we will call *Torque Coefficient*, can be expressed as

$$\Gamma_{ft2}[v_r] = 0.8685 \frac{\sqrt{\eta_{st}}}{v_r} \quad (39)$$

The solid curve in **Figure 5** shows this function compared to the dashed which is the one extracted from [3]

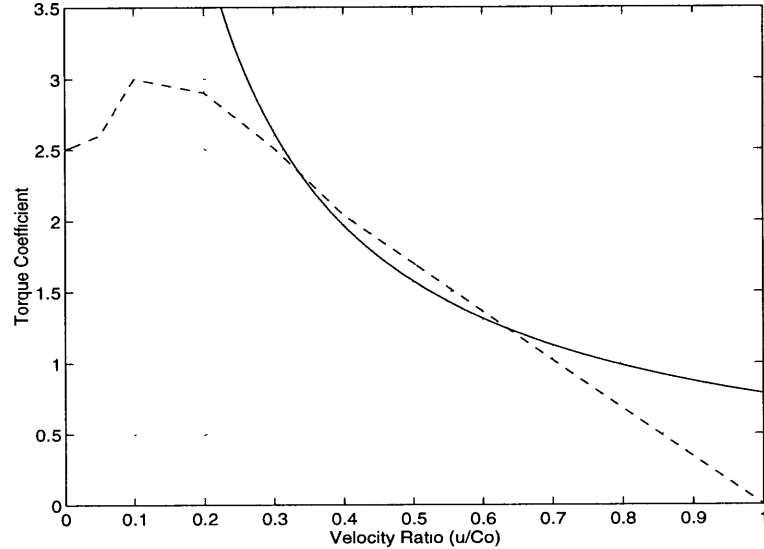


FIGURE 5. Torque Coefficient (constant efficiency) vs. Velocity Ratio

We see that for small and close to unity values of v_r , our estimated Torque Coefficient is somewhat different from the dashed line. However, the operating points of the HPFTP turbine lie in the middle of this range, from 0.3 to about 0.7. The difference can be attributed to the fact that we took the efficiency as constant, while in reality it varies with the rotor speed and, ultimately, with the velocity ratio. As an illustration, we can estimate in a very simple case the way in which the torque coefficient varies with v_r . From the definition of static efficiency η_{st} and from the *Euler Equation*¹

$$\Delta h' = \frac{1}{gJ} u \Delta V_u \quad (40)$$

1. The Euler equation determines in a purely geometrical way the form in which the fluid velocity transforms into useful work by the turbine. For a complete derivation of it refer for example to [6].

where u is the rotor tangential velocity and ΔV_u is the tangential component of the differential fluid velocity between the exit of the rotor and the inlet of the stator in a particular stage. **Figure 6** shows a velocity diagram where the V 's represent absolute velocities while the W 's are velocities relative to the rotor. The flow moves in the x direction before entering into the stator. In this diagram we have considered that the magnitude of the relative velocities of the fluid out of the stator (or into the rotor) and out of the rotor are the same. This kind of turbine is commonly termed as an *impulse* turbine.¹ The HPFTP turbine is not exactly of this kind (although it is close), however this assumption will simplify our analysis.

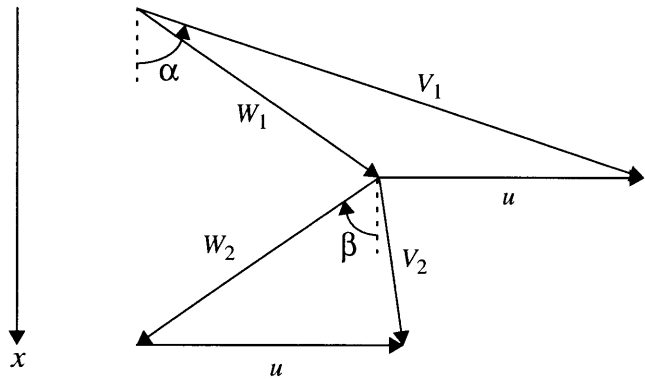


FIGURE 6. Velocity Diagram for an Impulse Turbine

Finally assume also that the only penalization taken into account in this particular analysis in terms of turbine efficiency is the exit kinetic energy which is not converted into useful work, in other words $\eta_{tt} = 1$, the expansion process is isentropic.

Each vector in **Figure 6** can be decomposed in their axial (x) and tangential (u) components. From our assumptions, $W_{2u} = -W_{1u}$ and $V_{1x} = V_{2x}$ so we have

$$V_{2u} = W_{2u} + u = -W_{1u} + u = -(V_{1u} - u) = -V_{1u} + 2u$$

1. In an impulse turbine, there is no change in static enthalpy in the rotor. The *degree of reaction* in a turbine is precisely defined as the ratio of change in static enthalpy in the rotor to that in the complete stage; an impulse turbine is therefore referred also as a zero reaction turbine.

and also $V_{1u} = V_1 \sin \alpha$, where α is the stator exit angle ($\alpha = 70^\circ$, $\beta = 60^\circ$ and the turbine reaction $R = 0.216$ in the HPFTP turbine, from ref. [5]). As $\eta_{tt} = 1$, the static enthalpy at the exit of the rotor (station 2) is the same as in the exit of the stator (station 1), therefore $V_1 = \sqrt{2gJ(h_o - h_1)} = \sqrt{2gJ\Delta h_s}$. And now taking the difference of tangential velocities, we get

$$\Delta V_u = V_{1u} - V_{2u} = 2V_{1u} - 2u = 2\sqrt{2gJ\Delta h_s} \sin \alpha - 2u$$

and from (40), using the definition (22)

$$\eta_{st} = \frac{\Delta h'}{\Delta h_s} = \frac{4u \sin \alpha}{\sqrt{2gJ\Delta h_s}} - \frac{4u^2}{2gJ\Delta h_s}$$

Now, recalling the spouting velocity definition (24), we can write this expression in terms of the velocity ratio v_r as

$$\eta_{st} = 4v_r \sin \alpha - 4v_r^2 \quad (41)$$

Substituting this into equation (39) yields

$$\Gamma_{ft2}[v_r] = 1.737 \frac{\sqrt{v_r \sin \alpha - v_r^2}}{v_r} \quad (42)$$

Figure 7 shows this function (solid) against the one extracted from [3] (dashed). We can see that there is a significant improvement in a broader range of velocity ratios.

A more rigorous calculation involving the exact geometry and consideration of the dependence of the velocity ratio on the static efficiency would be required to improve the results already shown.

In [3] the increment in total enthalpy is given by the following equation

$$\Delta h' = \bar{c}_p T'_{FP} \left[1 - B149 \left(\frac{P'_{FI}}{P'_{FP}} \right)^{\eta_p \frac{\gamma-1}{\gamma}} \right] \quad (43)$$

where the constant coefficient has a value $B_{149} = 1.0213$. This represents an extra decrease in $\Delta h'$ of about 2% given the pressure ratio close to unity. The origin for this correction factor is not clear in the analysis already done. The reason for this is that in our efficiency considerations we only took into account some effects of the “aerodynamic” part, and in reality other losses like friction in seals and bearings heat losses or full viscous effects should be taken into account. Since this correction is quite small and considerations of such losses go beyond the scope of this work we leave the analysis of losses at this level.

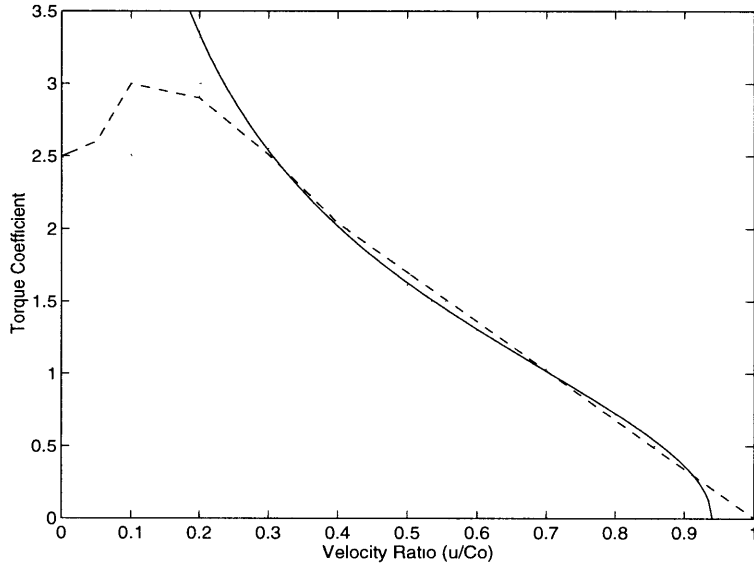


FIGURE 7. HPFTP Torque Coefficient (variable efficiency) vs. Velocity Ratio

3.2.1.2 Fuel Preburner Combustion Gas Characteristics

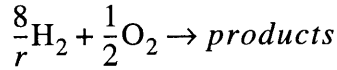
The specific heat \bar{c}_p depends not only on the gas composition given by the mixture ratio but also in the gas temperature. The variations of temperature in the fuel preburner are typically from 1600 to 1800°R for different operation points of the engine, this represents excursions of about 10% in temperature and 2% in \bar{c}_p . Given this weak dependence, a practical approximation is to consider only the variations of \bar{c}_p due to changes in the mixture ratio r .

$$\bar{c}_p = \text{fun}\left(\frac{\dot{m}_{ox}}{\dot{m}_f}\right) = \text{fun}(r)$$

In Rocketdyne's formulation, the specific heat is put in terms of the oxidizer flow rate to total flow rate ratio

$$\bar{c}_p = \text{fun}\left(\frac{\dot{m}_{ox}}{\dot{m}_f + \dot{m}_{ox}}\right) = \text{fun}\left(\frac{r}{r+1}\right) = \text{fun}(r^*)$$

From the chemical reaction given in the fuel preburner (for stoichiometry, $r = 8$)



we can obtain the mean specific heat \bar{c}_p depending on r^*

$$\bar{c}_p = \frac{r^* c_{pox} + 16(1 - r^*) c_{pf}}{r^* \mu_{ox} + 16(1 - r^*) \mu_f} \quad (44)$$

In the set of units used, the specific heat is given in Btu lbm⁻¹R⁻¹. **Figure 8a** shows equation (44) as the solid line for the full range of values of r^* , the dashed curve was extracted from [3]. The specific heats used in (44) were estimated at an adiabatic temperature of 1700°R in the fuel preburner, these values are

$$c_{pox} = 18.26 \frac{\text{Btu}}{\text{kmol}^\circ\text{R}} \quad c_{pf} = 16 \frac{\text{Btu}}{\text{kmol}^\circ\text{R}} \quad \mu_{ox} = 70 \frac{\text{lbm}}{\text{kmol}} \quad \mu_f = 4.41 \frac{\text{lbm}}{\text{kmol}}$$

where μ_{ox} and μ_f are the molecular masses of the oxygen and the hydrogen respectively.

As the \bar{c}_p of the gas mixture varies, the ratio of specific heats γ also changes its value.

From the gas constant (R_g) definition

$$R_g = \frac{\mathcal{R}}{\mu} = c_p - c_v$$

where $\mathcal{R} = 4.37 \text{ Btu kmol}^{-1}\text{R}^{-1}$ is the universal gas constant and μ the molecular mass, we can rewrite (44) as

$$\gamma = \left[1 + \frac{\mathcal{R}(15r^* - 16)}{r^* c_{pox} + 16(1 - r^*)c_{pf}} \right]^{-1} \quad (45)$$

Figure 8b shows equation (45) as the solid line compared with the dashed extracted from [3]. The differences between equations (44, 45) and those from [3] arise from the fact that in our work we have considered a *frozen* composition of the gases. The adiabatic temperature used in both cases was 1700°R , but as the composition approaches stoichiometry the temperature becomes very sensitive to changes in the mixture ratio, and therefore a more complete *equilibrium* calculation would be needed to eliminate the discrepancies between the two models. The “abnormal” behavior of the dashed line for values of $r^* < 0.1$ in **Figure 8b** is most likely due to an error in Rocketdyne’s model development. Nevertheless, in the regions where the mixture ratio is the one typically attained in the fuel preburner this simple approach is enough to compare with the one described in [3]. This is not true for values close to stoichiometry as in the MCC combustion chamber. NASA software is used in section 3.2.29 to perform an equilibrium calculation of gas properties in the MCC.

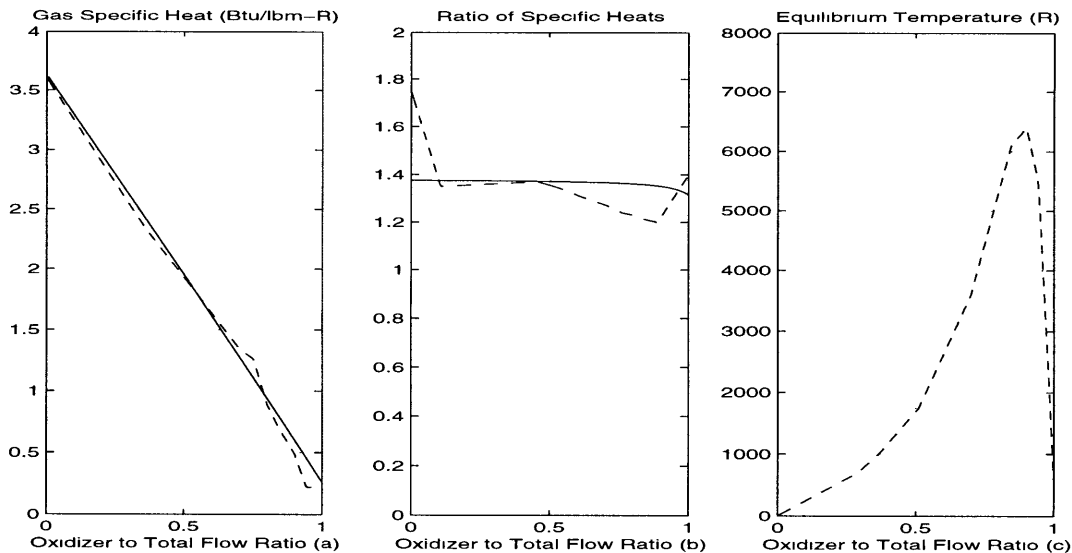


FIGURE 8. Different Gas Properties as Functions of Oxidizer Flow to Total Flow Ratio

Another by-product of the equilibrium calculation is, of course, the equilibrium temperature in terms of mixture ratio. In [3], this calculation was already performed and is shown here as the dashed line in **Figure 8c**.

3.2.1.3 HPFTP Turbine Mass Flow Rate Calculation

In the most general case, Euler's equation (40) can be applied to find the axial component of the absolute fluid velocity which can be considered as constant at any point of the mean radius of the turbine.¹ Using **Figure 6** as a reference (for notation purposes only, since this argument is applicable to reaction turbines as well), we observe that the tangential components of the fluid velocity that enters and leaves the rotor are, respectively,

$$V_{1u} = V_x \tan \alpha \quad \text{and} \quad V_{2u} = u - V_x \tan \beta$$

Minor manipulation of these expressions into Euler's equation yields (per stage)

$$V_x = \frac{gJ\Delta h'_{\text{stage}} + u^2}{u(\tan \alpha + \tan \beta)} \quad (46)$$

Considering that the total enthalpy drop in the first stage is the same as in the second stage and that in the stator inlet fuel preburner (*FP*) conditions prevail, then application of the continuity equation $\dot{m}_{ft2} = \rho_{FP} A V_x$ in terms of total quantities allow us to write

$$\dot{m}_{ft2} = \frac{AP'_{FP}}{JR_g T'_{FP}} \left(1 + \frac{\gamma-1}{2} M^2 \right)^{\frac{1}{1-\gamma}} \left(\frac{\frac{1}{2}gJ\Delta h' + \bar{R}^2 \Omega_{F2}^2}{\bar{R}\Omega_{F2}(\tan \alpha + \tan \beta)} \right) \quad (47)$$

where *A* and *M* are the effective area and the flow Mach number at the stator inlet. This is the most general form in which the turbine mass flow rate can be expressed; it, however, is not yet complete. There is a direct dependence of the turbine performance on the load driven by it. In our case this load is represented mostly by the 3-stage centrifugal pump. A

1. In practice, the turbine geometrical parameters can be selected to hold the variability of the fluid axial velocity within acceptable values as to consider it constant.

power balance between the turbine and pump equations can be performed and an involved procedure is needed to put (47) in the same form as it is described in [3]. Even after this procedure is completed, the results are not very good when calculations are performed far from the engine's steady state operation regimes (start-up sequence and throttle, for instance.) The reason for this is that many of the assumptions can be held no more at off-design conditions; the flow does not quite follow the blade exit angles, efficiency variations can be expected and many other non-modeled effects are likely to appear. For this reason, we will avoid introducing the power balance procedure. On the other hand we can assume a very simple case in which the turbine reaction is considered constant over all operating conditions.¹ Our final assumption is that the flow through the stator and through the rotor of the first stage is isentropic and the axial flow velocity is always constant. We will use **Figure 6** once more as our notation reference and will consider that the conditions at the stator inlet and rotor exit of the first stage are those at the fuel preburner and the interstage (*int*) respectively.²

Just before entering into the stator, the flow has only axial velocity (V_x). Conservation of total enthalpy in the stator yields (isentropic flow)

$$2(h_{FP} - h_1) = V_x^2 \tan^2 \alpha$$

Switching to the rotor coordinate frame, isentropic expansion results in

$$2(h_1 - h_{int}) = V_x^2 \tan^2 \beta - (V_x \tan \alpha - u)^2$$

And from the definition of turbine reaction, using these expressions, we see that

$$R = \frac{h_1 - h_{int}}{h_{FP} - h_{int}} = \frac{V_x^2 \tan^2 \beta - (V_x \tan \alpha - u)^2}{V_x^2 \tan^2 \beta + u(2V_x \tan \alpha - u)} \quad (48)$$

-
1. This statement is roughly equivalent to saying that the power delivered by the turbine is balanced with the power absorbed by the pump, with no allowance for inertia.
 2. See Figure 4 to complement this section. Points *a* and *b* (or *int*) are equivalent to points 1 and 2 of Figure 6 respectively.

Introducing the definition of *turbine flow coefficient* $\phi = \frac{V_x}{u}$, we can solve (48) to get

$$\phi = \frac{(1-R)\tan\alpha + \sqrt{(1-R)^2\tan^2\beta - R(1-R)\tan^2\alpha}}{\tan^2\alpha - (1-R)\tan^2\beta}$$

From mass conservation, the flow rate at the rotor exit is the same as the mass flow rate for both stages of the turbine, therefore we can apply the continuity equation at the turbine interstage (*int*) position: $\dot{m}_{ft2} = \rho_{int} V_{int} A_{int}$, where A_{int} is the annular flow area at the exit of the first stage rotor and $V_{int} = V_x$ is the turbine axial flow velocity. If h_b and \bar{R} are the blade height and mean radius of the turbine annulus, then

$$A_{int} = 2\pi h_b \bar{R} (1 - f_b) \quad (49)$$

where f_b represents a fraction of the area which is physically obstructed by the blade's wake which have certain thickness even if the blades are perfectly sharp at their trailing edge. Estimating the wake parameters is not a trivial task, most of the work related to it is centered on experimental results. With 63 blades in the rotor we can make a rough estimation of the blockage fraction based on the analysis presented in [9]: $f_b = 0.04$. Since $h_b = 0.854$ in, the effective annular flow area is $A_{int} = 26.1$ in². Introducing the flow coefficient definition into (46) we get

$$V_x = \frac{\phi}{\sqrt{\phi(\tan\alpha + \tan\beta) - 1}} \sqrt{gJ\Delta h'_{stage}} = K \sqrt{gJ\Delta h'_{stage}}$$

These considerations allow us to express the turbine mass flow rate as

$$\dot{m}_{ft2} = A_{int} \rho_{int} K \sqrt{gJ \bar{c}_p T'_{FP} \left(1 - \frac{T'_{int}}{T'_{FP}} \right)} \quad (50)$$

As $\eta_{tt} = 1$ in this estimation, we can make use of the isentropic relations between conditions at the fuel preburner and at *int*; considering again that both stages have the same pressure ratio

$$\frac{T'_{int}}{T'_{FP}} = \sqrt{\frac{P'_{FI}}{P'_{FP}}}^{\frac{\gamma-1}{\gamma}}$$

Now, using the ideal gas law equation $P = J\rho R_g T$, and assuming that the flow Mach number is low enough ($M \sim 0.13$) to approximate the static density to the stagnation density, we can write (50) as

$$\dot{m}_{ft2} = \frac{A_{int} K}{R_g} \frac{P'_{int}}{T'_{int}} \sqrt{\frac{g}{J}} \bar{c}_p T'_{FP} \left(1 - \sqrt{\frac{P'_{FI}}{P'_{FP}}}^{\frac{\gamma-1}{\gamma}} \right) \quad (51)$$

Using the above considerations, (51) depends only on the conditions at the fuel preburner (*FP*) and fuel injector (*FI*)

$$\dot{m}_{ft2} = A_{int} K \frac{\bar{\mu}}{\mathcal{R}} \frac{P'_{FP}}{\sqrt{T'_{FP}}} \sqrt{\frac{g}{J}} \bar{c}_p \left(\sqrt{\frac{P'_{FI}}{P'_{FP}}}^{\frac{2}{\gamma}} - \sqrt{\frac{P'_{FI}}{P'_{FP}}}^{\frac{\gamma+1}{\gamma}} \right) \quad (52)$$

where $\bar{\mu}$ is the average molecular weight of the mixture

$$\bar{\mu} = \frac{r\mu_{ox} + 16\mu_f}{r + 16}$$

The fuel preburner runs at steady state with a mixture ratio close to $r = 0.85$, this gives the following for the average specific heat and molecular weight

$$\bar{c}_p = 2.08 \frac{\text{Btu}}{\text{lbm} \cdot ^\circ\text{R}} \quad \bar{\mu} = 7.71 \frac{\text{lbm}}{\text{kmol}}$$

With these and other values already described, we can write (52) as

$$\dot{m}_{ft2} = 6.15 \frac{P'_{FP}}{\sqrt{T'_{FP}}} \sqrt{\left(\sqrt{\frac{P'_{FI}}{P'_{FP}}}^2 - \sqrt{\frac{P'_{FI}}{P'_{FP}}}^{\gamma+1} \right)} \quad (53)$$

In [3], the numerical coefficient is described as a function which varies with the shaft angular velocity

$$f[\Omega_{f2}] = 6.0528(1.258 - 1.637 \times 10^{-4}\Omega_{f2} + 2.552 \times 10^{-8}\Omega_{f2}^2)$$

this dependence is shown as the dashed line in **Figure 9**.

As we can see, as the velocity approaches operational values (>3500 rad/sec) our model (solid line in **Figure 9**) coincides relatively well with that of [3]. It is not unreasonable to believe, after comparing both results, that the analysis presented here was also performed in one way or another in [3]. The introduction of the extra function therefore is to respond to the “unknown” variations expected as the turbine accelerates through off-design operational regions. This is an excellent example of the need to introduce empirical correction factors to fine-tune a complex dynamic model.

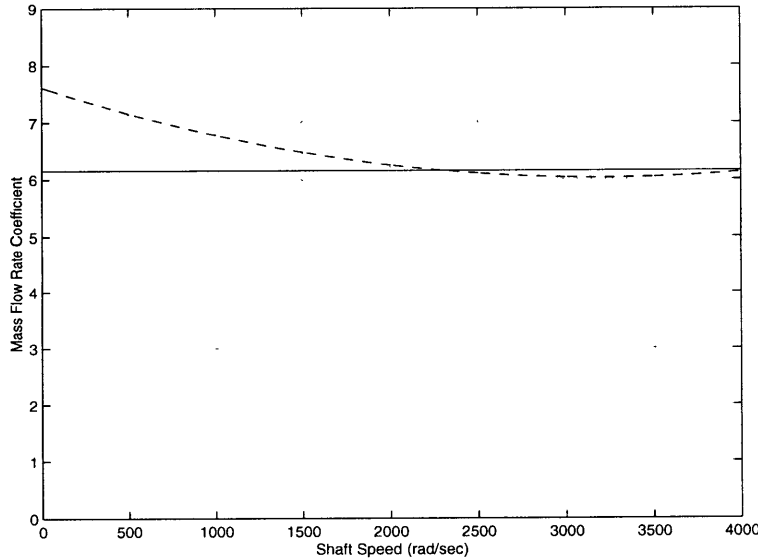


FIGURE 9. Variation of the Coefficient for the Mass Flow Rate equation (HPFTP)

3.2.1.4 HPFTP Additional Parameters

P'_{FI} and P'_{FP} are described in sections 3.2.28 and 3.2.24 respectively. As the preburners are run very fuel rich, T'_{FP} will depend heavily on the hydrogen temperature before injection and on the equilibrium temperature reached inside the preburner while reacting with the relatively small portion of LOX present. An energy balance can be performed to estimate the fuel preburner temperature

$$T'_{FP} = T'_{F2} + aT'_9$$

where T'_{F2} can be obtained from an equilibrium calculation (see **Figure 8c**). The constant a ($a = 0.99551$ in [3]) indicates that a small fraction of LOX contributes as well to the preburner temperature estimation. In reality a should be a function of LOX temperature and mixture ratio, however it appears that this function is nearly constant and was taken with a defined value for simplicity purposes. Fuel temperature T'_9 can be obtained by making a weighted average of the fuel flows converging to the preburners fuel supply line (position marked with a “9” in **Figure 1**). We see that these flows are two, one coming from the CCV valve (\dot{m}_{fnbp}) and the other from the exit of the nozzle heat exchanger (\dot{m}_4). Taking the average

$$T'_9 = \frac{T_4\dot{m}_4 + T_{fnbp}\dot{m}_{fnbp}}{\dot{m}_4 + \dot{m}_{fnbp}}$$

T_4 is obtainable from tables as a function of fuel internal specific energy (SU_4) and density (ρ_4) which are described in sections 3.2.33 and 3.2.31 respectively. For reasons that will become apparent in further sections, fuel properties in the fuel nozzle bypass (FNBP) are difficult to obtain analytically or from tables, therefore, empirical correction factors are introduced to describe their behavior in terms of “near-by” observable quantities. In the case of T_{fnbp} , a correction factor is introduced in terms of P_9 , the preburners fuel supply line pressure. This experimental relation is shown as the dashed curve in **Figure 10**.

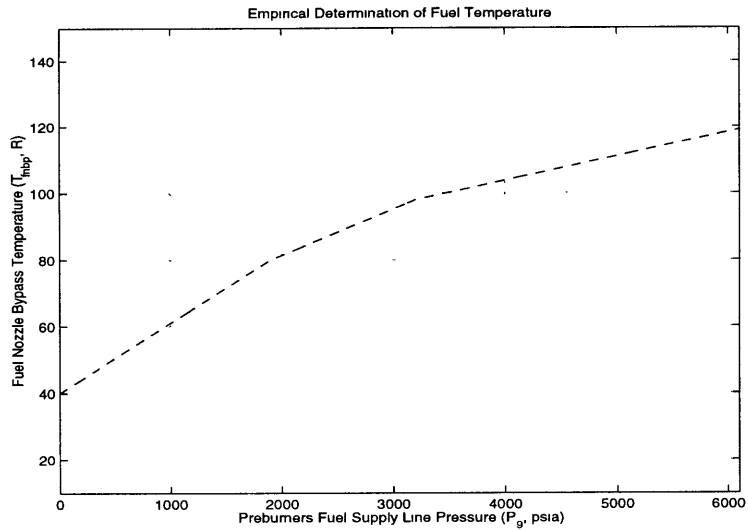


FIGURE 10. Empirical Representation of T_{fnbp} in Terms of P_g

3.2.1.5 HPFTP Centrifugal Pump Analysis

The other component of equation (20) that determines the speed of the shaft is the torque required or absorbed by the pump. The HPFTP pump is a 3-stage centrifugal type; staging is needed in order to attain the high pressure levels required by the engine using a low density liquid such as hydrogen and avoiding at the same time cavitation, i.e. the formation of bubbles. Figure 11 shows a simplified geometrical view of one of the stages of the pump. The blades force the fluid to exit the pump at a “back-leaning” angle β with respect to the radial direction with velocity V_p .

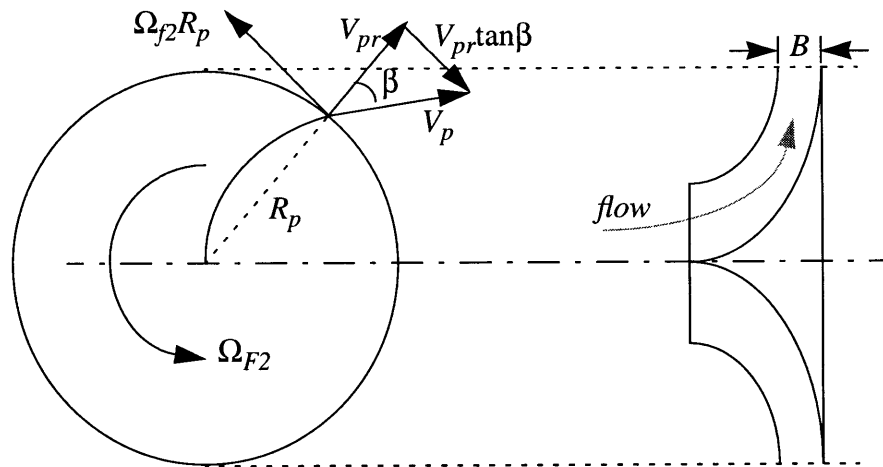


FIGURE 11. Single Stage of a Centrifugal Pump

In this kind of pump, each one of the components of the exit fluid velocity determines a specific parameter; the mass flow rate is determined by the radial component while the tangential component determines the torque required for such flow rate. From the pump geometry (with 24 blades, each with a thickness of 0.23in, the physical blockage factor is estimated to be around $f_b \sim 0.15$) we can approximate the volumetric flow rate Q as

$$Q = 2\pi R_p B V_{pr} (1 - f_b) \quad (54)$$

The required torque to obtain this Q is the rate of angular momentum of the fluid in the pump outlet. Assuming that the fluid has no angular momentum at the inlet then all of it will be transmitted by the rotating wheel and blades. From **Figure 11** we can see that the fluid leaves the pump with a net tangential speed V_{tg} given by (positive in shaft direction)

$$V_{tg} = \Omega_{f2} R_p - V_{pr} \tan \beta \quad (55)$$

Therefore, the required torque is (at constant radius and tangential velocity)

$$\tau = \frac{d}{dt} R_p m V_{tg} = R_p \dot{m}_{fd2} V_{tg} \quad (56)$$

where \dot{m}_{fd2} is the fuel mass flow. Substituting (55) in (56) and adding the effect of the three stages for the HPFTP pump¹ we have for the absorbed torque

$$\tau_{fp2} = 3R_p \dot{m}_{fd2} (\Omega_{f2} R_p - V_{pr} \tan \beta) \quad (57)$$

Using (54) and as $\dot{m}_{fd2} = \rho_f Q$, where ρ_f is the fuel density, (57) turns into

$$\tau_{fp2} = 3R_p^2 \left(\frac{\dot{m}_{fd2}}{\Omega_{f2}} \right) \Omega_{f2}^2 \left(1 - \left(\frac{\dot{m}_{fd2}}{\Omega_{f2}} \right) \frac{\tan \beta}{2\pi(1-f_b)R_p^2 B \rho_f} \right) \quad (58)$$

1. This direct adding is possible as we are considering that the three pump stages are identical. This is not completely true, however the differences are small enough to lump the net effect into an identical set.

This equation can be simplified further by defining the *Flow Coefficient* ϕ_{f2} commonly used in this kind of analysis¹

$$\phi_{f2} = \frac{1}{\rho_f} \frac{\dot{m}_{fd2}}{\Omega_{f2}} \quad (59)$$

Introducing this coefficient, (58) is now

$$\tau_{fp2} = \frac{3R_p^2 \rho_f \phi_{f2} \Omega_{f2}^2}{g} \left(1 - \phi_{f2} \frac{\tan \beta}{2\pi(1-f_b)R_p^2 B} \right) \quad (60)$$

where the conversion constant g has been introduced to form a consistent set of units.

To see how close does this derivation approaches the one of [3] we searched from appropriate sources such as Rocketdyne's engineering drawings and part specifications:

$$R_p = 5.87 \text{ in} \quad B = 0.54 \text{ in} \quad \beta = 43.6^\circ$$

Since the liquid fuel (hydrogen) experiences somewhat sensible variations of density with pressure, and pressure changes drastically at each stage of the pump, it is reasonable to take an average density value, from tables [15], we take it as $\rho_f = 2.9 \times 10^{-3} \text{ lbm-in}^{-3}$.

In this way, the flow coefficient (59) is

$$\phi_{f2} = 344 \frac{\dot{m}_{fd2}}{\Omega_{f2}}$$

A value of 339 is used in [3], quite similar. This suggests that the average assumption was considered too.

After substituting values, the torque equation (60) becomes

1. Flow coefficients are usually defined as non-dimensional quantities. For consistency reasons, however, we have introduced a dimensional ϕ in the same way as it is described in [3].

$$\tau_{fp2} = 7.77 \times 10^{-4} \phi_{f2} \Omega_{f2}^2 (1 - 0.0096 \phi_{f2}) \quad (61)$$

For comparison purposes, let's put this equation in the same form as in [3]

$$\tau_{fp2} = 2.9783 \times 10^{-3} \Omega_{f2}^2 \Gamma_{fp2}[\phi_{f2}] \quad (62)$$

If this is true then the function Γ_{fp2} , called *Torque Coefficient* in [3], should be given by

$$\Gamma_{fp2}[\phi_{f2}] = 0.2608(\phi_{f2} - 0.0096\phi_{f2}^2) \quad (63)$$

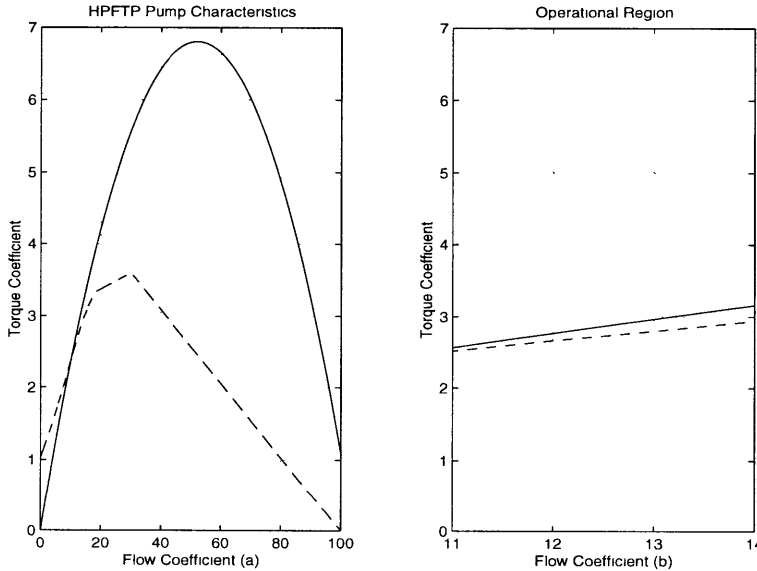


FIGURE 12. Torque Coefficient vs. Flow Coefficient for the HPFTP

The solid curve in **Figure 12a** represents equation (63) as compared with the dashed extracted from [3]. In steady state operation the values of ϕ_{f2} range from 11 to 14; it is only larger than that for a fraction of a second after the ignition signal, when high-order effects are dominant. **Figure 12b** shows both curves plotted in the operating region, we can expect that both models will have a similar behavior in that particular region. This fact will preclude our model from being used in an “off-design-point” analysis. Trying to make an analytical description of turbomachinery components is a very difficult matter even in well

understood devices, for example those used in aircraft engines. It is a common practice to obtain sets of curves similar to the one depicted in **Figure 12** from empirical data. The approach used in this thesis is very useful for marking trends only; this becomes evident when comparing both curves in **Figure 12** for values outside the operational region.¹

Finally (refer to **Figure 1**) the pumped fuel is separated in three main flows and a secondary which we will denote as \dot{m}_{asi} , two of the principal streams are used to regeneratively cool the nozzle \dot{m}_{fn} and the main combustion chamber \dot{m}_{mc} , while the third one \dot{m}_{fnbp} is diverted into the fuel and oxidizer preburners. The secondary flow is separated into three flows which feed the Augmented Spark Igniters (ASI) in the FP, OP and MCC. In this way we have that

$$\begin{aligned}\dot{m}_{fd2} &= \dot{m}_{fn} + \dot{m}_{mc} + \dot{m}_{fnbp} + \dot{m}_{asi} && \text{where} \\ \dot{m}_{asi} &= \dot{m}_{asifp} + \dot{m}_{asiop} + \dot{m}_{asimc}\end{aligned}\quad (64)$$

It would be wrong to affirm that the analysis presented for the HPFTP is as deep as can it be, there is much more complexity involved in each of its components which are significantly more than the number introduced here. Several of these components modify in one way or another the dynamics of the engine, e.g. bearings, seals, pipes, etc, and therefore should be taken into account. Variations can also be expected when introducing other factors in the analysis, such as losses from friction effects and from mechanical configurations.

3.2.2 High Pressure Oxidizer Turbopump Speed (Ω_{o2})

Much that has been said about the HPFTP in section 3.2.1 can be applied to the thermodynamic modeling of the HPOTP. It is also a two-stage turbine driven turbopump, however the torque generated is absorbed by two pump subsystems. In the first one, all of the oxidizer is pressurized by a two-staged centrifugal pump in parallel operation. Most of

1. Operational region is defined as the values that the engine variables can take when throttling from 65% to 109% RPL. Ignition sequence and shutdown are not included.

the oxidizer is then injected directly into the MCC through the MOV. Some of it however is diverted back to the second pump subsystem which is a single-stage centrifugal pump (Boost Stage) which further increases the pressure to that needed by the fuel and oxidizer preburners (see **Figure 1**). The rotational speed can be determined using a type 1 equation:

$$I_{o2} \frac{d\Omega_{o2}}{dt} = \tau_{ot2} - \tau_{op2} - \tau_{op3} \quad (65)$$

where

I_{o2} is the moment of inertia of the HPOTP rotor (lbf-in-sec²)

Ω_{o2} is the angular velocity of the HPOTP shaft (rad/sec)

τ_{ot2} is the torque generated by the 2-stage HPOTP axial-flow turbine (lbf-in)

τ_{op2} is the required torque of the 2-stage HPOTP centrifugal-flow pump (lbf-in)

τ_{op3} is the required torque of the HPOTP Boost Stage centrifugal-flow pump (lbf-in)

The value of the rotor inertia I_{o2} was directly extracted from [4]

$$I_{o2} = \frac{1}{0.882} \text{ lbf-in-sec}^2$$

3.2.2.1 HPOTP Turbine Section

The value used in [3] is 0.916 in the denominator. Making the same set of assumptions as in section 3.2.1, we can apply equation (25) also to the HPOTP as

$$v_r = \frac{u}{C_o} = \sqrt{\frac{\eta_{st}}{2gJ}} \bar{R} \frac{\Omega_{o2}}{\sqrt{\Delta h}} \quad (66)$$

Values for the HPOTP turbine were extracted from ref. [3] and technical drawings

$$\eta_{st} = 0.9 \quad \bar{R} = 5.06 \text{ in}$$

using these values (66) turns into

$$v_r = 0.001788 \frac{\Omega_{o2}}{\sqrt{\Delta h'}} \quad (67)$$

the coefficient reported in [3] has the value of 0.001630.

The results of section 3.2.1.1 can also be used to find the total and the polytropic efficiencies. Given the inlet and exit conditions of the turbine, the ratio of specific heats can be estimated to be 1.37, substituting values with a pressure ratio of 1.547 and a Mach number of M~0.13 yields $\eta_{tt} = 0.9462$ and therefore $\eta_p = 0.9446$, which can be compared to 0.95179 reported in [3].

For the torque we can use the HPOTP version of equation (36)

$$\tau_{ot2} = \bar{R} \sqrt{\frac{J\eta_{st}}{2g}} \frac{\dot{m}_{ot2}\sqrt{\Delta h'}}{v_r} = 17.59 \sqrt{\eta_{st}} \frac{\dot{m}_{ot2}\sqrt{\Delta h'}}{v_r} \quad (68)$$

In [3], the torque equation is expressed in the following form

$$\tau_{ot2} = 21.15 \dot{m}_{ot2} \sqrt{\Delta h'} \Gamma_{ot2}[v_r] \quad (69)$$

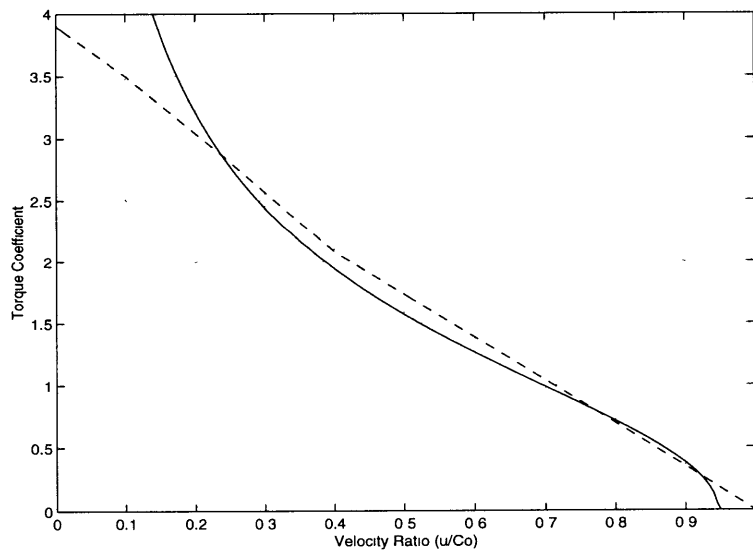


FIGURE 13. HPOTP Torque Coefficient vs. Velocity Ratio

Comparing equations (68) and (69) we see that

$$\Gamma_{ot2}[v_r] = 0.8317 \frac{\sqrt{\eta_{st}}}{v_r} \quad (70)$$

But as we already considered, a better approximation of this function can be obtained by allowing efficiency variations with the velocity ratio (41), therefore

$$\Gamma_{ot2}[v_r] = 1.6634 \frac{\sqrt{v_r \sin \alpha - v_r^2}}{v_r} \quad (71)$$

with $\alpha = 71.1^\circ$, taken from Rocketdyne's technical drawings. **Figure 13** shows this function against the one (dashed line) extracted from [3].

The increment in stagnation enthalpy across the turbine can be written as

$$\Delta h' = \bar{c}_p T'_{OP} \left[1 - C \left(\frac{P'_{FI}}{P'_{OP}} \right)^{\eta_p} \frac{\gamma-1}{\gamma} \right] \quad (72)$$

where C is a constant with value 1 for our model, or a function of shaft speed as described in [3]

$$C[\Omega_{o2}] = 1.007 + 6.276 \times 10^{-6} \Omega_{o2}$$

At maximum RPL, with a shaft speed of about 3060 rad/sec, this coefficient has a value of 1.0268, this term represents a decrement in total enthalpy of about 2.5%. There are several mechanisms involving seals and bearings that ultimately can cause this enthalpy drop. The HPOTP turbine analysis has been oversimplified since we have considered all along that both stages are identical, but in reality they have different geometry and aerodynamic characteristics. We have tried to lump these differences into an “averaged” identical-stage version, which is likely to introduce errors. The gas specific heat and ratio of specific heats can be calculated also with equations (44) and (45) respectively.¹

1. Recall that these frozen composition calculations are possible only because the preburners run fuel rich at design conditions.

3.2.2.2 HPOTP Turbine Mass Flow Rate

The HPOTP version of equation (52) allow us to estimate the mass flow rate through the turbine in steady state configuration. Considering a blockage fraction of 0.05, a blade height of 0.43 in, a rotor exit angle $\beta = 60^\circ$ and a mixture ratio of $r = 0.67$ in the oxidizer preburner, we can estimate the following

$$\dot{m}_{ot2} = 2.76 \frac{P'_{OP}}{\sqrt{T'_{OP}}} \sqrt{\left(\sqrt{\frac{P'_{FI}}{P'_{OP}}}^{\frac{2}{\gamma}} - \sqrt{\frac{P'_{FI}}{P'_{OP}}}^{\frac{\gamma+1}{\gamma}} \right)} \quad (73)$$

Again in [3] the numerical coefficient of equation (73) appears as a function of Ω_{o2}

$$f[\Omega_{o2}] = 2.142(1.247 - 1.129 \times 10^{-4} \Omega_{o2} + 9.245 \times 10^{-9} \Omega_{o2}^2)$$

The dashed curve in **Figure 14** shows this function against the (solid) constant value given in equation (73). Again, the variable coefficient is very likely to be introduced to compensate for the dynamic behavior in this steady state expression. As we can see in **Figure 14**, our derivation departed considerably from that of [3] in the steady state operational region (> 2000 rad/sec); this was expected since we have oversimplified our description of the two-stage turbine. In reality each stage is very different, they have different blade number, geometry and size. This means different operation conditions, different pressure ratio and dynamic properties.

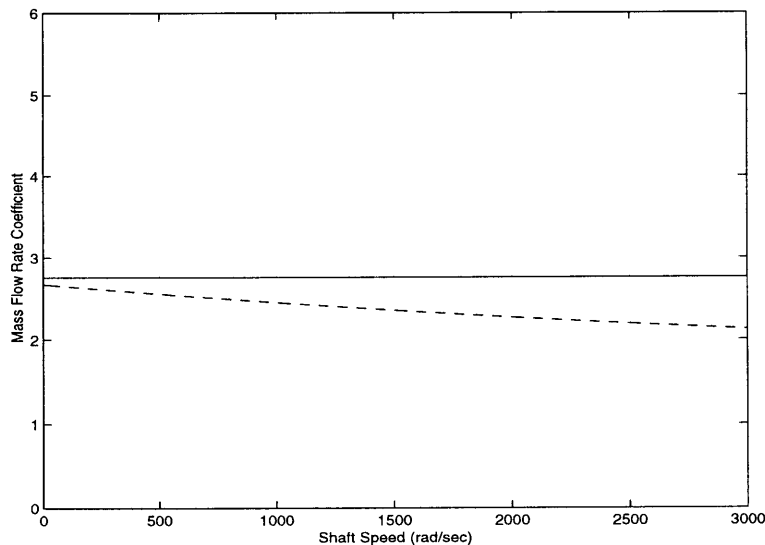


FIGURE 14. Variation of the Coefficient for the Mass Flow Rate Equation (HPOTP)

3.2.2.3 HPOTP Additional Parameters

P'_{OP} is defined section 3.2.23 and the oxidizer preburner temperature T'_{OP} can be obtained in the same way as it was done for T'_{FP} in section 3.2.1

$$T'_{OP} = T'_{O2} + aT'_9$$

where T'_9 is defined as before and T'_{O2} can be found with a thermodynamic equilibrium calculation (see **Figure 8c**). In [3] $a = 0.9651$ to compensate for the presence of LOX in the mixture.

With reference to **Figure 1**, we observe that the pumped oxidizer flow \dot{m}_{op2} is separated into four different paths; the first one \dot{m}_{mov} takes most of it through the MOV, the second diverts a fraction \dot{m}_{op3} directly to the boost stage, while a third fraction \dot{m}_{ot1} is sent back to the LPOTP to serve as the powering mechanism in the hydraulic turbine. A fourth fraction, very small compared to the others, is used as coolant fluid in the HPOTP's tubular heat exchanger. This flow has been excluded in the engine modeling reported in [3]; the reason can be attributed to its relatively small impact on the dynamics. As our reference point is given by [3], we will exclude it as well. These considerations allow us to write the oxidizer flow through the HPOTP as

$$\dot{m}_{op2} = \dot{m}_{mov} + \dot{m}_{op3} + \dot{m}_{ot1} \quad (74)$$

3.2.2.4 HPOTP Pump Section

From the flow coefficient definition (59)

$$\phi_{ox2} = \frac{1}{\rho_{ox}} \frac{\dot{m}_{op2}}{\Omega_{o2}} \quad (75)$$

In the same way as it was done for the HPFTP, the net torque required by the oxidizer pump can be written as

$$\tau_{op2} = \frac{R_p^2 \rho_{ox} \phi_{ox2} \Omega_{o2}^2}{g} \left(1 - \phi_{ox2} \frac{\tan \beta}{4\pi(1-f_b)R_p^2 B} \right) \quad (76)$$

where the effect of the two parallel stages with half mass flow each has been included. Accurate information about the internal geometry (blade angles, number and blocking) was not available, however nominal values involving other kinds of liquid oxygen turbopumps were extracted from [7] and averaged to be used here:

$$f_b \sim 0.2 \quad \beta = 72.5^\circ$$

From engineering drawings and thermodynamic tables

$$R_p = 3.46\text{in} \quad B = 0.5\text{in} \quad \rho_{ox} = 0.043\text{lbm-in}^{-3}$$

Using all these values allow us to write (76) as

$$\tau_{op2} = 1.3 \times 10^{-3} \phi_{ox2} \Omega_{o2}^2 (1 - 0.0527 \phi_{ox2}) \quad (77)$$

when comparing this to the expression given in [3]

$$\tau_{op2} = 0.04096 \Omega_{o2}^2 \Gamma_{op2} [\phi_{ox2}] \quad (78)$$

we see that the torque coefficient should be the following

$$\Gamma_{op2} [\phi_{ox2}] = 0.0326 (\phi_{ox2} - 0.0527 \phi_{ox2}^2) \quad (79)$$

The solid line in **Figure 15a** represents (79), which can be compared with the dashed functional relation extracted from [3]. The operational region of the HPOTP is shown in **Figure 15b**, we see that both curves are similar only for “design” points; same comments given with regard to the HPFTP can be applied here.

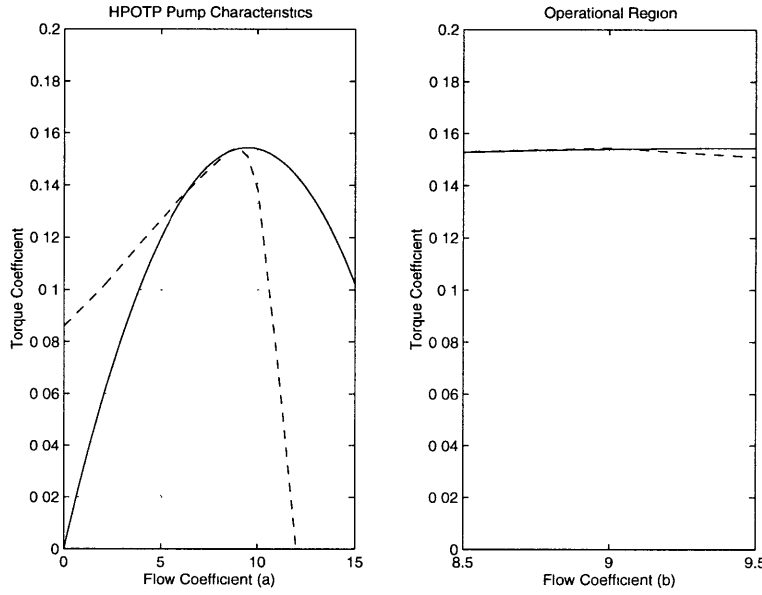


FIGURE 15. Torque Coefficient vs. Flow Coefficient for the HPOTP

3.2.2.5 HPOTP Boost Pump Section

For the boost stage, the flow coefficient is

$$\phi_{ox3} = \frac{1}{\rho_{ox}} \frac{\dot{m}_{op3}}{\Omega_{o2}} \quad (80)$$

which can be used to find the torque required by the single-staged boost pump

$$\tau_{op3} = \frac{R_p^2 \rho_{ox} \phi_{ox3} \Omega_{o2}^2}{g} \left(1 - \phi_{ox3} \frac{\tan \beta}{2\pi(1-f_b)R_p^2 B} \right) \quad (81)$$

As for the main pump, data on blockage and blade angle was not available, therefore they were selected with the criteria established in [7]

$$f_b \sim 0.2 \quad \beta = 72.5^\circ$$

while the following values were extracted from Rocketdyne's technical drawings

$$R_p = 2.57 \text{ in} \quad B = 0.25 \text{ in}$$

These numerical quantities transform (81) into

$$\tau_{op3} = 7.34 \times 10^{-4} \phi_{ox3} \Omega_{o2}^2 (1 - 0.3794 \phi_{ox3}) \quad (82)$$

after comparing this to the torque expression given in [3]

$$\tau_{op3} = 0.04196 \Omega_{o2}^2 \Gamma_{op3} [\phi_{ox3}] \quad (83)$$

we have that the torque coefficient should be

$$\Gamma_{op3} [\phi_{ox3}] = 0.0175 (\phi_{ox3} - 0.3794 \phi_{ox3}^2) \quad (84)$$

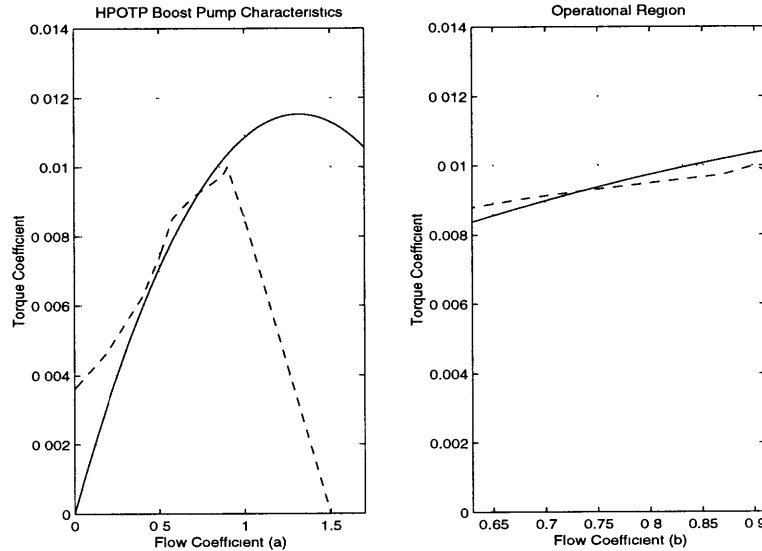


FIGURE 16. Torque Coefficient vs. Flow Coefficient for the HPOTP Boost Stage

The solid line in **Figure 16a** represents (84) as compared with the dashed which represents the boost pump characteristics as reported in [3]. **Figure 16b** shows both curves in the engine's operational region.

3.2.3 Low Pressure Fuel Turbopump Speed (Ω_{f1})

Most liquid rocket engines have the strict requirement of a minimum amount of pressure that the propellants should have before being pumped by the turbomachinery. This initial

“head” precludes cavitation from happening at the pump inlet. Cavitation can be very harmful to turbopump components; particularly in rocket engines it can lead to fluid-mechanical fluctuations and/or combustion instabilities which can have serious consequences. In most cases pressurizing the propellants while stored in the vehicle’s tanks is enough to avoid an excessively low pressure at the pump inlet. Of course, increasing the pressure inside the tanks has a direct impact on their structural characteristics which can be ultimately related to an increase in tank weight, without mentioning the added complexity of a pressurization subsystem. In the specific case of the high pressure turbopumps of the SSME, a somewhat large initial head is required. Tank pressurization was discarded because the increase in tank weight would decrease the payload capacity of the Space Shuttle in a very sensitive way. The best solution was found to be the adding of a pair of low pressure turbopumps; their introduction allowed the initial head to be exclusively gravitational, thus minimizing weight and structural concerns (and cost) of the only non-reusable component of the shuttle system. No numerical information was found regarding this component, therefore all values were extracted directly from [3].

The angular speed of the LPFTP can be found with a type 1 equation:

$$I_{f1} \frac{d\Omega_{f1}}{dt} = \tau_{ft1} - \tau_{fp1} \quad (85)$$

where

I_{f1} is the moment of inertia of the LPFTP rotor (lbf-in-sec²)

Ω_{f1} is the angular velocity of the LPFTP shaft (rad/sec)

τ_{ft1} is the torque generated by the 2-staged LPFTP axial-flow turbine (lbf-in)

τ_{fp1} is the required torque of the LPFTP inducer-type, axial-flow pump (lbf-in)

The rotor inertia is $I_{f1} = \frac{1}{1.0449}$ lbf-in-sec²

3.2.3.1 LPFTP Turbine Section

The LPFTP makes use of an axial-flow two-stage turbine. The analysis presented in 3.2.1 and 3.2.2 can be applied here once more. The velocity ratio

$$v_r = \frac{u}{C_o} = \sqrt{\frac{\eta_{st}}{2gJ}} \bar{R} \frac{\Omega_{f1}}{\sqrt{\Delta h}} \quad (86)$$

The coefficient has a value of

$$\sqrt{\frac{\eta_{st}}{2gJ}} \bar{R} = 0.001328$$

The torque produced by the turbine can be written as¹

$$\tau_{ft1} = J \frac{P}{\Omega_{f1}} = \frac{J}{\Omega_{f1}} \dot{m}_{ft1} c_p T_5 \left[1 - \left(\frac{P_{FI}}{P_{ft1}} \right)^{\eta_p \frac{\gamma-1}{\gamma}} \right] \quad (87)$$

Introducing the increase in enthalpy

$$\Delta h = c_p T_5 \left[1 - \left(\frac{P_{FI}}{P_{ft1}} \right)^{\eta_p \frac{\gamma-1}{\gamma}} \right] \quad (88)$$

where T_5 is the hydrogen temperature (now gasified, to drive the LPFTP turbine) at the exit of the MCC heat exchanger and P_{ft1} is the turbine inlet pressure. From **Figure 1** we can see that P_{ft1} comes from the pressure at the exit of the MCC cooling circuit P_5 . These pressures, however, are not identical; there is a net decrease due to friction as the fluid travels along the pipe that runs from the exit of the MCC heat exchanger to the inlet of the LPFTP turbine. This pressure loss can be put in terms of (2)

$$P_{FT1} = P_5 - \lambda \left(\frac{1}{2} \rho v^2 \right) \quad \text{with} \quad \lambda = f \frac{L}{D} \quad (89)$$

1. The primes denoting total conditions will be omitted from now on to simplify the notation.

where f , L and D are a friction coefficient dependent on the Reynolds number, the pipe length and diameter respectively. From the mass continuity equation $\dot{m} = \rho v A$, where A is the cross sectional area of the pipe, we can write (89) as

$$P_{ft1} = P_5 - C_5 \frac{\dot{m}_{ft1}^2}{\rho_5} \quad \text{where} \quad C_5 = \frac{8\lambda}{g\pi^2 D^4} \quad (90)$$

this coefficient has a value of $C_5 = 0.0002804$; ρ_5 is the hydrogen density at position 5 in **Figure 1** (see section 3.2.32). Using (86), the generated torque (87) can be written as

$$\tau_{ft1} = \bar{R} \sqrt{\frac{J\eta_{st}}{2g}} \frac{\dot{m}_{ft1} \sqrt{\Delta h}}{v_r} \quad (91)$$

allowing static efficiency variations with the velocity ratio (41), equation (91) becomes

$$\tau_{ft1} = \sqrt{\frac{J}{2g}} \bar{R} \sqrt{4v_r \sin \alpha - 4v_r^2} \dot{m}_{ft1} \frac{\sqrt{\Delta h}}{v_r} \quad (92)$$

where α is the stator exit angle. In [3], the coefficients were evaluated to yield

$$\tau_{ft1} = 13.34 \dot{m}_{ft1} \sqrt{\Delta h} \Gamma_{ft1}[v_r] \quad (93)$$

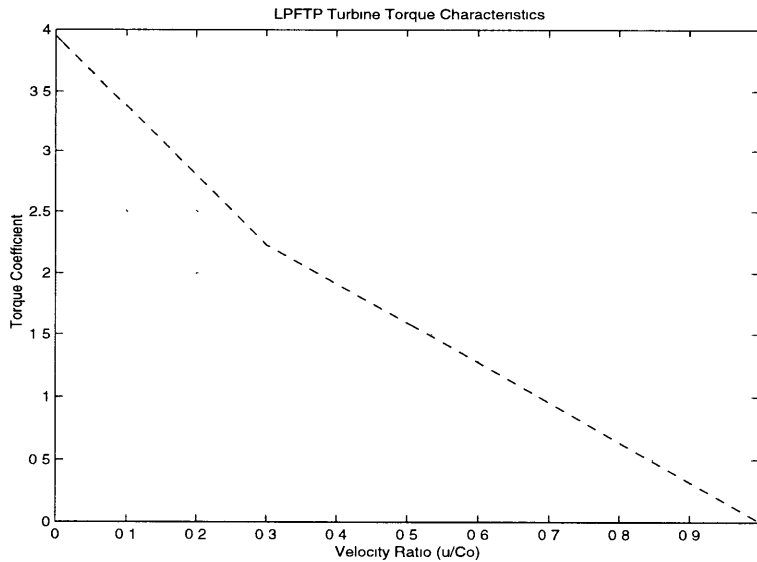


FIGURE 17. LPFTP Turbine Torque Characteristics

The torque coefficient $\Gamma_{ft1}[v_r]$ is shown as the dashed line in **Figure 17**.

3.2.3.2 LPFTP Turbine Mass Flow Rate

After driving the LPFTP turbine, the hydrogen flow is used as coolant for the hot gas manifold (HGM) which carries the hot gases created in the preburners into the fuel injector (FI); after that, it enters the FI along with the hot gases. However, before entering the FI a small fraction is tapped and diverted back into the LH tank to pressurize it. If we assume that the hydrogen density ρ_5 remains more or less constant (at a given RPL) while inside the pipe that runs from the exit of the MCC cooling circuit to the inlet of the FI then the turbine mass flow rate \dot{m}_{ft1} can be calculated from the continuity equation

$\dot{m}_{ft1} = \rho_5 v A_e$, where A_e is the flow area of the HGM coolant cavity exit. The gas velocity v can be put in terms of the enthalpy drop along the pipe

$$v = \sqrt{2gJ\Delta h_{pipe}}$$

We can extend our total efficiency definition (23) into a quantity η_{tp} that includes turbine efficiency and other losses along the pipe. By doing this, the gas velocity will depend on the ideal enthalpy drop

$$v = \sqrt{2gJ\eta_{tp}\Delta h_{id}} \quad \text{with} \quad \Delta h_{id} = c_p(T_5 - T_{FI})$$

Substituting the ideal gas law $P = J\rho R_g T$ yields

$$\dot{m}_{ft1} = \sqrt{\frac{2g\gamma\eta_{tp}A_e^2}{\gamma-1}\rho_5(P_5 - P_{FI})} \quad \text{where} \quad \frac{2g\gamma\eta_{tp}A_e^2}{\gamma-1} = 627.65 \quad (94)$$

P_5 and T_5 can be found from tables as functions of SU_5 (hydrogen specific internal energy at position 5 in **Figure 1**, see section 3.2.32) and ρ_5 which is described in section 3.2.30. The gas specific heat c_p can also be obtained from tables as function of the gas pressure and temperature (P_{ft1} and T_5).

3.2.3.3 LPFTP Pump Section

The pump configuration of the LPFTP is not of the centrifugal type described in sections 3.2.1 and 3.2.2. It is an axial-pump with inducer-type blades. Its analysis can be performed in a similar way as for axial compressors with incompressible flows¹ (at most very low compressibility such as that of LH.) We can, however, expect some errors in the performance prediction just because of the differences in blade geometries.² From Euler's equation (40), the torque required by an axial compressor can be written as³

$$\tau_{fp1} = J \frac{\mathcal{P}}{\Omega_{f1}} = J \frac{\dot{m}_{fd2} \Delta h}{\Omega_{f1}} = \frac{\dot{m}_{fd2}}{g \Omega_{f1}} u \Delta V_u \quad (95)$$

Figure 18 shows a compressor blade (radial view) which indicates several geometrical parameters. Conditions upstream and downstream of the blade are denoted by *a* and *b* subscripts respectively.

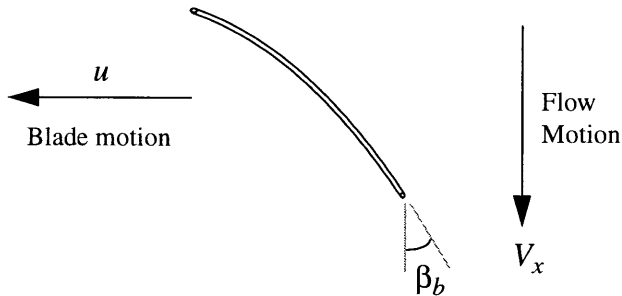


FIGURE 18. Compressor Blade

With this notation, equation (95) takes the following form

$$\tau_{fp1} = \frac{\dot{m}_{fd2}}{g} (R_b V_b - R_a V_a) \quad (96)$$

1. See for example ref. [9]

2. The inducer blades are long-spirals along the shaft, while the compressor's are "flat" turbine-like.

3. Note that the mass flow through the pump of the LPFTP is the same as for the HPTFP.

V_x is the axial velocity at which the fluid leaves the blade. Let us assume that the fluid enters with velocity in the x direction only, therefore $V_a = 0$. We also note from **Figure 18** that the net tangential velocity at the blade exit is given by

$$V_b = u - V_x \tan \beta_b \quad \text{where} \quad u = \Omega_{f1} R_b$$

Introducing the definition of the flow coefficient into our analysis:

$$\phi_{f1} = \frac{1}{\rho_f} \frac{\dot{m}_{fd2}}{\Omega_{f1}} \quad (97)$$

In (97), the LH density is averaged under less severe pressure conditions than in (59), from tables we take $\rho_f = 2.5 \times 10^{-3}$ lbm-in $^{-3}$. After some manipulation and using the continuity equation $\dot{m}_{fd2} = \rho_f V_x A_b$, where A_b is the blade exit annular flow area, (96) can be written as

$$\tau_{fp1} = \frac{1}{g} \rho_f R_b^2 \Omega_{f1}^2 \phi_{f1} \left(1 - \frac{\phi_{f1}}{R_b A_b} \tan \beta_b \right) \quad (98)$$

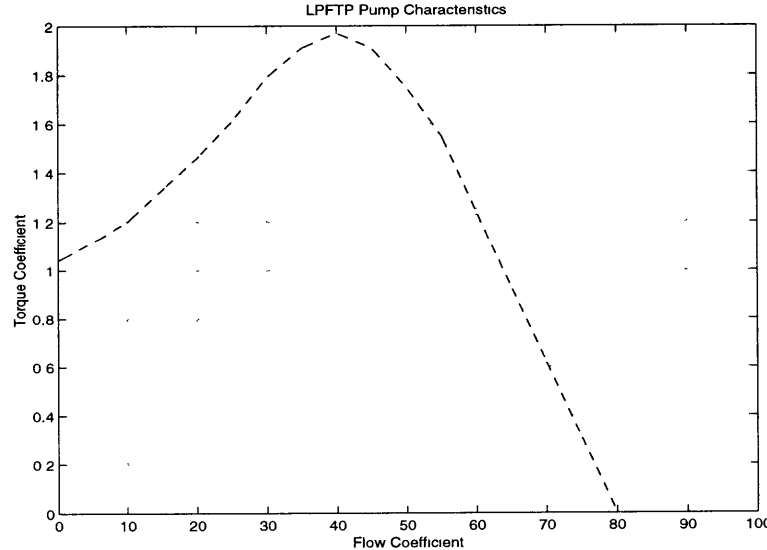


FIGURE 19. Torque Coefficient vs. Flow Coefficient for the LPFTP

The same equation is described in [3] as

$$\tau_{fp1} = 0.002561 \Omega_{f1}^2 \Gamma_{fp1}[\phi_{f1}] \quad (99)$$

where the torque coefficient $\Gamma_{fp1}[\phi_{f1}]$ appears as the dashed line in **Figure 19**.

3.2.4 Low Pressure Oxidizer Turbopump Speed (Ω_{o1})

Much that has been said for the LPFTP in section 3.2.3 can be applied to the LPOTP. The SSME initial pressure requirements established the need for this turbopump as well. The purpose is the same, but their characteristics are quite different. The LPOTP makes use of a multi-stage hydraulic turbine driven with LOX diverted from part of the flow through the HPOTP¹. Hydraulic turbines are relatively less efficient than gas turbines, but their use in the LPOTP represented a great advantage in the developing process as complex seals were not needed to isolate the pumped fluid from the turbine fluid. As a result, safety concerns were reduced; using hydrogen gas instead would very likely react in catastrophic ways if leaking occurs. After driving the turbine, the LOX is diverted back to the pump volute where it adds to the rest of the pumped fluid.

Angular velocity of the LPOTP is described with a type 1 equation:

$$I_{o1} \frac{d\Omega_{o1}}{dt} = \tau_{ot1} - \tau_{op1} \quad (100)$$

where

I_{o1} is the moment of inertia of the LPOTP rotor (lbf-in-sec²)

Ω_{o1} is the angular velocity of the LPOTP shaft (rad/sec)

τ_{ot1} is the torque generated by the 6-staged LPOTP axial-flow hydraulic turbine (lbf-in)

τ_{op1} is the required torque of the LPOTP inducer-type, axial-flow pump (lbf-in)

1. See equation (74)

The rotor inertia is $I_{o1} = \frac{1}{0.37566}$ lbf-in-sec²

3.2.4.1 LPOTP Turbine Section

A hydraulic turbine can be characterized in a similar way as a gas turbine. Let us assume that in the first stage of the turbine, LOX reaches the stator which turns the flow to an angle β_a . The rotational energy is then used by the rotor to power the turbine. The fluid leaves the rotor at an angle β_b (with respect to the moving blades), and enters an identical second stage; the work transfer process is therefore repeated for the six stages of the LPOTP turbine. **Figure 20** shows a diagram of the LOX flow through a single stage of the turbine; R_m is the mean radius of the turbine.

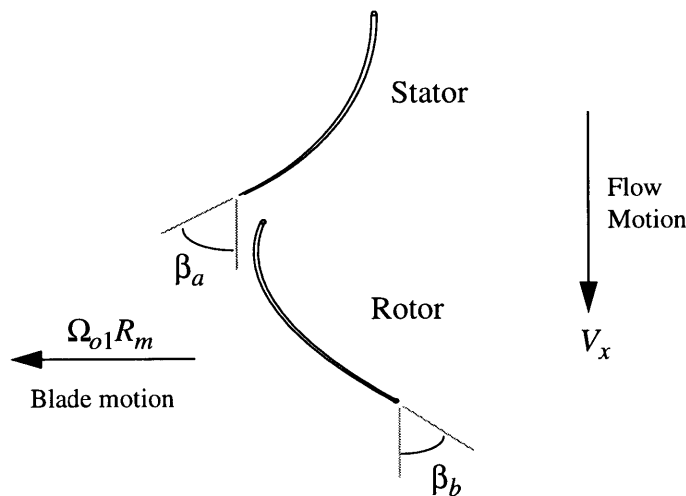


FIGURE 20. LPOTP Hydraulic Turbine Blading

Now we can make use of Euler's equation (40). Assuming that the axial velocity V_x remains constant, the torque delivered is (mean radius analysis, per stage)

$$\tau_{ot1} = \frac{R_m \dot{m}_{ot1}}{g} (V_a - V_b) \quad (101)$$

where

$$V_a = V_x \tan \beta_a \quad \text{and} \quad V_b = \Omega_{o1} R_m - V_x \tan \beta_b$$

Including the effect of the six stages and noting that the axial flow velocity determines the mass flow rate through the continuity equation $\dot{m}_{ot1} = \rho_{ox} V_x A$, it is straight forward to prove that (101) can be written as

$$\tau_{ot1} = \frac{6R_m^2 \dot{m}_{ot1}^2}{g} \left[\frac{\tan \beta_a + \tan \beta_b}{\rho_{ox} R_m A} - \phi_{ot1} \right] \quad (102)$$

where A is the turbine effective-flow annular area and ϕ_{ot1} can be defined as a flow coefficient with the following general dependence

$$\phi_{ot1} \equiv \frac{\Omega_{o1}}{\dot{m}_{ot1}} \quad (103)$$

There are several ways in which equations (102) and (103) can be written. In [3] they are given by

$$\tau_{ot1} = 0.6291 \dot{m}_{ot1}^2 \Gamma_{ot1}[\phi_{ot1}] \quad \text{with} \quad \phi_{ot1} = 0.1467 \frac{\Omega_{o1}}{\dot{m}_{ot1}} \quad (104)$$

where the torque coefficient function Γ_{ot1} is shown as the dashed line in **Figure 21** as described in [3]. Numerical values for the LPOTP were not available; we however, can see that at least the same linear behavior is functionally shown in equation (102).

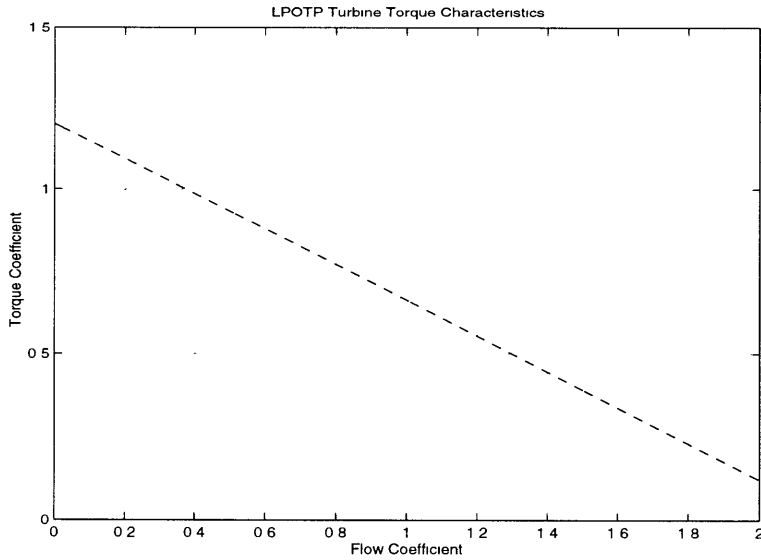


FIGURE 21. LPOTP Turbine Torque Coefficient vs. Flow Coefficient

3.2.4.2 LPOTP Pump Section

The pump section of the LPOTP has two blade rows with different number and geometry, and it can be described essentially in the same way as it was done for the LPFTP. The required torque for driving the pump is then

$$\tau_{op1} = \frac{2}{g} \rho_{ox} R_b^2 \Omega_{o1}^2 \phi_{ox1} \left(1 - \frac{\phi_{ox1}}{R_b A_b} \tan \beta_b \right) \quad (105)$$

We kept the same notation that led to (98) and included the effect of the two blade rows. From **Figure 1** we note that $\dot{m}_{mov} = \dot{m}_{op2} - \dot{m}_{ot1} - \dot{m}_{op3}$, but as the turbine flow is added, the pumped flow is $\dot{m}_{op2} - \dot{m}_{ot1}$. With this in mind, the flow coefficient for the LPOTP pump can be written as

$$\phi_{ox1} = \frac{1}{\rho_{ox}} \frac{\dot{m}_{mov} + \dot{m}_{op3}}{\Omega_{o1}} \quad (106)$$

The HPOTP boost pump flow rate \dot{m}_{op3} and the MOV valve flow rate \dot{m}_{mov} are derived in sections 3.2.5 and 3.2.6 respectively. In [3], (105) is written as

$$\tau_{op1} = 0.0405 \Omega_{o1}^2 \Gamma_{op1}[\phi_{ox1}] \quad (107)$$

The dashed line in **Figure 22** shows the torque coefficient $\Gamma_{op1}[\phi_{ox1}]$, as given in [3].

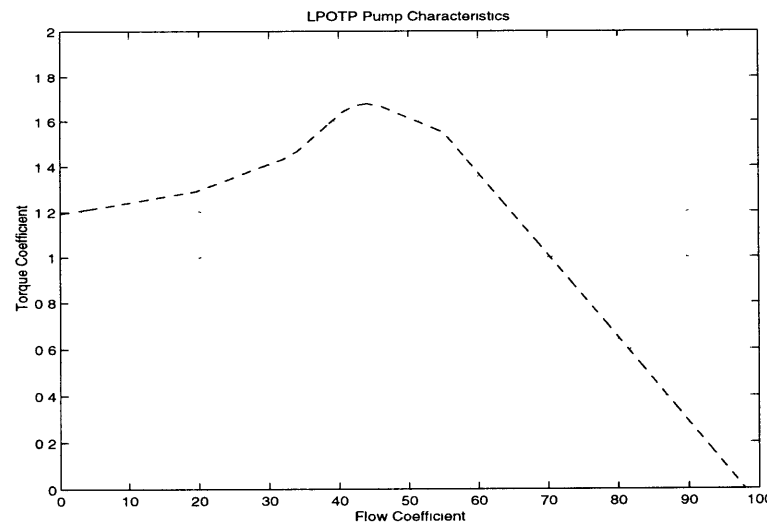


FIGURE 22. Torque Coefficient vs. Flow Coefficient for the LPOTP

3.2.5 HPOTP Boost Pump Oxidizer Flow Rate (\dot{m}_{op3})

As explained in section 3.2.2, a LOX fraction (~10%) which is initially pumped by the HPOTP, is diverted into a compact centrifugal stage mounted at one end of the shaft that connects the HPOTP main pump with the turbine (boost pump, refer to **Figure 1**). The role of this pump is to increase the LOX pressure prior to injection into the fuel and oxidizer preburners. Very high pressures are attained by introducing this pump (~8000 psia at 109% RPL), thus maximizing the performance of the staged combustion cycle (maximize chamber pressure). Mass flow rates can be described from a type 2 equation:

$$\left(\frac{L}{gA}\right)\frac{d}{dt}\dot{m}_{op3} = P_{od3} - P_{pos} - \frac{\lambda}{2g\rho_{ox}A^2}\dot{m}_{op3}^2 \quad (108)$$

where

L, A and λ are the length and area of the pipe and a non-dim. loss coefficient (in, in²)

\dot{m}_{op3} is the oxidizer mass flow rate through the boost pump (lbm/sec)

P_{od3} is the boost pump discharge pressure (psia)

P_{pos} is the mean pressure of the preburner supply line fed by the boost pump (psia)

ρ_{ox} is the LOX density (lbm/in³)

Using Euler's equation (40) we see that for an incompressible fluid

$$\frac{\Delta P}{\rho} = \frac{1}{g}u\Delta V_u \quad (109)$$

In our case we can use (109) to find the pressure increase in the boost stage. If we consider that the inlet pressure is equal to the HPOTP discharge pressure (P_{od2}), then

$$P_{od3} = P_{od2} + \frac{\rho_{ox}}{g}u\Delta V_u$$

From the torque definition, one can easily verify that

$$u\Delta V_u = g \frac{\tau \Omega}{m} \quad (110)$$

Using this expression along with equation (81) we have that the exit pressure is

$$P_{od3} = P_{od2} + \frac{\rho_{ox3}}{g} R_p^2 \Omega_{o2}^2 \left(1 - \phi_{ox3} \frac{\tan \beta}{2\pi(1-f_b)R_p^2 B} \right) \quad (111)$$

In [3], this equation is expressed as

$$P_{od3} = P_{od2} + 0.03869 \Omega_{o2}^2 \Psi_{op3}[\phi_{ox3}] \quad (112)$$

where the function Ψ_{op3} , called the *Head Coefficient*, was extracted from [3] and is shown as the dashed line in **Figure 23a**. The solid line represents Ψ_{op3} as given in (111) with the not-very-accurate information about the boost stage dimensions and properties. We see, however that in the operational region (**Figure 23b**), both curves exhibit at least the same linear behavior in ϕ_{ox3} .

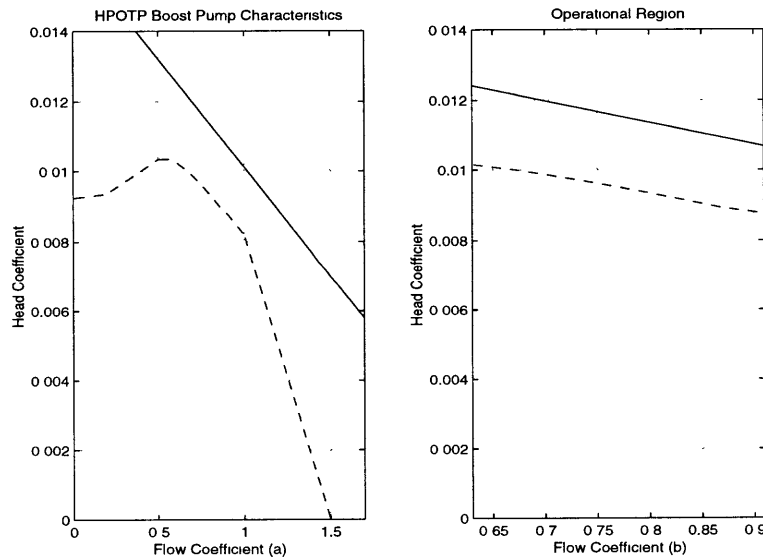


FIGURE 23. Head Coefficient vs. Flow Coefficient for the HPOTP Boost Stage

Equation (111) is applicable only when we know the HPOTP discharge pressure P_{od2} , which can be found by extending the same reasoning as before. Repeating the analysis yields

$$P_{od2} = P_{od1} + \frac{\rho_{ox}}{g} R_p^2 \Omega_{o2}^2 \left(1 - \phi_{ox2} \frac{\tan \beta}{4\pi(1-f_b)R_p^2 B} \right) \quad (113)$$

where, obviously, the specific geometric parameters such as pump radius, blade angle, blockage and impeller width are now those of the HPOTP. P_{od1} is the exit pressure of the LPOTP, which can be found with the same strategy from (105)

$$P_{od1} = P_{os} + \frac{2}{g} \rho_{ox} R_b^2 \Omega_{o1}^2 \left(1 - \frac{\phi_{ox1}}{R_b A_b} \tan \beta_b \right) \quad (114)$$

where P_{os} is the LPOTP inlet pressure (see section 3.2.27) and the geometrical parameters are those of the LPOTP pump (see section 3.2.4).

In [3], equations (113) and (114) are given respectively by

$$P_{od2} = P_{od1} + 0.04122 \Omega_{o2}^2 \Psi_{op2}[\phi_{ox2}] \quad (115)$$

$$P_{od1} = P_{os} + 0.041067 \Omega_{o1}^2 \Psi_{op1}[\phi_{ox1}] \quad (116)$$

Dashed lines in **Figures 24a** and **24b** show the head coefficients as functions of the flow coefficient from equations (115) and (116) respectively.

The pressure P_{pos} is described in section 3.2.22 Finally, the constant coefficients of (108) are given in [3] by

$$\frac{L}{gA} = 0.01 \quad \text{and} \quad \frac{\lambda}{2g\rho_{ox}A^2} = 0.000813$$

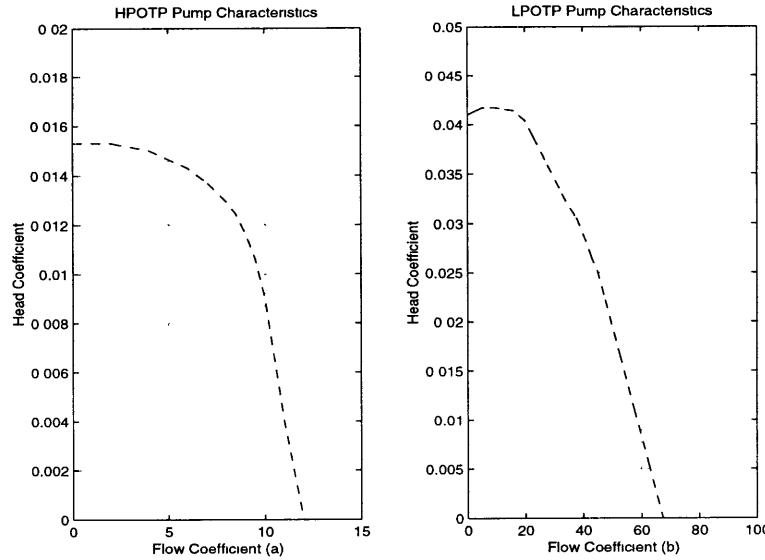


FIGURE 24. Head Coefficient vs. Flow Coefficient for the HPOTP and the LPOTP

3.2.6 Main Oxidizer Valve Flow Rate (\dot{m}_{mov})

As described by (74), the main stage of the HPOTP pump diverts most of the LOX through the MOV directly into the oxidizer injectors of the MCC.

The MOV valve is opened at 100% during engine operation at any RPL. A type 2 equation can be applied:

$$\left(\frac{L}{gA}\right)\frac{d}{dt}\dot{m}_{mov} = P_{od2} - P_c - f(A)_{mov}\dot{m}_{mov}^2 - \left[\frac{\lambda}{2g\rho_{ox}A^2}\right]_{\text{pipe}}\dot{m}_{mov}^2 \quad (117)$$

where

\dot{m}_{mov} is the oxidizer mass flow rate through the MOV valve (lbm/sec)

P_{od2} is the mean pressure of the preburner supply line fed by the boost pump (psia)

P_c is the Main Combustor Chamber pressure (psia)

$f(A)_{mov}$ is the pressure drop term for the MOV valve

$[]_{\text{pipe}}$ is the flow/friction term of the LOX supply pipe and main injector

L , A and λ are the length and area of the pipe and a non-dim. loss coefficient (in, in²)

This flow is induced by the difference in pressure from the exit of the HPOTP pump (P_{od2} , from equation (113)) and the MCC (P_c , see section 3.2.29).

Frictional losses along the pipe cause a pressure drop given by the last term in equation (117), where the constant coefficient is given in [3] by¹

$$\left[\frac{\lambda}{2g\rho_{ox}A^2} \right]_{\text{pipe}} = 0.0003573$$

Pressure losses are also present in the valve subsystem; this accounts for the purpose of the third term in the rhs of equation (117). However, the flow area in the valve is a variable quantity which depends on the situation of the valve mechanism.

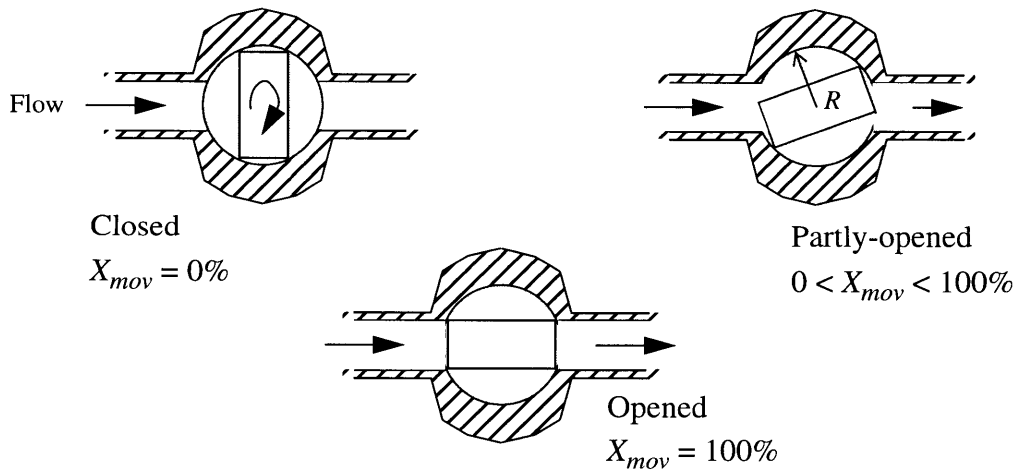


FIGURE 25. Simplified Schematic of a Drop-Ball Valve

-
1. This quantity needs to be considered as an averaged value for the friction term, since in reality the pipe is not of constant area and roughness. Included in this coefficient is also the effect of the LOX main injector, which is a set of small cylindrical elements each with a definite cross-sectional area and frictional properties. We just have to be very careful when trying to identify “pipe” parameters with the real flow parameters. This comment applies as well for the rest of equations that involve “pipe” flow.

Control valves in the SSME are of the *drop-ball* kind, in which a compact (circular cross-section) tube contained inside the rotating “ball” turns to modulate the amount of fluid allowed to pass through the valve. Valves are in no way a trivial component of a rocket engine, on the contrary, their design involves numerous considerations and trade studies. Manufacturing and implementation is as complex as any other part of the engine and in some instances more critical. **Figure 25** shows a simplified schematic of a drop-ball valve in operation. If we assume that the circular tube inside the ball and the pipe have the same cross-sectional area, then we can perform a geometrical analysis to find the *normalized area* which is the ratio of effective flow area (A) to total flow area (A_t) in terms of the parameter X_{mov} (the valve position) which is defined as the fraction of turning required to completely open the valve (see **Figure 25**). With these considerations we have that

$$\frac{A}{A_t} = \left(1 - \frac{\theta}{\theta_c}\right) - \frac{1}{\pi} \sin \left[\pi \left(1 - \frac{\theta}{\theta_c}\right) \right] \quad \text{for} \quad \theta < \theta_c \quad (118)$$

$$\frac{A}{A_t} = 0 \quad \text{for} \quad \theta \geq \theta_c$$

$$\text{where} \quad \theta = \frac{\pi}{2}(1 - X_{mov}) \quad \text{and} \quad \theta_c = 2 \arcsin \frac{r}{R}$$

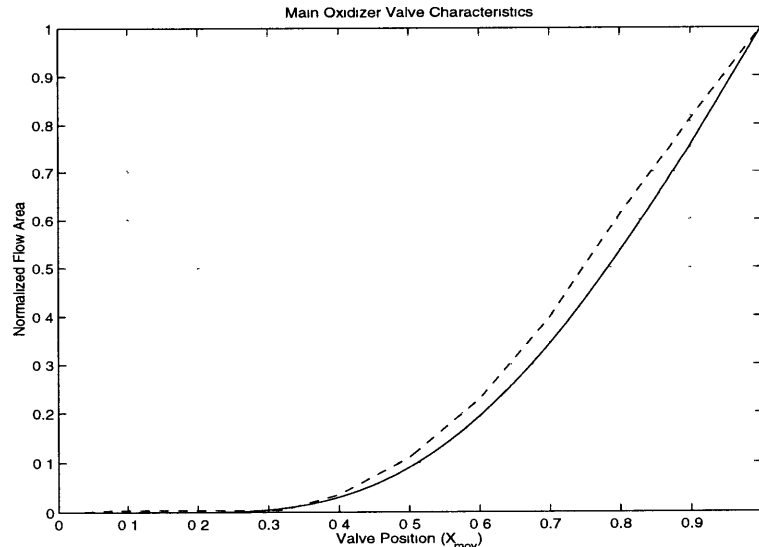


FIGURE 26. Main Oxidizer Valve Characteristics

In this equation, r and R are the radius of the pipe and of the ball mechanism respectively.

From Ref. [10], we estimated that $\frac{r}{R} = 0.6$. The solid line in **Figure 26** shows (118)

with this value while the dashed is the MOV valve characteristics extracted from [3].

To find an expression for the MOV flow term of equation (117), we can assume a simple non-frictional flow through an area-varying pipe section as shown in **Figure 27**. In our case the value of A can go from zero for a completely closed valve to A_t , the nominal total flow area.

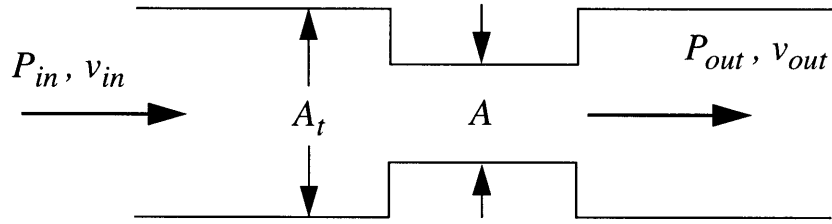


FIGURE 27. Simple Geometry for Propellant Flow Through a Control Valve

If we assume also that there is no pressure recovery, then the pressure downstream is the same as in the obstruction that reduces the flow area from A_t to A ; application of Bernoulli's equation yields

$$P_{in} + \frac{\rho_{ox}v_{in}^2}{2g} = P_{out} + \frac{\rho_{ox}v_{out}^2}{2g}$$

which can be combined with the continuity principle $\dot{m}_{mov} = \rho_{ox}v_{in}A_t = \rho_{ox}v_{out}A$ to find an expression relating pressure drop with mass flow rate. Once this expression is obtained, a simple comparison with (117) shows that

$$f(A)_{mov} = \frac{1}{2g\rho_{ox}A_t^2} \left[\left(\frac{A_t}{A} \right)^2 - 1 \right]$$

In [3], the MOV flow term is given by

$$f(A)_{mov} = 0.001358 \left(\frac{A_t}{A} \right)^2$$

As we can see, there is a difference between these results; it is not clear why in [3] the constant contribution to the pressure drop has been ignored. On the other hand, maybe it is included in the pipe flow/friction term of (117). Other explanation could be simply that the valve flow area is never exactly the same as the nominal total flow area, in this case there will always be a small pressure drop even when the valve is 100% opened. In any case, a good knowledge of the valve characteristics is essential to understand and develop an accurate dynamic model.

Finally, the constant coefficient of the first term of (117) is given in [3] by $\frac{L}{gA} = 0.04$

3.2.7 Fuel Preburner Oxidizer Flow Rate (\dot{m}_{fpo})

As was already described, the boost stage of the HPOTP increases the pressure of an oxidizer fraction before injection into the SSME preburners. Accurate control of these flows is of great importance for the engine functioning.

Prior to injection to the Fuel Preburner (FP), a fraction of \dot{m}_{op3} is diverted into a pipe which contains a controlling valve; the Fuel Preburner Valve (FPV). Its main purpose is to maintain a mixture ratio (O/F by mass) of 6:1 in the MCC. A type 2 equation can be used:

$$\left(\frac{L}{gA} \right) \frac{d}{dt} \dot{m}_{fpo} = P_{pos} - P_{FP} - f(A)_{fpv} \dot{m}_{fpo}^2 - \left[\frac{\lambda}{2g\rho_{ox}A^2} \right]_{\text{pipe}} \dot{m}_{fpo}^2 \quad (119)$$

where

\dot{m}_{fpo} is the oxidizer mass flow rate injected into the fuel preburner (lbm/sec)

P_{pos} is the mean pressure of the preburner supply line fed by the boost pump (psia)

P_{FP} is the fuel preburner pressure (psia)

$f(A)_{fpv}$ is the pressure drop term for the FPV valve

$[]_{\text{pipe}}$ is the flow/friction term of the fuel preburner LOX supply pipe and injector

L , A and λ are the length and area of the pipe and a non-dim. loss coefficient (in, in²)

Calculation of P_{pos} is described in section 3.2.22, while P_{FP} can be found in section 3.2.24.

Constant coefficients for this equation are given in [3] by¹

$$f(A)_{fpv} = 0.02488 \left(\frac{A_t}{A} \right)^2 \quad \left[\frac{\lambda}{2g\rho_{ox}A^2} \right]_{\text{pipe}} = 0.1948 \quad \frac{L}{gA} = 0.5$$

while the normalized area, as function of valve position (X_{fpv}), is shown in **Figure 28** as the dashed line taken from [3].

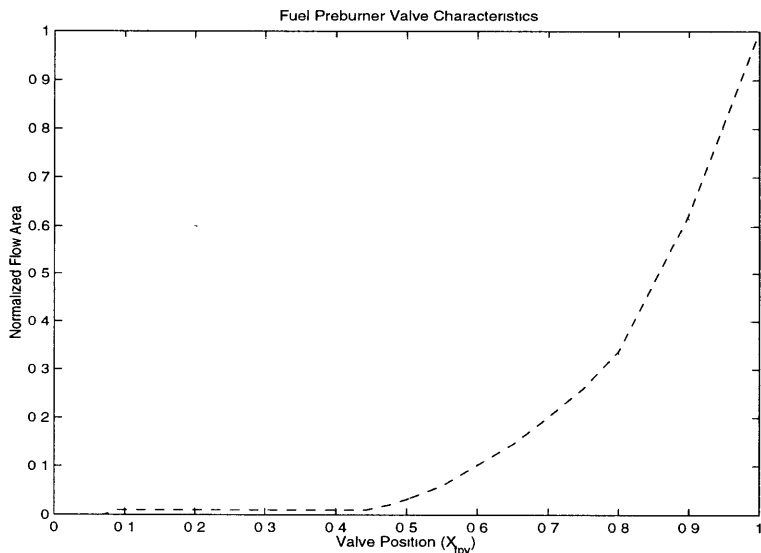


FIGURE 28. Fuel Preburner Valve Characteristics

1. Including effects of preburner LOX injector.

3.2.8 Oxidizer Preburner Oxidizer Flow Rate (\dot{m}_{opo})

A second fraction of \dot{m}_{op3} is now diverted into a pipe which contains another controlling valve, the Oxidizer Preburner Valve (OPV), before being injected into the oxidizer preburner (OP). The main purpose of the OPV is to throttle up or down the engine power level.¹ A type 2 equation can be applied here:

$$\left(\frac{L}{gA}\right)\frac{d}{dt}\dot{m}_{opo} = P_{pos} - P_{OP} - f(A)_{opv}\dot{m}_{opo}^2 - \left[\frac{\lambda}{2g\rho_{ox}A^2}\right]_{\text{pipe}}\dot{m}_{opo}^2 \quad (120)$$

where

\dot{m}_{opo} is the oxidizer mass flow rate injected into the fuel preburner (lbm/sec)

P_{pos} is the mean pressure of the preburner supply line fed by the boost pump (psia)

P_{OP} is the oxidizer preburner pressure (psia)

$f(A)_{opv}$ is the pressure drop term for the OPV valve

$[]_{\text{pipe}}$ is the flow/friction term of the oxidizer preburner LOX supply pipe and injector

L , A and λ are the length and area of the pipe and a non-dim. loss coefficient (in, in²)

Calculation of P_{pos} is described in section 3.2.22, while the one for P_{OP} can be found in section 3.2.23.

Constant coefficients for this equation are given in [3] by²

$$f(A)_{opv} = 0.26\left(\frac{A_t}{A}\right)^2 \quad \left[\frac{\lambda}{2g\rho_{ox}A^2}\right]_{\text{pipe}} = 1.463 \quad \frac{L}{gA} = 1$$

and the normalized area, as function of valve position (X_{opv}), is shown as the dashed line in **Figure 29** taken from [3].

-
1. A feedback mechanism is implemented between the FPV and the OPV to control the overall performance of the SSME.
 2. Including the effect of preburner LOX injector.

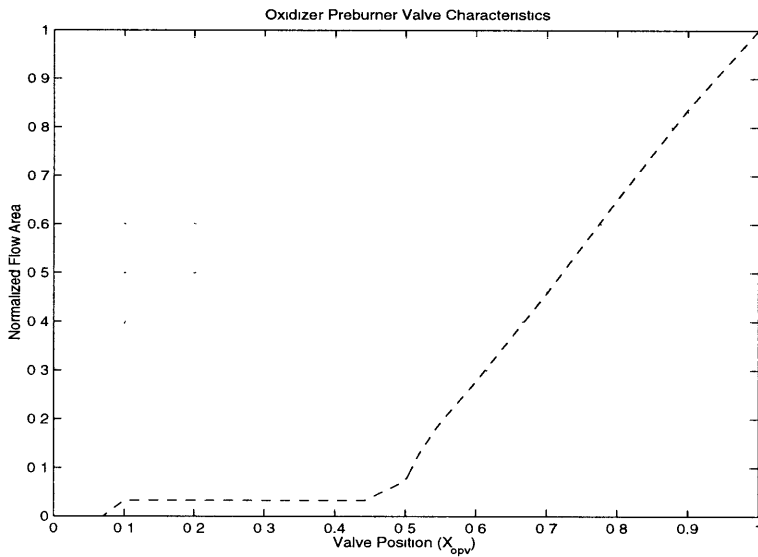


FIGURE 29. Oxidizer Preburner Valve Characteristics

3.2.9 Coolant Liner Inlet Flow Rate (\dot{m}_{cli})

The HPFTP shaft is mounted over two sets of bearings which are operated at extreme conditions. Frictional heating is a significant factor that was taken into account while designing the turbomachinery; therefore, cooling of rotating parts, namely, ball bearings, was of fundamental importance. In order to simplify the design, it was decided that the best solution was to cool the bearings with LH after it leaves the pump section of the HPFTP. In this way, a very small fraction of LH is diverted into the turbopump casing, taking out heat from the pump bearings while it quickly gasifies. After that, this flow is used to cool other parts of the turbine assembly before finally being injected at the turbine exhaust, where the pressure is well below the coolant gas pressure, thus assuring the absence of back-flow. Trying to describe the fluid flow through the cooling passages inside the HPFTP casing just in the same way as for smooth-flow inside a pipe can be futile, therefore it is useful to lump the cavities properties into effective values and name this effective pipe the *coolant liner*. Therefore we have to bear in mind that when we talk about liner flow properties or dimensions we are referring to a non-existent entity which happens to behave in a very close way to the real cooling passages.

The first liner equation comes from a type 2, which is written in terms of the inlet properties:

$$\left(\frac{L}{gA}\right)\frac{d}{dt}\dot{m}_{cli} = P_{fd2} - P_{cl} - \left[\frac{\lambda}{2g\rho_f A^2}\right]_{\text{liner,in}} \dot{m}_{cli}^2 \quad (121)$$

where

\dot{m}_{cli} is the coolant liner inlet flow rate (lbm/sec)

P_{fd2} is the HPFTP discharge pressure (psia)

P_{cl} is the mean pressure of the coolant line (psia)

$[\cdot]_{\text{liner,in}}$ is the flow/friction term of the coolant line inlet

L, A and λ are the length and area of the pipe and a non-dim. loss coefficient (in, in²)

P_{fd2} can be found with the same procedure described in section 3.2.5. Using Euler's equation (40), (110) and (60) we can easily verify that

$$P_{fd2} = P_{fd1} + \frac{3\rho_f}{g} R_p^2 \Omega_{f2}^2 \left(1 - \phi_{f2} \frac{\tan \beta}{2\pi(1-f_b)R_p^2 B} \right) \quad (122)$$

The pump parameters are those described in section 3.2.1. P_{fd1} is the discharge pressure of the LPFTP, which can be found exactly in the same way using (98)

$$P_{fd1} = P_{fs} + \frac{1}{g} \rho_f R_b^2 \Omega_{f1}^2 \left(1 - \frac{\phi_{f1}}{R_b A_b} \tan \beta_b \right) \quad (123)$$

In this equation, the parameters are those described in section 3.2.3. P_{fs} is the LPFTP inlet pressure which can be taken as the fuel tank pressure as it is maintained more or less constant with help of gasified hydrogen which is tapped from the exhaust of the LPFTP turbine.

In [3] it is assumed that $P_{fs} = 45$ psia and (122, 123) are written in the following way

$$P_{fd2} = P_{fd1} + 0.002797 \Omega_{f2}^2 \Psi_{fp2}[\phi_{f2}] \quad (124)$$

$$P_{fd1} = P_{fs} + 0.002011 \Omega_{f1}^2 \Psi_{fp1}[\phi_{f1}] \quad (125)$$

Dashed lines in **Figures 30a** and **30b** show Ψ_{fp2} and Ψ_{fp1} respectively as reported in [3].

The mean liner pressure P_{cl} is discussed in section 3.2.25. Constant coefficients for equation (121) are given in [3] by

$$\left[\frac{\lambda}{2g\rho_f A^2} \right]_{\text{liner,in}} = 6573.46 \quad \frac{L}{gA} = 10$$

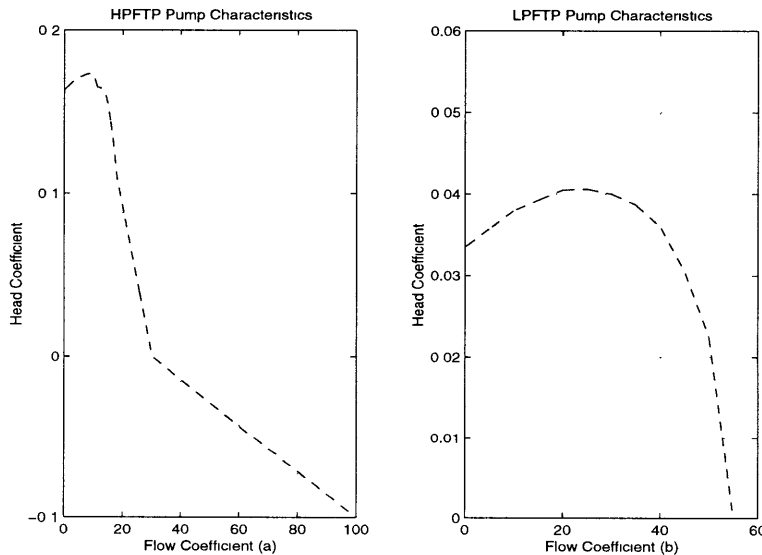


FIGURE 30. Head Coefficient vs. Flow Coefficient for the HPFTP and the LPFTP

3.2.10 Coolant Liner Outlet Flow Rate (\dot{m}_{clo})

The second liner equation comes from a type 2, which is written in terms of the liner exit properties. The coolant flows inside the turbopump to finally mix with the LPFTP turbine exhaust gases; we can consider that conditions prevailing at this point are those of the fuel injector (see **Figure 1**):

$$\left(\frac{L}{gA}\right)\frac{d}{dt}\dot{m}_{clo} = P_{cl} - P_{FI} - \left[\frac{\lambda}{2g\rho_f A^2}\right]_{\text{liner,out}} \dot{m}_{clo}^2 \quad (126)$$

where

\dot{m}_{clo} is the coolant liner outlet flow rate (lbm/sec)

P_{cl} is the HPFTP discharge pressure (psia)

P_{FI} is the mean pressure of the coolant line (psia)

$[\cdot]_{\text{liner,out}}$ is the friction term of the coolant line exit

L, A and λ are the length and area of the pipe and a non-dim. loss coefficient (in, in²)

The mean liner pressure P_{cl} and the fuel injector pressure P_{FI} are defined in sections 3.2.25 and 3.2.28 respectively.

Constant coefficients for equation (126) are given in [3] by

$$\left[\frac{\lambda}{2g\rho_f A^2}\right]_{\text{liner,out}} = 109.59 \quad \frac{L}{gA} = 10$$

3.2.11 Fuel Preburner Fuel Flow Rate (\dot{m}_{fpf})

After being discharged by the HPFTP, fuel is separated in three main paths as described by (64). One of them is used to drive the LPFTP turbine as we saw in section 3.2.3, while the other two are put together after one passes through the CCV valve and the other enters the cooling circuit in the engine nozzle. This flow is then separated once more in two; one of them is diverted into the fuel preburner. This is also a type 2 equation:

$$\left(\frac{L}{gA}\right)\frac{d}{dt}\dot{m}_{fpf} = P_9 - P_{FP} - \left[\frac{\lambda}{2gA^2}\right]_{\text{pipe}} \frac{\dot{m}_{fpf}^2}{\rho_9} \quad (127)$$

where

\dot{m}_{fpf} is the fuel mass flow rate injected into the fuel preburner (lbm/sec)

P_9 is the mean pressure of the preburners fuel supply line (psia)

P_{FP} is the fuel preburner pressure (psia)

ρ_9 is the fuel density in the preburners fuel supply line (lbm-in⁻³)

[]_{pipe} is the friction term of the fuel preburner fuel supply pipe and injector

L , A and λ are the length and area of the pipe and a non-dim. loss coefficient (in, in²)

P_9 and P_{FP} are defined in sections 3.2.26 and 3.2.24 respectively. ρ_9 can be found by performing a simple fuel density weighted average of the mixed flow, namely, the fuel nozzle by-pass flow \dot{m}_{fnbp} (flow through the CCV valve) and the nozzle cooling circuit flow \dot{m}_4 . If these flows have densities ρ_{fnbp} and ρ_4 respectively, then the weighted average ρ_9 is

$$\rho_9 = \frac{\dot{m}_4 + \dot{m}_{fnbp}}{\frac{1}{\rho_4} \dot{m}_4 + \frac{1}{\rho_{fnbp}} \dot{m}_{fnbp}}$$

\dot{m}_{fnbp} , \dot{m}_4 and ρ_4 are described in sections 3.2.16, 3.2.15 and 3.2.31 respectively, while ρ_{fnbp} can be taken as a fuel density average which is not expected to have sensible variations and therefore can be computed from tables [15] once we know that after passing through the MFV valve, the duct system is no longer insulated and the fuel gasifies. Constant coefficients for (127) are given in [3] by

$$\left[\frac{\lambda}{2gA^2} \right]_{\text{pipe}} = 0.000131 \quad \frac{L}{gA} = 0.05 \quad \rho_{fnbp} = 2.69 \times 10^{-3} \text{ lbm-in}^{-3}$$

3.2.12 Oxidizer Preburner Fuel Flow Rate (\dot{m}_{opf})

Another fraction of fuel flow is now diverted into the fuel injector of the oxidizer preburner. Analysis is exactly the same as in section 3.2.11. A type 2 equation is used:

$$\left(\frac{L}{gA}\right)\frac{d}{dt}\dot{m}_{opf} = P_9 - P_{OP} - \left[\frac{\lambda}{2gA^2}\right]_{\text{pipe}} \frac{\dot{m}_{opf}^2}{\rho_9} \quad (128)$$

where

\dot{m}_{opf} is the fuel mass flow rate injected into the oxidizer preburner (lbm/sec)

P_9 is the mean pressure of the preburners fuel supply line (psia)

P_{OP} is the oxidizer preburner pressure (psia)

ρ_9 is the fuel density in the preburners fuel supply line (lbm-in⁻³)

[]_{pipe} is the friction term of the fuel preburner fuel supply pipe and injector

L, A and λ are the length and area of the pipe and a non-dim. loss coefficient (in, in²)

The oxidizer preburner pressure P_{OP} is defined in section 3.2.23 and the constant coefficients are given in [3] by

$$\left[\frac{\lambda}{2gA^2}\right]_{\text{pipe}} = 0.000570 \quad \frac{L}{gA} = 0.1$$

3.2.13 Main Combustion Chamber Heat Exchanger Fuel Flow Rate (\dot{m}_{mc})

As we have already described, high pressure hydrogen discharged from the HPFTP flows through the MFV valve and then is separated into 3 main paths. The MFV is opened at 100% once ignition sequence begins and remains in that position until shutdown occurs. One of the flow fractions (\dot{m}_{mc}) is used to regeneratively cool the MCC as it is diverted to flow inside a cooling jacket. After heated, the flow is used to drive the LPFTP turbine; we can expect that in steady state operation this flow becomes \dot{m}_{ft1} , described in section 3.2.3. A type 2 equation is used once more:

$$\left(\frac{L}{gA}\right)\frac{d}{dt}\dot{m}_{mc} = P_{mfvd} - P_5 - \left[\frac{\lambda}{2gA^2}\right]_{\text{pipe}} \frac{\dot{m}_{mc}^2}{\rho_5} \quad (129)$$

where

\dot{m}_{mc} is the fuel mass flow rate injected into the MCC heat exchanger (lbm/sec)

P_{mfvd} is the MFV valve discharge pressure (psia)

P_5 is the MCC cooling circuit exit pressure (psia)

ρ_5 is the fuel density at the MCC cooling circuit exit (lbm-in⁻³)

[]_{pipe} is the friction term of the MCC cooling circuit

L , A and λ are the length and area of the pipe and a non-dim. loss coefficient (in, in²)

P_{mfvd} can be directly identified with the HPFTP discharge pressure P_{fd2} and taking into account the pressure drop term associated with the MFV valve

$$P_{mfvd} = P_{fd2} - f(A)_{mfv} \dot{m}_{fd2}^2 \quad (130)$$

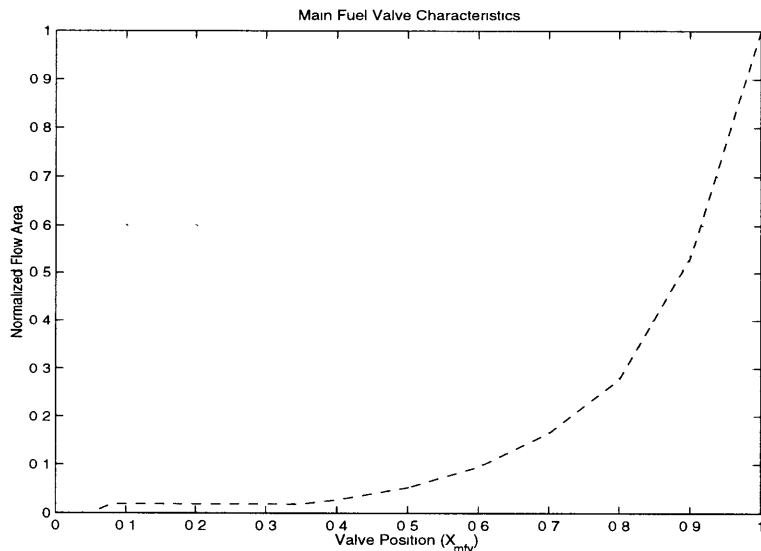


FIGURE 31. Main Fuel Valve Characteristics

\dot{m}_{fd2} and P_{fd2} are given by equations (64) and (124) respectively. ρ_5 is described in section 3.2.30. Constant coefficients are given by

$$f(A)_{mfv} = 0.005347 \left(\frac{A_t}{A} \right)^2 \quad \frac{L}{gA} = 0.2$$

where the normalized flow area (A/A_t) is shown in **Figure 31** as a function of the MFV valve position (X_{mfv}).

3.2.14 Nozzle Heat Exchanger Outlet Fuel Flow Rate (\dot{m}_{fn})

Another fraction of fuel discharged from the MFV valve is used to regeneratively cool the nozzle walls as it is separated into 1,080 individual tubes welded together. This is also a type 2 equation:

$$\left(\frac{L}{gA} \right) \frac{d}{dt} \dot{m}_{fn} = P_{mfvd} - P_4 - \left[\frac{\lambda}{2g\rho_f A^2} \right]_{\text{pipe}} \dot{m}_{fn}^2 \quad (131)$$

where

\dot{m}_{fn} is the fuel mass flow rate injected into the nozzle heat exchanger (lbm/sec)

P_{mfvd} is the MFV valve discharge pressure (psia)

P_4 is the nozzle cooling circuit exit pressure (psia)

$[]_{\text{pipe}}$ is the flow/friction term of the nozzle cooling circuit

L, A and λ are the length and area of the pipe and a non-dim. loss coefficient (in, in²)

P_{mfvd} is given in equation (130). P_4 can be found from tables [15] as function of SU_4 and ρ_4 which are described in sections 3.2.33 and 3.2.31 respectively. Inside the cooling circuit, the flow can be very irregular both in structural and thermodynamic aspects as fuel properties change from point to point along the passages. Intuitively we would assume that the nozzle friction term would depart from a constant value. In [3], variations are considered as a correction function obtained from empirical data. $[]_{\text{pipe}}$ is then represented as a function of gas exit pressure P_4 , which is shown as the dashed line in **Figure 32**. The form of this curve suggests that two-phase flow may exist at this particular

location with mixed properties; because in a perfect liquid (constant density) the flow/friction term should remain unchanged whereas in a perfect gas the dependence is proportional to P^{-1} at constant temperature. Trying to derive this kind of corrections from first principles is a very difficult matter. In any case, experimentation provides reliable data that can be fitted to be used in the model development. If empirical information is not available (for example, when designing a dynamic model of an untested engine), then an approximation of the fluid equation of state should be made based on the expected operational conditions.

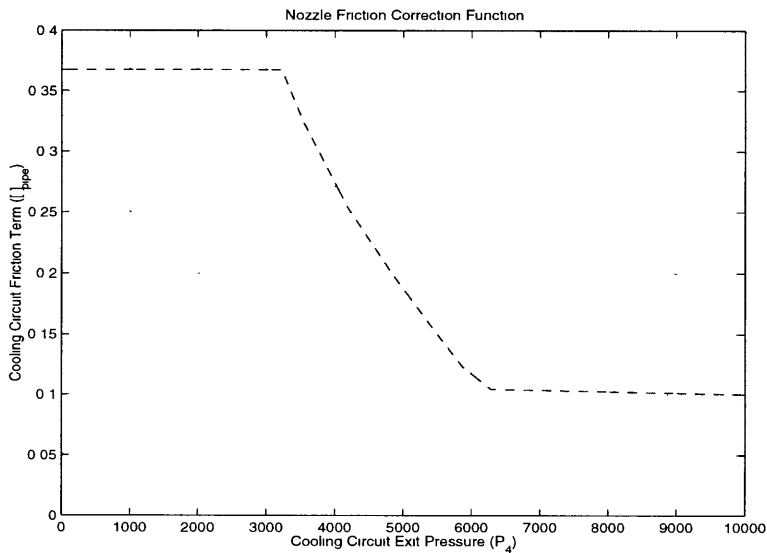


FIGURE 32. Nozzle Cooling Circuit Friction Correction Function

The constant coefficient in (131) is given in [3] by $\frac{L}{gA} = 0.0667$

3.2.15 Nozzle Heat Exchanger Outlet Fuel Flow Rate (\dot{m}_4)

Just after leaving the nozzle cooling circuit, fuel is mixed with more fuel discharged from the CCV valve and sent directly to the preburners fuel supply line. A type 2 equation is once more needed here:

$$\left(\frac{L}{gA}\right)\frac{d}{dt}\dot{m}_4 = P_4 - P_9 - \left[\frac{\lambda}{2gA^2}\right]_{\text{pipe}} \frac{\dot{m}_4^2}{\rho_4} \quad (132)$$

where

\dot{m}_4 is the fuel mass flow rate at the exit of the nozzle heat exchanger (lbm/sec)

P_4 is the nozzle cooling circuit exit pressure (psia)

P_9 is the preburners fuel supply line mean pressure (psia)

ρ_4 is the fuel density in the nozzle cooling circuit exit duct (lbm-in⁻³)

[]_{pipe} is the flow/friction term of the nozzle cooling circuit exit duct

L , A and λ are the length and area of the pipe and a non-dim. loss coefficient (in, in²)

It is clear that the flow is “powered” by the difference in pressure from P_4 (taken from tables as described in 3.2.14) to P_9 (defined in section 3.2.26). The fuel density ρ_4 is defined in section 3.2.31.

Once more the problem reduces to quantifying the friction term as the flow properties change when it is mixed with the fuel discharged by the CCV valve. Losses are accounted for in an empirical correction function described in [3] which depends on P_4 . This function is shown as the dashed line in **Figure 33**. From first principles is hard to understand the reasons for the shape of this function; given that this particular pipe carries gasified hydrogen we would think that its value should be more or less constant, however this is not the case, there is an initial, non-negligible (almost six-fold) increase of the flow/friction term from 3000 to 6200 psi, and suddenly, there is practically linear decrease after that. It would not be surprising that the origin of this correction factor have nothing to do with the thermodynamic properties of the flow but with the mechanical operation of the engine, such as the control sequence of valves and other components.

And the constant coefficient for (132) is given in [3] by $\frac{L}{gA} = 0.0472$

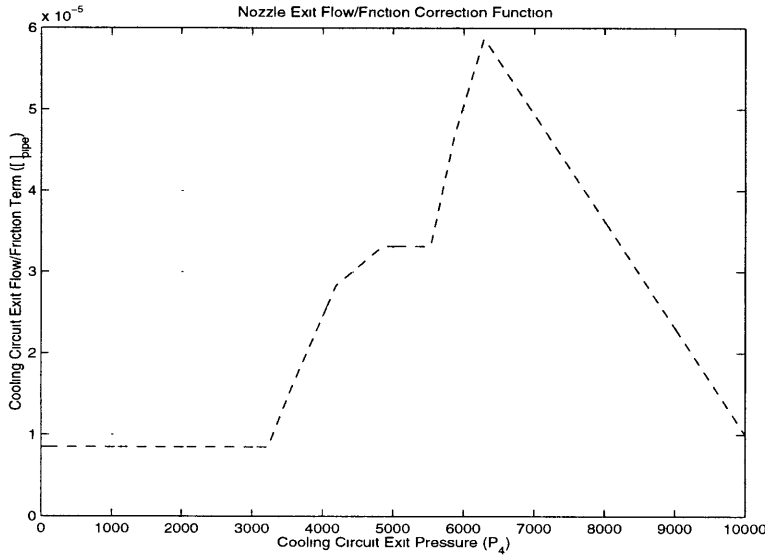


FIGURE 33. Nozzle Cooling Circuit Exit Flow/Friction Correction Function

3.2.16 Nozzle Heat Exchanger Bypass Fuel Flow Rate (\dot{m}_{fnbp})

The third main flow given in (64) is diverted into the CCV valve which function is to control the amount of fuel that is allowed to move into the nozzle heat exchanger so an adequate gas temperature rise could be achieved before injecting it into the preburners. This valve enters in closed-loop operation along with the FPV and OPV valves to control the overall performance of the SSME. A type 2 equation is used:

$$\left(\frac{L}{gA}\right)\frac{d}{dt}\dot{m}_{fnbp} = P_{mfvd} - P_9 - f(A)_{ccv}\dot{m}_{fnbp}^2 \quad (133)$$

where

\dot{m}_{fnbp} is the fuel mass flow rate through the nozzle heat exchanger bypass (lbm/sec)

P_{mfvd} is the MFV valve discharge pressure (psia)

P_9 is the preburners fuel supply line mean pressure (psia)

$f(A)_{ccv}$ is the pressure drop term for the CCV valve

L, A and λ are the length and area of the pipe and a non-dim. loss coefficient (in, in²)

P_{mfvd} is calculated with equation (130) while P_9 is defined in section 3.3.26.

Constant coefficients are given by

$$f(A)_{ccv} = 0.1297 \left(\frac{A_t}{A} \right)^2 \quad \frac{L}{gA} = 5$$

where the normalized flow area (A/A_t) is shown in **Figure 34** as a function of the CCV valve position (X_{ccv}).

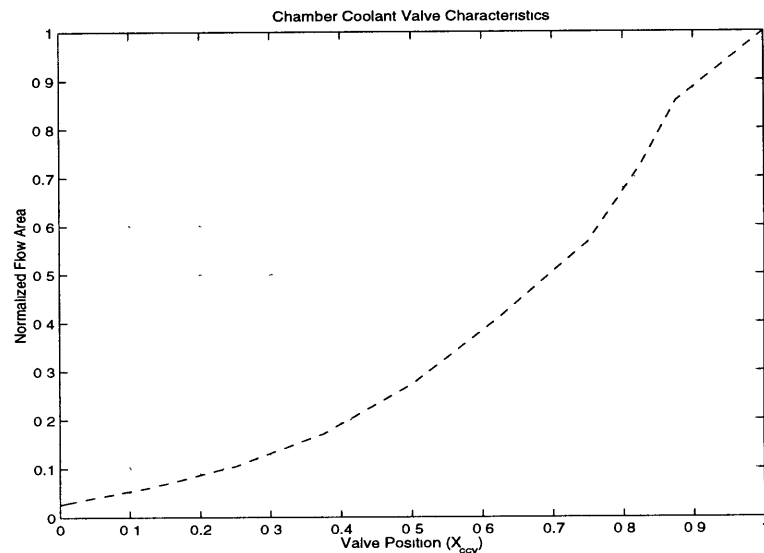


FIGURE 34. Chamber Coolant Valve Characteristics

3.2.17 LPOTP Pump Inlet Oxidizer Flow Rate (\dot{m}_{os})

As explained in section 3.2.4, the LPOTP turbine is driven by LOX which is then added to the main stream of pumped LOX. We can expect a direct interaction between the pumped and the turbine fluids, which are the same, kept always in their liquid phase. A significant inertia is present and fluid oscillations justify the introduction of this flow variable into the dynamic model. This is not completely true in the case of the LPFTP where fluid interaction between the pumped LH and the gasified hydrogen that drives the axial

turbine, is small enough to have negligible contribution to the dynamics. A type 2 equation can be used to describe this flow behavior:

$$\left(\frac{L}{gA}\right)\frac{d}{dt}\dot{m}_{os} = P_{ot} - P_{os} - \left[\frac{\lambda}{2g\rho_{ox}A^2}\right]_{\text{pipe}} \dot{m}_{os}^2 \quad (134)$$

where

\dot{m}_{os} is the LPOTP pump inlet oxidizer flow rate (lbm/sec)

P_{ot} is the oxidizer tank pressure (psia)

P_{os} is the LPOTP pump inlet pressure (psia)

$[]_{\text{pipe}}$ is the friction term of the LPOTP inlet supply line

L, A and λ are the length and area of the pipe and a non-dim. loss coefficient (in, in²)

As was explained in section 3.2.2, the HPOTP tubular heat exchanger takes a very small fraction of LOX to cool the turbopump. In this process, the oxidizer is gasified and taken back to the LOX tank in such a way as to maintain the tank pressure more or less constant over the whole operation of the SSME. Therefore we can take a constant value for this pressure, which is given in [3] by $P_{ot} = 110$ psia. The pump inlet pressure P_{os} is described in section 3.2.27.

The friction term in [3] is written in a different way as compared with the type 2 equations we have developed. Using the definitions given in (2) and the continuity equation $\dot{m}_{os} = \rho_{ox}vA$, we can write (134) as

$$\left(\frac{L}{gA}\right)\frac{d}{dt}\dot{m}_{os} = P_{ot} - P_{os} - \left[\frac{0.0199L^4\mu_{ox}}{\pi\lambda^3\rho_{ox}D^7}\right]_{\text{pipe}} \dot{m}_{os} \quad (135)$$

which is the form described in [3], with constant coefficients

$$\left[\frac{0.0199L^4\mu_{ox}}{\pi\lambda^3\rho_{ox}D^7}\right]_{\text{pipe}} = 0.0112 \quad \frac{L}{gA} = 0.046$$

Written in this form would assume that both viscosity and density of LOX remains constant at the LPOTP inlet. There are no large pressure gradients at this particular point, therefore this assumption is more or less accurate.

3.2.18 LPOTP Hydraulic Turbine Flow Rate (\dot{m}_{ot1})

As is remarked in section 3.2.4, the turbine of the LPOTP is driven by LOX discharged by the HPOTP and carried through a pipe directly into the six-stage hydraulic turbine. We can make use of a type 2 equation:

$$\left(\frac{L}{gA}\right)\frac{d}{dt}\dot{m}_{ot1} = P_{od2} - P_{od1} - C_f \dot{m}_{ot1}^2 \quad (136)$$

where

\dot{m}_{ot1} is the LPOTP hydraulic turbine flow rate (lbm/sec)

P_{od2} is the HPOTP pump discharge pressure (psia)

P_{od1} is the LPOTP pump discharge pressure (psia)

C_f is the pressure loss factor along the pipe and the LPOTP hydraulic turbine

L and A are the length and area of the pipe (in, in²)

\dot{m}_{ot1} , P_{od2} and P_{od1} are given in section 3.2.18, (115) and (114) respectively.

Pressure losses have two sources in this particular case. First, there is the flow/frictional pressure loss due to the pipe that connects the exit of the HPOTP main pump to the inlet of the LPOTP hydraulic turbine. There is also a pressure drop in the turbine related to the work transferred to the pump. In this way, we have that the pressure loss coefficient has the following form

$$C_f = \left[\frac{\lambda}{2g\rho_{ox}A^2} \right]_{\text{pipe}} + f(\phi_{ot1})$$

To find the dependence of the pressure loss coefficient with the flow coefficient, we can use Euler's equation in a form similar to (110) along with the turbine torque described by (102). By doing this, we observe that

$$f(\phi_{ot1}) = \rho_{ox}\phi_{ot1} \frac{6R_m^2}{g} \left[\frac{\tan\beta_a + \tan\beta_b}{\rho_{ox}R_mA} - \phi_{ot1} \right] + f_{geom}$$

where f_{geom} accounts for the pressure loss inside the pump due to the intrinsic flow separation that occurs even when the velocity of the shaft is zero because of the presence of twelve blade rows. The notation in this expression is explained in section 3.2.4. Just as an exercise, we can adjust some values for the turbine to see how well our expression approaches the one described in [3]: $\beta_a = 20^\circ$, $\beta_b = 12^\circ$, $R_m = 1.25\text{in}$, $A = 3\text{in}^2$ (annular area) and $\rho_{ox} = 0.043\text{lbm/in}^3$. We also assume $f_{geom} = 0.004$ in the same way as in [3] to account for the turbine intrinsic pressure loss. The solid line in **Figure 35** shows the result of using these selected values while the dashed represents the hydraulic turbine pressure loss function in terms of the flow coefficient as described in [3].

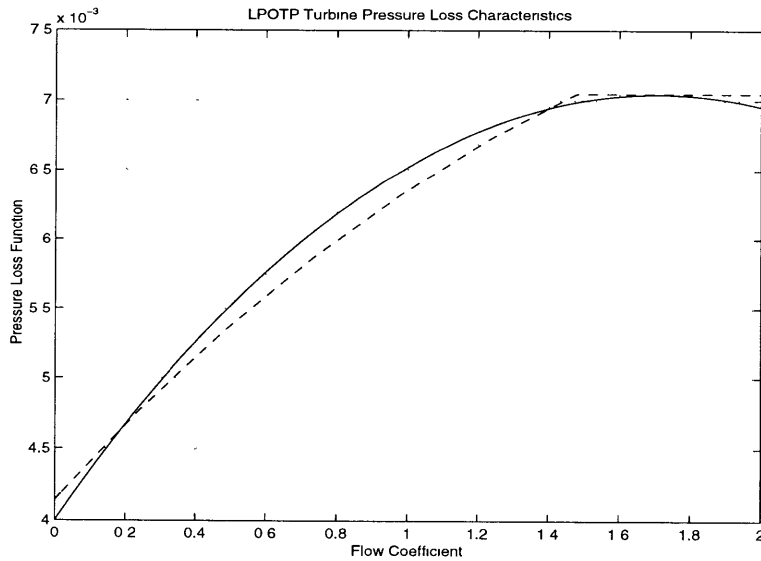


FIGURE 35. LPOTP Pressure Loss Function vs. Flow Coefficient

Finally, constant coefficients for this equation are

$$\left[\frac{\lambda}{2g\rho_{ox}A^2} \right]_{\text{pipe}} = 0.1142 \quad \frac{L}{gA} = 0.833$$

3.2.19 Fuel Preburner Augmented Spark Igniter Flow Rate (\dot{m}_{asifp})

As is described by (64), a small fraction of fuel discharged by the HPFTP is used to feed the Augmented Spark Igniters (ASI). Once the ignition signal is received, ASI flows are directed to each one of the three injectors in the SSME (FP, OP and MCC) along with a very small quantity of LOX; two spark igniters on each injector are then energized, creating a flame which induces the initial burn of propellants injected into the combustion chambers.¹ A type 2 equation is used in this case:

$$\left(\frac{L}{gA} \right) \frac{d}{dt} \dot{m}_{asifp} = P_{mfvd} - P_{FP} - \left[\frac{\lambda}{2g\rho_f A^2} \right]_{\text{pipe}} \dot{m}_{asifp}^2 \quad (137)$$

where

\dot{m}_{asifp} is the fuel preburner ASI flow rate (lbm/sec)

P_{mfvd} is the MFV valve discharge pressure (psia)

P_{FP} is the fuel preburner pressure (psia)

$[]_{\text{pipe}}$ is the friction term of the ASI fuel preburner fuel supply line

L , A and λ are the length and area of the pipe and a non-dim. loss coefficient (in, in²)

P_{mfvd} and P_{FP} are described by equation (130) and in section 3.2.24 respectively, while the constant coefficients of (137) are given in [3] by

$$\left[\frac{\lambda}{2g\rho_f A^2} \right]_{\text{pipe}} = 1072.88 \quad \frac{L}{gA} = 10$$

1. Two ASIs are used for redundancy purposes. It is worthwhile to note that we have not talked about redundant components in the SSME, and the reason is because they are almost nonexistent. Rocket engines have to base their success in high reliability instead; the implementation of redundant hardware would cause prohibitive increases in the launch vehicle's weight.

3.2.20 Oxidizer Preburner Augmented Spark Igniter Flow Rate (\dot{m}_{asiop})

In the same way as in section 3.2.19, for the oxidizer preburner, a type 2 equation can be used:

$$\left(\frac{L}{gA}\right)\frac{d}{dt}\dot{m}_{asiop} = P_{mfvd} - P_{OP} - \left[\frac{\lambda}{2g\rho_f A^2}\right]_{\text{pipe}} \dot{m}_{asiop}^2 \quad (138)$$

where

\dot{m}_{asiop} is the oxidizer preburner ASI flow rate (lbm/sec)

P_{mfvd} is the MFV valve discharge pressure (psia)

P_{OP} is the oxidizer preburner pressure (psia)

[]_{pipe} is the friction term of the ASI oxidizer preburner fuel supply line

L , A and λ are the length and area of the pipe and a non-dim. loss coefficient (in, in²)

P_{mfvd} and P_{OP} are described by equation (130) and in section 3.2.23 respectively, while the constant coefficients of (138) are given in [3] by

$$\left[\frac{\lambda}{2g\rho_f A^2}\right]_{\text{pipe}} = 1025.04 \quad \frac{L}{gA} = 10$$

3.2.21 Main Combustion Chamber Augmented Spark Igniter Flow Rate (\dot{m}_{asimc})

As is explained in section 3.2.19, for the MCC, a type 2 equation can be used:

$$\left(\frac{L}{gA}\right)\frac{d}{dt}\dot{m}_{asimc} = P_{mfvd} - P_c - \left[\frac{\lambda}{2g\rho_f A^2}\right]_{\text{pipe}} \dot{m}_{asimc}^2 \quad (139)$$

where

\dot{m}_{asimc} is the MCC ASI flow rate (lbm/sec)

P_{mfvd} is the MFV valve discharge pressure (psia)

P_c is the MCC pressure (psia)

[]_{pipe} is the friction term of the ASI MCC fuel supply line

L , A and λ are the length and area of the pipe and a non-dim. loss coefficient (in, in²)

P_{mfvd} and P_c are described by equation (130) and in section 3.2.29 respectively, while the constant coefficients of (139) are given in [3] by

$$\left[\frac{\lambda}{2g\rho_f A^2} \right]_{\text{pipe}} = 3552.88 \quad \frac{L}{gA} = 10$$

3.2.22 Preburners Oxidizer Supply Line Pressure (P_{pos})

As we can see from **Figure 1**, the preburners supply line has one input which comes from the HPOTP boost stage exit and two outputs which go directly into the oxidizer and fuel preburners. However, there is a third output, a small LOX quantity is used to cool the bearings of the pump section of the HPOTP. This third output is tapped from the exit of the boost stage, it cools the bearings and then is directed back to the HPOTP inlet. Fluid capacitance can be described using a type 3 equation:

$$\kappa_{ox}\rho_{ox}V\frac{d}{dt}P_{pos} = \dot{m}_{op3} - \dot{m}_{fpo} - \dot{m}_{opo} - \dot{m}_{op2c} \quad (140)$$

where

P_{pos} is the preburners oxidizer supply line pressure (psia)

\dot{m}_{op3} is the oxidizer mass flow rate through the boost pump (lbm/sec)

\dot{m}_{fpo} is the oxidizer mass flow rate injected into the fuel preburner (lbm/sec)

\dot{m}_{opo} is the oxidizer mass flow rate injected into the oxidizer preburner (lbm/sec)

\dot{m}_{op2c} is the HPOTP internal cooling oxidizer mass flow rate (lbm/sec)

V is the preburners oxidizer supply line volume (in³)

κ_{ox} and ρ_{ox} are the LOX compressibility and density (in²/lbf, lbm/in³)

\dot{m}_{op3} , \dot{m}_{fpo} and \dot{m}_{opo} are defined in sections 3.2.5, 3.2.7 and 3.2.8 respectively. To estimate the HPOTP internal coolant flow we can lump together all the geometrical and frictional properties of the complicated channel flow into a simplified model to describe the pressure losses as

$$\Delta P_{loss} = \frac{K}{g} \rho_{ox} u^2 \quad \text{with} \quad u = \frac{\dot{m}_{op2c}}{\rho_{ox} A}$$

where A is the channel effective flow area and K is a generalized loss coefficient which includes all the effects that occur along the flow.¹ If we now assume that this pressure loss is precisely the pressure difference from the exit of the boost stage and the inlet of the LPOTP, then we have that

$$\dot{m}_{op2c} = \sqrt{\frac{g \rho_{ox} A^2}{K} (P_{od3} - P_{od1})} \quad (141)$$

In [3], the constant coefficient of (141) is given by $\frac{g \rho_{ox} A^2}{K} = 0.005727$, which is adequate for the small orifices used by the LOX to cool the turbopump. Also from [3] we see that the constant coefficient of (140) is $\kappa_{ox} \rho_{ox} V = 2.6233 \times 10^{-5}$. If we take the LOX compressibility to be $\kappa_{ox} \approx 3.4 \times 10^{-6}$ in²/lbf, then we can calculate the volume of the pipe using the LOX density given in section 3.2.2: $V \approx 179.43$ in³. Using this volume and also the constant coefficients from [3] of section 3.2.5 we see that the pipe dimensions and friction characteristics are close to

$$L \approx 27 \text{ in} \quad A \approx 7 \text{ in}^2 \quad \lambda \approx 1.3$$

which are not unreasonable values for the SSME.

1. Given the geometrically complex flow in these channels, we can expect the value of K to be larger than unity, probably in the range $5 < K < 15$.

3.2.23 Oxidizer Preburner Pressure (P_{OP})

Centering our attention to the oxidizer preburner in **Figure 1**, we note that there are two flow inputs; LOX and fuel from their respective lines are ignited and gasified and then diverted out of the preburner through the HPOTP turbine. We can use a type 3 equation to find the preburner pressure:

$$\kappa \rho V \frac{d}{dt} P_{OP} = \dot{m}_{opf} + \dot{m}_{opo} + \dot{m}_{asiop} - \dot{m}_{ot2} \quad (142)$$

where

P_{OP} is the oxidizer preburner pressure (psia)

\dot{m}_{opf} is the fuel mass flow rate injected into the oxidizer preburner (lbm/sec)

\dot{m}_{opo} is the oxidizer mass flow rate injected into the oxidizer preburner (lbm/sec)

\dot{m}_{ot2} is the HPOTP turbine flow rate (lbm/sec)

\dot{m}_{asiop} is the oxidizer preburner ASI flow rate (lbm/sec)

V is the oxidizer preburner flow volume (in³)

κ and ρ are the gas compressibility and density (in²/lbf, lbm/in³)

\dot{m}_{opf} , \dot{m}_{opo} , \dot{m}_{asiop} and \dot{m}_{ot2} are defined in sections 3.2.12, 3.2.8, 3.2.20 and by equation (73) respectively. Because at this point the fluid is a gas, compressibility becomes a strong function of pressure, on the other hand we can use the ideal gas equation to write the product

$$\kappa \rho = \frac{1}{JR_g T_{OP}}$$

Since the preburners' mixture ratio is maintained more or less constant, we can expect that both the gas constant and temperature will not experience large variations at different operational points. It is possible that due to this reasons, the value in [3] was taken simply as a constant which is $\kappa \rho V = 0.0001$. Using this and taking the oxidizer preburner mean values for the gas constant and temperature to be $R_g = 0.6 \text{ Btu lbm}^{-1}\text{R}^{-1}$ and $T_{OP} =$

1400°R respectively, we can estimate a volume of about $V = 800\text{in}^3$, which is reasonable for the size of the preburner cavity. There is another slight difference in [3]; the last term of (142) is modified by a constant factor while the ASI flow rate is eliminated. The equation in [3] is the following

$$0.0001 \frac{d}{dt} P_{op} = \dot{m}_{opf} + \dot{m}_{opo} - 0.9980 \dot{m}_{ot2}$$

The reason for this could be that ASI flows are little enough to be taken as small (constant) perturbations into the dynamic model. The advantage of doing so is just a simplification of the mathematical procedures when solving the coupled system of differential equations; however we have to keep track of the origin of such simplifications. As we can see, the simplified version in [3] shows an additional input in the oxidizer preburner subsystem which is reflected in a slight decrease of the output flow rate.

3.2.24 Fuel Preburner Pressure (P_{FP})

The fuel preburner pressure equation is very similar to the oxidizer preburner pressure equation described in 3.2.23. We have two inputs and one output that can be inserted in a type 3 equation, which is modified by allowing variations of the gas compressibility with pressure as was described in section 3.2.23:

$$\left(\frac{V}{JR_g T_{FP}} \right) \frac{d}{dt} P_{FP} = \dot{m}_{fpf} + \dot{m}_{fpo} + \dot{m}_{asifp} - \dot{m}_{ft2} \quad (143)$$

where

P_{FP} is the fuel preburner pressure (psia)

\dot{m}_{fpf} is the fuel mass flow rate injected into the fuel preburner (lbm/sec)

\dot{m}_{fpo} is the oxidizer mass flow rate injected into the fuel preburner (lbm/sec)

\dot{m}_{ft2} is the HPFTP turbine flow rate (lbm/sec)

\dot{m}_{asifp} is the fuel preburner ASI flow rate (lbm/sec)

V is the fuel preburner flow volume (in³)

R_g and T_{FP} are the gas constant and temperature (Btu lbm⁻¹ °R⁻¹, °R)

\dot{m}_{fpf} , \dot{m}_{fpo} , \dot{m}_{asifp} and \dot{m}_{ft2} are defined in sections 3.2.11, 3.2.7, 3.2.19 and equation (53) respectively. The coefficient in (143) is given in [3] as a constant with value

$\frac{V}{JR_g T_{FP}} = 6.25 \times 10^{-5}$. A lower value than the coefficient of (142) was expected since the fuel preburner temperature is slightly higher than the oxidizer preburner's. As in 3.2.23, there is a correction factor given in [3] to account for ASI flows into the preburner; this factor appears also in the last term of (143) which now reads

$$6.25 \times 10^{-5} \frac{d}{dt} P_{FP} = \dot{m}_{fpf} + \dot{m}_{fpo} - 0.997 \dot{m}_{ft2}$$

Again, this simplification lumps together the effect of an extra input term, the ASI flow rate, which is eliminated in [3].

3.2.25 Coolant Liner Pressure (P_{cl})

The coolant liner was described in sections 3.2.9 and 3.2.10. Using the results in that section we can apply a type 3 equation noting that for the liner there is only one input and one output:

$$\left(\frac{V}{JR_g T_{cl}} \right) \frac{d}{dt} P_{cl} = \dot{m}_{cli} - \dot{m}_{clo} \quad (144)$$

where

P_{cl} is the coolant liner pressure (psia)

\dot{m}_{cli} is the coolant liner inlet flow rate (lbm/sec)

\dot{m}_{clo} is the coolant liner outlet flow rate (lbm/sec)

V is the coolant liner flow volume (in³)

R_g and T_{cl} are the gas constant and temperature (Btu lbm $^{-1}$ °R $^{-1}$, °R)

\dot{m}_{cli} and \dot{m}_{clo} are defined in sections 3.2.9, 3.2.10 respectively. The constant coefficient in

$$(144) \text{ is given in [3] by } \frac{V}{JR_g T_{cl}} = 3.525 \times 10^{-6}.$$

3.2.26 Preburners Fuel Supply Line Pressure (P_9)

With help of **Figure 1** we observe that in the preburners' fuel supply line there are two outputs and two inputs. The inputs come from CCV valve and the nozzle heat exchanger, while the outputs go into the fuel and oxidizer preburners. A type 3 equation is used:

$$\left(\frac{V}{JR_g T_9} \right) \frac{d}{dt} P_9 = \dot{m}_4 + \dot{m}_{fnbp} - \dot{m}_{fpf} - \dot{m}_{opf} \quad (145)$$

where

P_9 is the preburners fuel supply line pressure (psia)

\dot{m}_4 is the fuel mass flow rate at the exit of the nozzle heat exchanger (lbm/sec)

\dot{m}_{fnbp} is the fuel mass flow rate through the nozzle heat exchanger bypass (lbm/sec)

\dot{m}_{fpf} is the fuel mass flow rate injected into the fuel preburner (lbm/sec)

\dot{m}_{opf} is the fuel mass flow rate injected into the oxidizer preburner (lbm/sec)

V is the preburners fuel supply line volume (in 3)

R_g and T_9 are the gas constant and temperature (Btu lbm $^{-1}$ °R $^{-1}$, °R)

\dot{m}_4 , \dot{m}_{fnbp} , \dot{m}_{fpf} and \dot{m}_{opf} are defined in sections 3.2.15, 3.2.16, 3.2.11 and 3.2.12

respectively. The constant coefficient is given in [3] by $\frac{V}{JR_g T_9} = 0.0001$

3.2.27 LPOTP Pump Inlet Pressure (P_{os})

As is explained in section 3.2.4, the LPOTP hydraulic turbine flow is discharged directly into the LPOTP pump outlet. Therefore, there are two flow inputs in the LPOTP and one output; a type 3 equation can be used:

$$\kappa_{ox} \rho_{ox} V \frac{d}{dt} P_{os} = \dot{m}_{os} + \dot{m}_{ot1} - \dot{m}_{op2} \quad (146)$$

where

P_{os} is the LPOTP pump inlet pressure (psia)

\dot{m}_{os} is the LPOTP pump inlet oxidizer flow rate (lbm/sec)

\dot{m}_{ot1} is the LPOTP hydraulic turbine flow rate (lbm/sec)

\dot{m}_{op2} is the HPOTP main pump flow rate (lbm/sec)

V is the LPOTP supply line volume (in³)

κ_{ox} and ρ_{ox} are the LOX compressibility and density (in²/lbf, lbm/in³)

\dot{m}_{os} , \dot{m}_{ot1} and \dot{m}_{op2} are defined in sections 3.2.17, 3.2.18 and in equation (74) respectively. In [3], substitution of (74) into (146) was explicitly made and their version of the pump inlet pressure equation reads (including constant coefficient)

$$0.0067 \frac{d}{dt} P_{os} = \dot{m}_{os} - \dot{m}_{mov} - \dot{m}_{op3}$$

Making a similar analysis as that of the end of section 3.2.22 and using the constant coefficients of section 3.2.17, we can make an estimation of the oxidizer supply line geometric and friction characteristics: $L \approx 903\text{ in}$ $D \approx 8\text{ in}$ $\lambda \approx 2.3$

Actual dimensions of the LOX supply line are about 1000in for length and 10in for diameter.

3.2.28 Fuel Injector Pressure (P_{FI})

The fuel injector pressure calculation involves a somewhat large number of flows because in one way or another, most of the fluids in the SSME systems converge at some point into the structure of the HGM. From **Figure 1** we observe that the inputs are the LPFTP, HPFTP and HPOTP turbines discharge gases along with the outlet of the coolant liner. The outputs are the fuel injector flow rate and the fraction taken from the LPFTP turbine discharge to pressurize the LH tank. A type 3 equation can be used here once more:

$$\left(\frac{V}{JR_g T_{FI}}\right) \frac{d}{dt} P_{FI} = \dot{m}_{ft1} + \dot{m}_{ot2} + \dot{m}_{ft2} + \dot{m}_{clo} - \dot{m}_{FI} - \dot{m}_{ftk} \quad (147)$$

where

P_{FI} is the fuel injector pressure (psia)

\dot{m}_{ft1} is the LPFTP turbine discharge flow rate (lbm/sec)

\dot{m}_{ot2} is the HPOTP turbine discharge flow rate (lbm/sec)

\dot{m}_{ft2} is the HPFTP turbine discharge flow rate (lbm/sec)

\dot{m}_{clo} is the coolant liner outlet flow rate (lbm/sec)

\dot{m}_{FI} is the fuel injector flow rate (lbm/sec)

\dot{m}_{ftk} is the fuel tank pressurization flow rate (lbm/sec)

V is the HGM flow volume (in³)

R_g and T_{FI} are the gas constant and temperature (Btu lbm-°R⁻¹, °R)

\dot{m}_{ft1} , \dot{m}_{ot2} and \dot{m}_{ft2} are calculated with equations (94), (73) and (50) respectively. \dot{m}_{FI} is defined in section 3.2.2. \dot{m}_{ftk} is not modeled here and a new type 2 equation would be needed to introduce it. However, its contribution to the dynamics, along with the contribution of \dot{m}_{clo} is expected to be small enough to lump their effects into a constant factor in the same way as it was done in sections 3.2.23 and 3.2.24. In [3], this assumption turned equation (147) into

$$3.33 \times 10^{-4} \frac{d}{dt} P_{FI} = \dot{m}_{fi1} + \dot{m}_{ot2} + \dot{m}_{fi2} - 1.085 \dot{m}_{FI}$$

This modification indicates us that the fraction taken to pressurize the LH tank is in fact larger than the coolant liner outflow.

3.2.29 Main Combustor Chamber Pressure (P_c)

After passing through the MCC injector, the propellants are mixed and burned in the MCC. As we see from **Figure 1**, the inputs are the fuel injector fuel flow and the MOV valve LOX flow, while the output is the nozzle flow which generates thrust. A type 3 equation can be used to calculate the chamber pressure:

$$\left(\frac{V}{JR_g T_c} \right) \frac{d}{dt} P_c = \dot{m}_{FI} + \dot{m}_{mov} - \dot{m}_{cn} \quad (148)$$

where

P_c is the main combustion chamber pressure (psia)

\dot{m}_{FI} is the fuel injector flow rate (lbm/sec)

\dot{m}_{mov} is the oxidizer mass flow rate through the MOV valve (lbm/sec)

\dot{m}_{cn} is the thrust chamber nozzle flow rate (lbm/sec)

V is the thrust chamber nozzle flow volume (in³)

R_g and T_c are the gas constant and temperature (Btu lbm⁻¹ °R⁻¹, °R)

\dot{m}_{FI} and \dot{m}_{mov} are described in sections 3.2.38 and 3.2.6 respectively.

The purpose of a rocket engine is thrust (F) generation, therefore we can say that the most important flow (from this point of view) is the chamber nozzle flow \dot{m}_{cn} which can be ultimately related to the thrust using the following expression derived from classical mechanics considerations

$$F = \frac{\dot{m}_{cn}c}{g} + A_e(P_e - P_a) \quad (149)$$

where c is the nozzle gas exit velocity (in/sec) which depends and is limited by the thermodynamic expansion of the hot gases in the nozzle. A_e is the nozzle exit area, while P_e and P_a are the nozzle exit gas pressure and the ambient pressure respectively. The second term in the rhs of (149) is often referred as the *pressure thrust* and is considerably smaller in magnitude than the first term. It can be shown that maximum thrust can be obtained when the nozzle is *matched*, i.e. when the nozzle exit pressure is the same as the ambient pressure. Qualitatively we can test this by noting that when $P_a > P_e$ the second term changes sign reducing directly the thrust generation, this nozzle *underexpansion* causes a physical suction that is naturally avoided by separation of the nozzle flow when the gas exit pressure is kept above a limiting value. In the opposite case when $P_a < P_e$, the second term actually contributes with positive thrust, however this higher exit pressure indicates that the expansion process was not fully exploited, in other words, the gas exit velocity c is not as large as it would have been with a complete expansion. The net effect is a decrease in magnitude of the first rhs term in (149) which acts as drawback to the increase in pressure thrust. Most rocket engines (including the SSME) work at variable ambient pressures while in their climb phase, therefore, all suffer from thrust reduction because the nozzle geometry remains fixed, fixing the gas exit pressure as well. A solution for this problem is the use of an *external expansion* nozzle that adjusts its exit pressure with the ambient properties in such a way that it remains matched along its flight path. Such a nozzle is considerably less massive and complex than a conventional bell-shaped nozzle, and it is about to be used in the next generation of reusable launch vehicles.

Internal expansion nozzles (like the one in the SSME) are of the convergent-divergent type. **Figure 36** shows this basic shape. Hot gases are generated in the pressurized MCC and move at negligible Mach number ($M \sim 0$) into the convergent part of the nozzle where the gas is accelerated until the flow becomes choked ($M = 1$) at the nozzle throat and then it is expanded supersonically in the divergent part of the nozzle ($M > 1$).¹

1. Nozzle flow is a subject much more complex than this brief explanation. The reader is encouraged to review a good reference such as [10, 11] for a complete description of the phenomena involving compressible fluid flow.

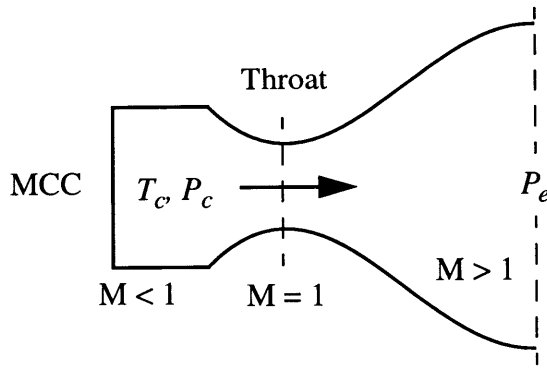


FIGURE 36. Internal Expansion Nozzle

Since we know that in the throat the flow is sonic, we can calculate the mass flow rate at that point, which is the same as the mass flow rate at any other point in the nozzle. From the continuity equation $\dot{m}_{cn} = \dot{m}_t = \rho_t a_t A_t$, where the subscript t indicates conditions at the throat; and as $M = 1$ in the throat the flow velocity is the same as the sound velocity, therefore $a_t = \sqrt{\gamma R_g T_t}$. If we consider the flow to be isentropic inside the nozzle, then some manipulation of these expressions, along with the ideal gas equation, the total or stagnation definitions and the isentropic relations described all in section 3.2.1 yield an expression for the nozzle flow

$$\dot{m}_{cn} = P_c A_t \sqrt{\frac{g\gamma}{JR_g T_c}} \left(\frac{2}{\gamma + 1} \right)^{\frac{\gamma + 1}{2(\gamma - 1)}} \quad (150)$$

From ref. [1] we extracted a value of $A_t = 83.41 \text{ in}^2$ for the throat flow area. The rest of the variables in (150), except P_c , depend on the composition of the gas, which can be described after introducing the oxidizer to total flow ratio r^* in the same way as it is done in section 3.2.1

$$r^* = \frac{\dot{m}_{ox}}{\dot{m}_f + \dot{m}_{ox}} = \frac{\dot{m}_{mov} + \dot{m}_{op3}}{\dot{m}_{mov} + \dot{m}_{FI}}$$

where the last term in this expression can be obtained by keeping track of the oxidizer and fuel flows in **Figure 1**. \dot{m}_{op3} is described in section 3.2.5.

As the typical mixture of propellants in the MCC is close to stoichiometry, the frozen composition analysis performed in 3.2.1 can not be used here. An equilibrium calculation is needed instead and it was done using the NASA CEA code (ref. [12]). The results of such calculation are shown in **Figures 37a**, **37b** and **37c** which represent the equilibrium temperature (T_c), ratio of specific heats (γ) and gas constant (R_g) respectively as functions of the oxidizer to total flow ratio r^* . In particular, the dashed line of **Figure 37a** represents the chamber temperature as established in [3].

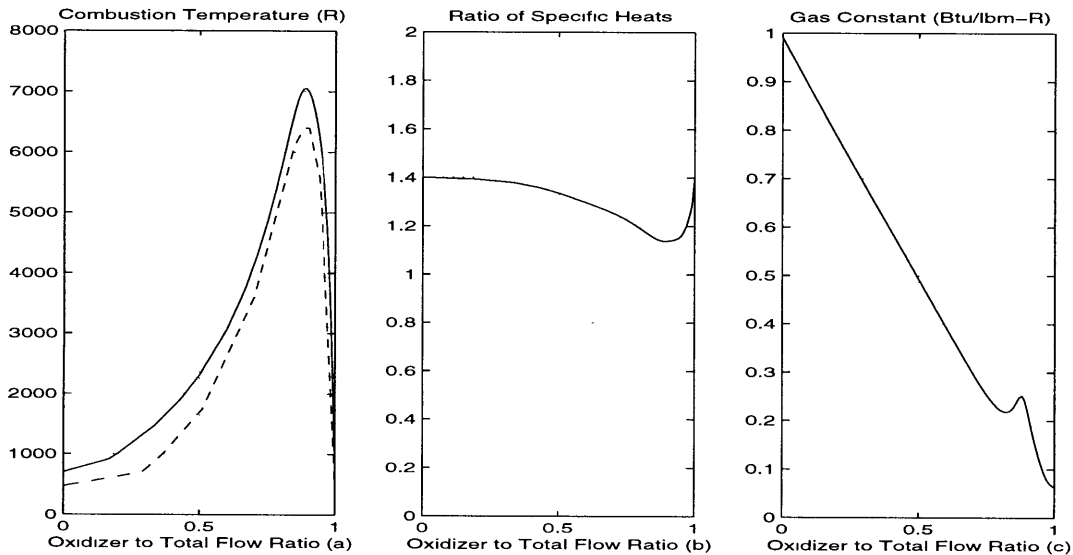


FIGURE 37. NASA CEA Equilibrium Calculation of MCC Gas Properties

After using these results we are now in position to write equation (150) as

$$\dot{m}_{cn} = P_c C^*(r^*) \quad (151)$$

The function C^* , which we may call the *equilibrium flow rate factor* is shown in **Figure 38** as a function of r^* . The dashed line in **Figure 38** is the approximation in [3] to C^* . The approach used to find such a smooth curve is unknown. The only information available is the function itself which is a polynomial function of the oxidizer to total flow ratio:

$$C^*(r^*) = \frac{29122}{35000 + 210500r^* - 173500r^{*2}}$$

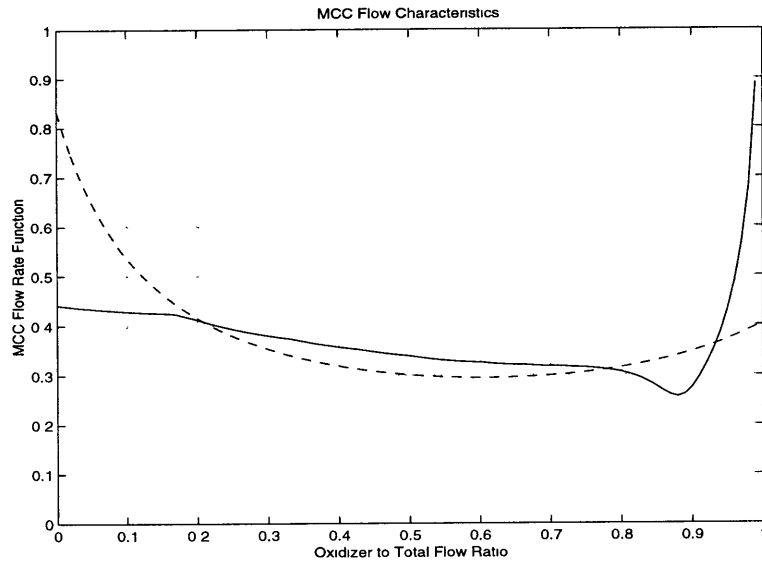


FIGURE 38. Equilibrium Flow Rate Factor

Finally, the constant coefficient of equation (148) is given in [3] by $\frac{V}{JR_g T_c} = 0.00025$

3.2.30 Fuel Density at the Main Combustion Chamber Heat Exchanger (ρ_5)

Hydrogen density is subject to change while it flows from one part to another of the engine. In particular, large amounts of heat can be taken by the fuel in its way through the cooling passages of the nozzle and MCC heat exchangers. In these engine sections, the capacitive dynamics are more likely to be affected by density variations than by pressure variations. With this in mind we can use a type 4 equation to find the density at the MCC cooling circuit in terms of the input which is the flow from the CCV valve and the output that is used to drive the LPFTP as is explained in section 3.2.3:

$$V \frac{d}{dt} \rho_5 = \dot{m}_{mc} - \dot{m}_{ft1} \quad (152)$$

where

ρ_5 is the fuel density at the MCC heat exchanger (lbm/in^3)

\dot{m}_{mc} is the fuel mass flow rate injected into the MCC heat exchanger (lbm/sec)

\dot{m}_{ft1} is the LPFTP turbine flow rate (lbm/sec)

V is the MCC cooling circuit flow volume (in^3)

\dot{m}_{mc} and \dot{m}_{ft1} are described in section 3.2.13 and equation (94) respectively. A rough estimation from an engineering drawing of the MCC found in ref. [1] was made to determine the volume of the MCC cooling circuit. We estimated it to be around 935 in^3 . In [3], the volume is given as 1000 in^3 .

3.2.31 Fuel Density at the Nozzle Heat Exchanger (ρ_4)

Derivation of this equation is the same as that in section 3.2.30. A type 4 equation can be used; the input is the net fuel flow through the nozzle cooling passages while the output is the outflow from the heat exchanger:

$$V \frac{d}{dt} \rho_4 = \dot{m}_{fn} - \dot{m}_4 \quad (153)$$

where

ρ_4 is the fuel density at the nozzle heat exchanger (lbm/in^3)

\dot{m}_{fn} is the fuel mass flow rate injected into the nozzle heat exchanger (lbm/sec)

\dot{m}_4 is the fuel mass flow rate at the exit of the nozzle heat exchanger (lbm/sec)

V is the nozzle cooling circuit flow volume (in^3)

\dot{m}_{fn} and \dot{m}_4 are described in sections 3.2.14 and 3.2.15 respectively. The nozzle cooling circuit flow volume is given in [3] as 2000 in^3 .

3.2.32 Fuel Specific Internal Energy at the MCC Heat Exchanger (SU_5)

As has been already described, some of the fuel flow is diverted out of the MFV into a cooling jacket that encloses the MCC. Definitively one of the most critical parts of a rocket engine is the cooling subsystem. This becomes more evident when we notice that the operational hot gas temperature inside the thrust chamber is in general higher than the melting point of the materials used to build it. Convection and radiation or a combination of both, are commonly used to cool a rocket engine, in particular the radiative method can be used only if the operation conditions are not extreme enough to cause damage to the chamber and nozzle. For example the OMS propulsion subsystem of the Space Shuttle is used to achieve a stable circular orbit after the main engines are shut down; these engines do not operate at extreme conditions like the SSME as their thrust requirements are much lower; their gas temperature is low enough to allow them to cool down using radiative heat transfer only. On the other hand the SSME hot gases reach 6400°R , higher than the melting point of Iron, radiation is by no means enough to maintain the structures in a safe range of temperatures. Convection needs to be used instead. Minimizing weight in a space launch vehicle is of the highest importance, this limits the capability of including a coolant fluid inside it. A very smart way used by the rocket scientists since the very beginning of the “rocket age” was to use the propellants themselves as cooling fluids. This technique is known as *regenerative cooling* since the heat flow into the propellants is not wasted at all, on the contrary it increases its internal energy content which is then applied along with the chemical reaction inside the combustion chamber to produce thrust. Estimating and implementing the heat transfer needs of a particular engine is not a trivial work; considerable empirical and analytical efforts have to be made to reach a final design. In the SSME, hydrogen is used as the coolant fluid; this has some advantages and disadvantages. On the plus side, the heat transfer properties of hydrogen make it an excellent coolant, on the minus there is always an extra care involved in the design to avoid dangerous leaks which can lead to catastrophic situations; this extra care translates into more design and implementation costs. A type 5 equation can be used to estimate the specific internal energy of the hydrogen as it flows through the MCC cooling jacket:

$$\rho_5 V \frac{d}{dt} SU_5 = \dot{Q}_{15} - \dot{Q}_{25} + \dot{m}_{mc} h_{mc} - \dot{m}_{ft1} h_5 \quad (154)$$

where

- SU_5 is the fuel specific internal energy at the MCC heat exchanger (Btu/lbm)
- \dot{Q}_{15} is the heat flow rate from the hot wall to the coolant at the MCC (Btu/sec)
- \dot{Q}_{25} is the heat flow rate from the coolant to the cold wall at the MCC (Btu/sec)
- h_{mc} is the specific enthalpy at the MCC coolant circuit inlet (Btu/lbm)
- h_5 is the specific enthalpy at the MCC coolant circuit outlet (Btu/lbm)
- \dot{m}_{mc} is the fuel mass flow rate injected into the MCC heat exchanger (lbm/sec)
- \dot{m}_{ft1} is the fuel mass flow rate injected into the LPFTP turbine (lbm/sec)
- ρ_5 is the fuel density at the MCC heat exchanger (lbm/in³)
- V is the MCC cooling circuit flow volume (in³)

\dot{m}_{mc} , ρ_5 and \dot{m}_{ft1} are described in sections 3.2.13, 3.2.32 and equation (94) respectively.

The MCC cooling circuit flow volume is once more given in [3] by 1000 in³.

Writing down the enthalpy definition we immediately observe that

$$h_5 = SU_5 + \frac{P_5}{J\rho_5}$$

P_5 can be obtained from tables as described in section 3.2.3. If we now assume that the internal energy of the fuel remains constant while it flows through the LPFTP and the HPFTP pump sections, then we can estimate the enthalpy at the inlet of the cooling circuit as a function of the pressure rise/drop in the pumps/lines (ΔP_{mcc}) and the hydrogen enthalpy inside the fuel tank (h_{tk}). Once again, from the enthalpy definition

$$h_{mc} = h_{tk} + \frac{\Delta P_{mcc}}{J\bar{\rho}}$$

where $\bar{\rho}$ can be taken as an average hydrogen density as it flows as a liquid through the centrifugal compressors and blades of the HPFTP and LPFTP pumps. Although we can

expect significant variations of the hydrogen (two-phase) gas pressure with operation power levels, they are, in principle, almost cancelled out by the corresponding increase in fluid density, the net effect is a minimum variability of the rhs term in the last expression.¹

In very general terms, convection heat transfer between the hot wall (or the wall which is in contact with the combustion gases) and the coolant fluid can be described as a function proportional to the temperature difference between them (see **Figure 3**)

$$\dot{Q}_{15} = Ah_g(T_{w15} - T_5) \quad (155)$$

where A is the hot wall effective cooled area, T_5 can be estimated from tables as described in section 3.2.3 and T_{w15} is the hot wall temperature which is described in section 3.2.34. As we can see, (155) itself is a very simple linear expression, however a considerable amount of complexity is hidden in the *film coefficient* h_g (Btu/hr- °R-ft²). Several authors² have tried to give accurate descriptions for this coefficient using dimensional analysis and a very large collection of experimental data. This coefficient depends on the coolant fluid properties which determine its heat capabilities and on the amount of coolant used. This has lead to expressions which look more or less like the following

$$\frac{h_g D}{k} = 0.026 \left(\frac{D\dot{m}_{mc}}{A\mu} \right)^{0.8} \left(\frac{\mu c_p}{k} \right)^{0.4} \quad (156)$$

where A and D are the chamber area and diameter (in ft² and ft), respectively and μ (lbm/hr-ft), k (Btu/ft-hr- °R) and c_p (Btu/lbm- °R) are the gas (the coolant, in this case) absolute viscosity, conductivity and specific heat respectively.³ Minor variations and corrections for rocket engine applications can be found in the literature [10]. It needs to be emphasized, however, that (156) is still an empirical relation used for simple purposes, therefore the most accurate description of heat transfer for a specific application always comes when testing and analyzing the data of actual engine burns.

1. One step further is taken in [3] where the enthalpy is given simply as a constant, $h_{mc} = 189.7$ Btu/lbm

2. See reference [14], for instance.

3. In this units, the mass flow rate should be given in lbm/hr. It is important to verify that all units are consistent before using this kind of expressions.

In [3], the product Ah_g has been manipulated into a function of the coolant temperature and mass flow rate only¹ (a dependence on $A^{0.2}$ would also be indicated by (156), but this has been averaged out).

$$Ah_g = 1.9104(1 + 0.002T_5)\dot{m}_{mc}^{0.8}$$

In exactly the same way there is also heat that flows from the coolant fluid to the cold wall (the wall in contact with the ambient in which the rocket operates). In [3], this heat flow is described as

$$\dot{Q}_{25} = 3.821(1 + 0.002T_5)(T_5 - Tw_{25})\dot{m}_{mc}^{0.8} \quad (157)$$

where Tw_{25} is the cold wall temperature as given in section 3.2.35.

3.2.33 Fuel Specific Internal Energy at the Nozzle Heat Exchanger (SU_4)

Even though most of the heat transfer rate is localized at the throat section of the MCC², there is also a very strict requirement for heat transfer in the nozzle walls. The difference with respect to the MCC coolant circuit is that the wall area becomes very large and structural rigidity precludes the use of a hollow jacket. Instead there are 1,080 individual stainless steel tubes brazed together, encircled by a structural support. The CCV valve controls the amount of fuel which is allowed to flow through these tubes and therefore it works also as an additional control of the preburners' energy input. The heat transfer can be described with a type 5 equation:

$$\rho_4 V \frac{d}{dt} SU_4 = \dot{Q}_{14} - \dot{Q}_{24} + \dot{m}_{fn} h_{fn} - \dot{m}_4 h_4 \quad (158)$$

where

-
1. This is to be expected since the coolant properties vary with temperature. It was found in [3] that the complex film coefficient reduced to a linear expression for the range of temperatures experienced by the coolant on its way through the heat exchangers.
 2. Heat flow rate is highest at the throat because the wall area reaches its minimum at that particular section.

- SU_4 is the fuel specific internal energy at the nozzle heat exchanger (Btu/lbm)
 \dot{Q}_{14} is the heat flow rate from the hot wall to the coolant at the nozzle (Btu/sec)
 \dot{Q}_{24} is the heat flow rate from the coolant to the cold wall at the nozzle (Btu/sec)
 h_{fn} is the specific enthalpy at the nozzle coolant circuit inlet (Btu/lbm)
 h_4 is the specific enthalpy at the nozzle coolant circuit outlet (Btu/lbm)
 \dot{m}_{fn} is the fuel mass flow rate injected into the nozzle heat exchanger (lbm/sec)
 \dot{m}_4 is the fuel mass flow rate out of the nozzle heat exchanger (lbm/sec)
 ρ_4 is the fuel density at the nozzle heat exchanger (lbm/in³)
 V is the nozzle cooling circuit flow volume (in³)

\dot{m}_{fn} , ρ_4 and \dot{m}_4 are described in sections 3.2.14, 3.2.31 and 3.2.15 respectively. As before, the nozzle coolant flow volume is given in [3] by $V = 2000\text{in}^3$.

The fuel flow used to regeneratively cool the nozzle section of the SSME follows a different path from the flow that cools the MCC after both pass through the MFV valve. That difference modifies the value of the pressure variations ΔP_{nozzle} that is used to estimate the hydrogen enthalpy at the inlet of the cooling circuit¹

$$h_{fn} = h_{tk} + \frac{\Delta P_{nozzle}}{J\bar{\rho}}$$

The enthalpy definition can be used here as well to estimate

$$h_4 = SU_4 + \frac{P_4}{J\rho_4}$$

P_4 is also obtainable from tables as described in section 3.2.14. The heat transfer complexity described in section 3.2.32 is an issue here once more. In [3], the heat flow

1. In [3] these variations are averaged and the constant value of $h_{fn} = 166.8$ is given.

from the nozzle's hot wall to the coolant and the heat flow from the coolant to the nozzle's cold wall are given respectively by

$$\dot{Q}_{14} = 2.092(1 + 0.002T_4)(Tw_{14} - T_4)\dot{m}_{fn}^{0.8} \quad \text{and}$$

$$\dot{Q}_{24} = 4.18(1 + 0.002T_4)(T_4 - Tw_{24})\dot{m}_{fn}^{0.8}$$

where Tw_{14} and Tw_{24} are the hot and cold wall temperatures respectively which can be found in sections 3.2.36 and 3.2.37 respectively.

3.2.34 Main Combustor Chamber Heat Exchanger Hot Wall Temperature (Tw_{15})

As it was explained in sections 3.2.32 and 3.2.33, heat transfer is a critical issue while reviewing the design considerations for a rocket engine. In particular, the coolant fluid takes the excess heat from the hot wall limiting therefore its temperature increase to a predetermined safe value. The heat transferred to the hot wall comes directly from the combustion gases, convection is once more the heat transfer mechanism. A type 6 equation can be used to estimate the hot wall temperature:

$$\frac{d}{dt}Tw_{15} = \frac{1}{mc_v}(\dot{Q}_{tc5} - \dot{Q}_{15}) \quad (159)$$

where

Tw_{15} is the MCC heat exchanger hot wall temperature ($^{\circ}\text{R}$)

\dot{Q}_{tc5} is the heat flow rate from the hot gases to the hot wall at the MCC (Btu/sec)

\dot{Q}_{15} is the heat flow rate from the hot wall to the coolant at the MCC (Btu/sec)

m, c_v are the MCC hot wall effective mass and its specific heat (lbm, Btu/lbm- $^{\circ}\text{R}$)

\dot{Q}_{15} is described by equation (155) and the product $mc_v = 3.23 \text{ Btu}/^{\circ}\text{R}$ was taken from [3]. On the other hand, \dot{Q}_{tc5} can be calculated considering that convection is involved. We can take advantage of the fact that the SSME operates at a fixed mixture ratio and

therefore generates hot gases at the unique temperature to estimate the value of the film coefficient using expression (156) directly. Using the results from the CEA NASA code [12], an equilibrium calculation yields

$$k = 0.97 \frac{\text{Btu}}{\text{ft}\cdot\text{hr}\cdot{}^{\circ}\text{R}} \quad \mu = 0.269 \frac{\text{lbm}}{\text{ft}\cdot\text{hr}} \quad c_p = 1.98 \frac{\text{Btu}}{\text{lbm}\cdot{}^{\circ}\text{R}}$$

and from [1], the chamber diameter is taken as $D = 1\text{ ft}$. We therefore find that¹

$$\dot{Q}_{tc5} = 0.011(T_c - Tw_{15})\dot{m}_{cn}^{0.8}$$

where the nozzle mass flow rate \dot{m}_{cn} comes from equation (150). In [3] a different value is described, and the heat flow rate is then given by

$$\dot{Q}_{tc5} = 0.030(T_c - Tw_{15})\dot{m}_{cn}^{0.8}$$

The non-negligible difference of 0.02 in the coefficient can be once more attributed to empirical adjustments done in [3].

3.2.35 Main Combustor Chamber Heat Exchanger Cold Wall Temperature (Tw_{25})

The cold wall serves as an interface between the coolant flow and the ambient conditions in which the rocket engine operates. Although less critical than its hot counterpart, the cold wall temperature still plays an important role in the determining the coolant properties and in structural considerations. A type 6 equation is used to find such temperature:

$$\frac{d}{dt}Tw_{25} = \frac{1}{mc_v}(\dot{Q}_{25} - \dot{Q}_{cw5}) \quad (160)$$

where

Tw_{25} is the MCC heat exchanger cold wall temperature (${}^{\circ}\text{R}$)

1. After performing some conversions of units.

\dot{Q}_{25} is the heat flow rate from the coolant to the cold wall at the MCC (Btu/sec)

\dot{Q}_{cw5} is the heat flow rate from the cold wall to the ambient at the MCC (Btu/sec)

m, c_v are the MCC cold wall effective mass and its specific heat (lbm, Btu/lbm- °R)

\dot{Q}_{25} is described in section 3.2.32, while the product $mc_v = 12.12 \text{ Btu}/\text{°R}$ was extracted from [3]. Trying to describe the convective heat transfer between the cold wall and the ambient atmosphere can be even more difficult and not very worthy; as the rocket climbs, the atmospheric air becomes less dense quite rapidly and convection soon becomes much less important than radiation, which in turn is also negligible compared with the rest of the heat flows inside the engine. A quite good approximation is to consider that the cold wall is perfectly insulated and therefore the heat transfer \dot{Q}_{cw5} is always zero.

3.2.36 Nozzle Heat Exchanger Hot Wall Temperature (T_{w14})

The nozzle hot wall temperature results also from a heat flow balance which can be expressed as a type 6 equation:

$$\frac{d}{dt}T_{w14} = \frac{1}{mc_v}(\dot{Q}_{tc4} - \dot{Q}_{14}) \quad (161)$$

where

T_{w14} is the nozzle heat exchanger hot wall temperature (°R)

\dot{Q}_{tc4} is the heat flow rate from the hot gases to the hot wall at the nozzle (Btu/sec)

\dot{Q}_{14} is the heat flow rate from the hot wall to the coolant at the nozzle (Btu/sec)

m, c_v are the MCC hot wall effective mass and its specific heat (lbm, Btu/lbm- °R)

\dot{Q}_{14} is described in section 3.2.33 and the product mc_v is equal to 6 Btu/°R as given in [3]. The heat transfer from the hot gases to the nozzle's hot wall can be found in the same way as in section 3.2.34 for the MCC, and is given in [3] by

$$\dot{Q}_{24} = 0.0580(T_c - Tw_{14})\dot{m}_{cn}^{0.8}$$

where T_c is the MCC chamber gas temperature and \dot{m}_{cn} is the chamber-nozzle flow rate, both are described in section 3.2.29.

3.2.37 Nozzle Heat Exchanger Cold Wall Temperature (Tw_{24})

To calculate the temperature of the cold wall in the nozzle heat exchanger we need to apply a type 6 equation:

$$\frac{d}{dt}Tw_{24} = \frac{1}{mc_v}(\dot{Q}_{24} - \dot{Q}_{cw4}) \quad (162)$$

where

Tw_{24} is the nozzle heat exchanger cold wall temperature ($^{\circ}\text{R}$)

\dot{Q}_{24} is the heat flow rate from the coolant to the cold wall at the nozzle (Btu/sec)

\dot{Q}_{cw4} is the heat flow rate from the cold wall to the ambient at the nozzle (Btu/sec)

m, c_v are the nozzle cold wall effective mass and its specific heat (lbm, Btu/lbm- $^{\circ}\text{R}$)

\dot{Q}_{24} is described in section 3.2.33. A value of $mc_v = 12$ Btu/ $^{\circ}\text{R}$ is given in [3].

In the same way as in section 3.2.35 for the MCC, a good simplification is to consider that the cold wall is insulated and no heat is transmitted in any way to the ambient. Therefore, a value of zero can be given to \dot{Q}_{cw4} as well.

3.2.38 Main Fuel Injector Flow Rate (\dot{m}_{FI})

After flowing through the HGM, the fuel rich hot gases generated in the fuel and oxidizer preburners are diverted into the MCC injector. LOX is injected through a series of 600 individual elements, these elements are heated by the hot gases causing the LOX to

evaporate and therefore making the mixing and combustion processes more expeditious, for this reason the MCC of the SSME is shorter than combustion chambers of rockets with different type of injectors. At some point along the element length, it becomes coaxial, allowing the hot fuel rich gases to flow through the annular region until mixing with the evaporated oxygen occurs. We can expect a time lag in the calculation of the fuel injector flow rate due to the relatively small channel radius-to-length ratio in this annular region. To compute the time lag, the last type of dynamic equation, number 7, can be used:

$$\frac{d}{dt}\dot{m}_{FI} = \frac{1}{\epsilon}(\dot{m}_{fi} - \dot{m}_{FI}) \quad (163)$$

where

\dot{m}_{FI} is the main fuel injector flow rate after considering the time lag (lbm/sec)

\dot{m}_{fi} is the main fuel injector flow rate before considering the time lag (lbm/sec)

ϵ is the time lag in the fuel injector (sec)

What equation (163) tells us is basically that the mass flow rate \dot{m}_{fi} , which can be computed given the conditions surrounding the injector, propagates after certain time into the flow rate \dot{m}_{FI} that affects the rest of the model once coupling takes place.

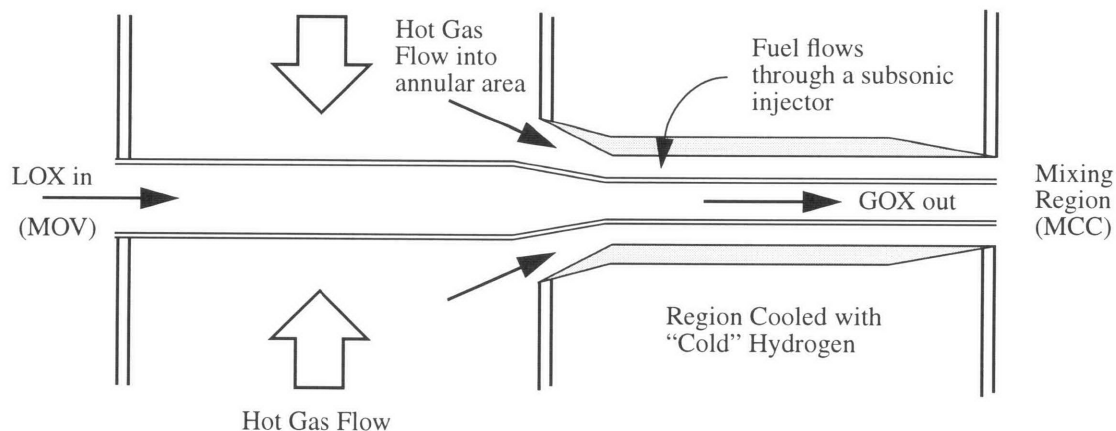


FIGURE 39. Propellant Flow in One Element of the Main Injector

Figure 39 shows a simplified diagram of the flow of propellants in one of the 600 individual elements that constitute the main injector of the SSME. The shape of the fuel injector channel is convergent, therefore the flow can be, at most, sonic.

If the inlet of the fuel injector has a temperature T_{FI} and pressure P_{FI} , and in the exit we have MCC conditions with temperature T_c and pressure P_c , then taking the fuel rich hot gases as ideal we can write the continuity equation in the injector exit as

$$\dot{m}_{fi} = n_e \rho_c u_c A_c = \frac{n_e P_c}{JR_g T_c} u_c A_c \quad (164)$$

where A_c is the annular area of the element's fuel injector exit and n_e is the total number of elements. The gas velocity u_c can be estimated considering an ideal expansion in the convergent passage from inlet to exit conditions

$$u_c = \sqrt{\frac{2gJ\gamma R_g}{\gamma - 1} T_{FI} \left[1 - \left(\frac{P_c}{P_{FI}} \right)^{\frac{\gamma-1}{\gamma}} \right]}$$

After some manipulation of the last two expressions and using isentropic relations, it can be shown that (164) reduces to

$$\dot{m}_{fi} = C_{fi} \frac{P_{FI}}{\sqrt{T_{FI}}} \sqrt{\left(\frac{P_c}{P_{FI}} \right)^{\frac{2}{\gamma}} - \left(\frac{P_c}{P_{FI}} \right)^{\frac{\gamma+1}{\gamma}}} \quad (165)$$

where the coefficient C_{fi} is given by

$$C_{fi} = n_e A_c \sqrt{\frac{2g\gamma}{JR_g(\gamma - 1)}}$$

In [3], the coefficient has a value of $C_{fi} = 19.387$. Using adequate values, we can estimate that each element has an annular area of about $A_c = 0.03 \text{ in}^2$, which is not an unreasonable value. Special attention needs to be focused on the fact that deals with the assumption already made to compute the gas velocity at the injector's exit; the equation itself cannot distinguish between subsonic or supersonic flow, it only depends on the conditions at the

extremes of the channel. However, we know from empirical results that in a convergent passage only the subsonic branch of the solution exists. We therefore need to specify into our model a condition dealing with this situation. Rewriting the velocity equation (isentropic flow) in terms of the Mach number

$$\frac{P_{FI}}{P_c} = \left(1 + \frac{\gamma - 1}{2} M^2\right)^{\frac{\gamma}{\gamma - 1}}$$

In the extreme physical case, the flow becomes choked and it does not matter how small the chamber to fuel injector pressure ratio becomes, the flow will remain sonic. Applying this condition to the last expression we see the following must hold

$$\frac{P_c}{P_{FI}} > \left(\frac{2}{\gamma + 1}\right)^{\frac{\gamma}{\gamma - 1}}$$

If for any reason the pressure ratio drops below this value, then a modified version of equation (165) should be used instead to force the sonic solution

$$\dot{m}_{fi} = C_{fi} \frac{P_{FI}}{\sqrt{T_{FI}}} \sqrt{\left(\frac{2}{\gamma + 1}\right)^{\frac{2}{\gamma - 1}} - \left(\frac{2}{\gamma + 1}\right)^{\frac{\gamma + 1}{\gamma - 1}}} \quad (166)$$

When choked, the mass flow rate remains fixed and becomes independent of the downstream conditions.

Finally, the time delay is given in [3] by $\epsilon = 0.02$ sec.

Chapter 4

SSME Rotordynamic Modeling

Vibrations in liquid propellants rocket engines is a very important issue and a difficult one to characterize given the large number of potential disturbance sources that range from the combustion process, the aerodynamic interaction with the vehicle all the way to the rotational dynamics of the turbopump pressurizing subsystem. As in any oscillatory system, a rocket engine can experience instabilities with unforeseeable consequences. It is therefore desirable to have a well-grounded knowledge regarding the origin of all the different types of vibrational excitations along with the expected response of the engine's components and subcomponents to these excitations. In reality it is exceptionally difficult to categorize all the possibilities because of the extremely high structural complexity involved, however we can expect that some sources and responses are more important than others in occurrence, amplitudes, and potential consequences if instabilities happen to appear.

Experience has demonstrated that one of the most important sources of vibration in a rocket engine comes from the rotordynamic interactions in the turbomachinery, more specifically, from rotor vibrations about its equilibrium position. **Figure 40** shows a schematic of the SSME's HPFTP rotor. Because of their importance, we will consider rotordynamic vibrations exclusively. The general vibration problem in turbomachinery can be divided in two types, the *synchronous* or *forced* vibration and the *sub-synchronous*

or *self-excited* vibration. After a brief explanation of both, we will conclude this chapter with the development of a simplified model which can be used to calculate some of the rotor's critical or natural oscillation frequencies. In the following paragraphs the importance of having an accurate knowledge of such frequencies will become evident.

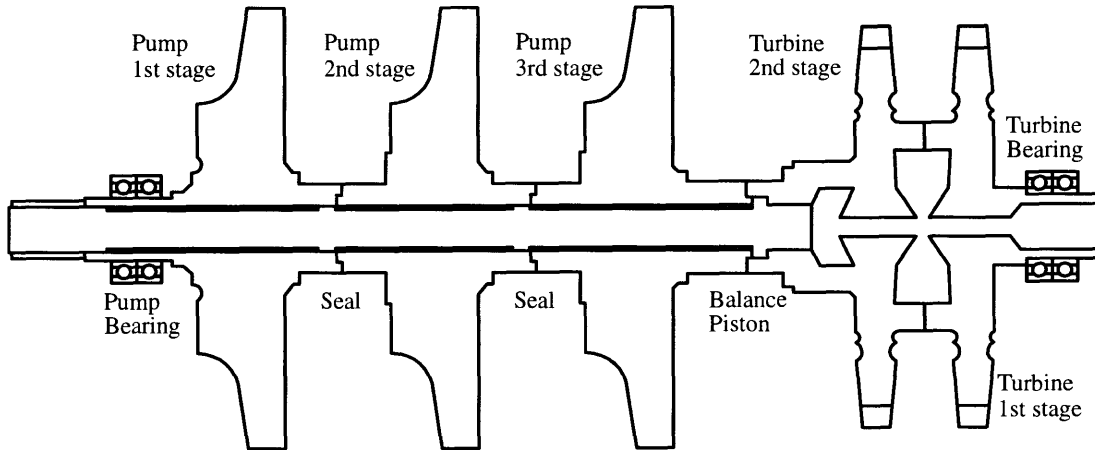


FIGURE 40. Schematic of the HPFTP Rotor - adapted from [4]

4.1 Synchronous or Forced Vibration

At the engine's design stage, we can easily imagine a rotor that will never undergo forced vibrations. It is enough to have a perfect distribution of mass around the shaft axis which needs to be perfectly aligned along the rotation axis. In reality it is just impossible to achieve such an ideal situation; it does not matter how strong are our efforts to maintain axial symmetry in the rotor construction, there will always be an unbalance from the equilibrium shaft axis. **Figure 41a** shows an axial view of a single disc rotor revolving at angular velocity Ω about its shaft axis. The center of mass does not lie in the same position as the shaft's rotational axis.

It is not difficult to conclude that this physical unbalance will cause a vibrational response of the rotor at exactly the same rotational frequency Ω . If for some reason the shaft angular velocity and therefore the vibration frequency coincides with one of the natural frequencies of the rotor, say ω_c , then resonance occurs and the vibration amplitude increases drastically as we can see in **Figure 41b**, this large amplitude can cause serious

damage mostly to static parts of the rotor assembly. As we have already said, this vibration is present in practically all turbomachinery in use and therefore its avoidance is of vital importance. In general there are two things that can be done: (a) to avoid large synchronous amplitudes a precise balance of the rotor assembly is required; and (b) avoiding resonance is easily done by operating the turbomachinery at a safe distance from critical frequencies.

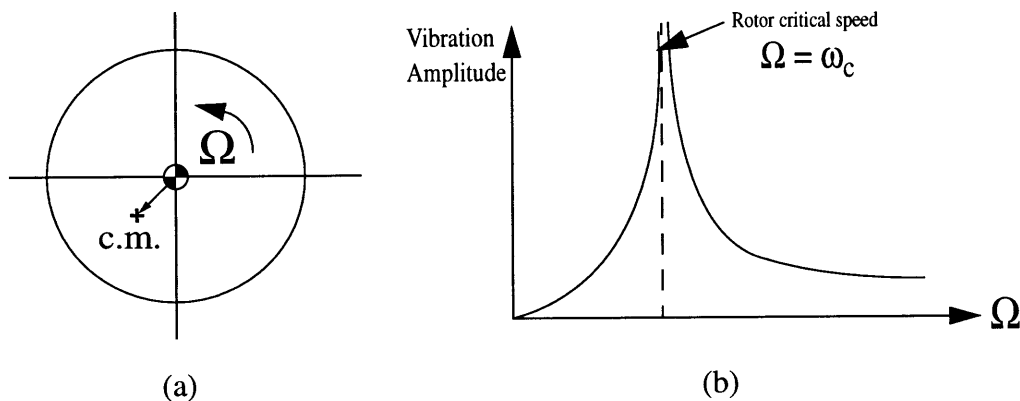


FIGURE 41. Rotor Synchronous Vibration

Rocket engine turbomachinery tend to be safe from synchronous vibration as they in general operate at a high angular velocity as compared with its natural frequencies. It, however, must be considered as a serious threat to the machinery performance and special care must be provided to avoid its presence at all times.

4.2 Sub-synchronous or Self-excited Vibration

Let us assume for the moment that we have a rotor in which the synchronous vibration described in section 4.1 has been completely eliminated; there is zero residual unbalance and we can, in principle, increase the shaft angular velocity to match one of the natural frequencies of the rotor without fear of entering in resonance.¹ As we, however, reach the lowest critical frequencies and keep on increasing the angular velocity, a new oscillation

1. In this particular case, the center of the shaft coincides with the rotor's center of mass.

may arise at some point. The characteristics of such movement are very specific: the rotor's center of mass experiences a revolving motion around the nominal position of the shaft's axis with an angular velocity equal to one of the lowest natural frequencies of the rotor. Commonly referred as *whirling*, this oscillation is sub-synchronous because its frequency lies below the operating angular velocity.¹

As an illustration of the sub-synchronous vibration origin, consider a disc of mass M which has the ability of rotate without friction about its principal axis at a rate Ω , and is restrained to the casing by means of a set of springs as in **Figure 42a**. External damping can be provided as well. If the disc is displaced from its central (equilibrium) position, a cross-force appears which is applied in a direction perpendicular to such displacement as shown in the close-up view of **Figure 42b**. This cross-force acts as a feedback mechanism that ultimately causes the disc center to whirl around its equilibrium position.²

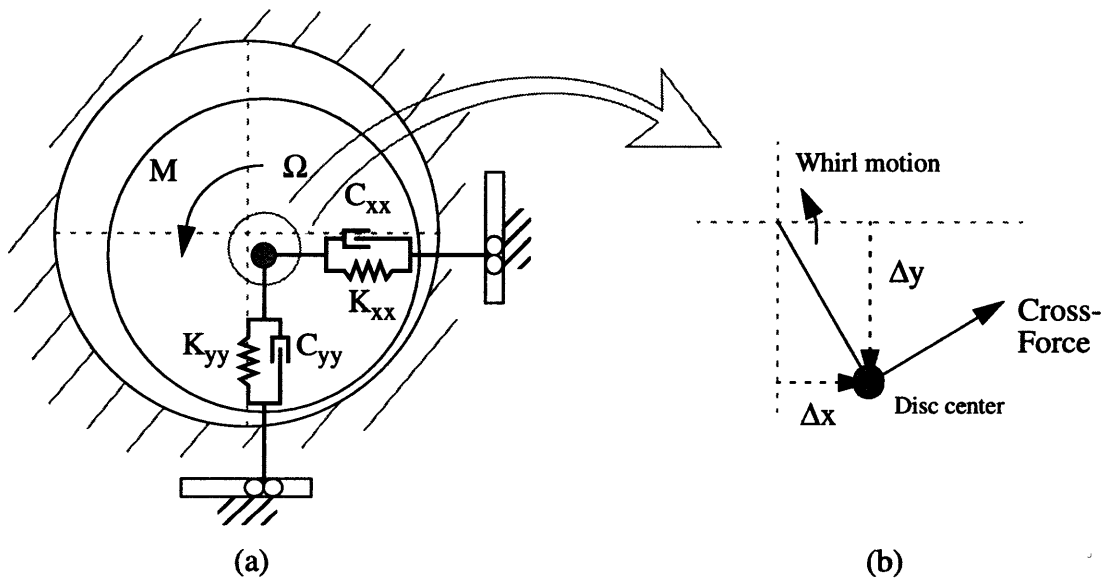


FIGURE 42. Disc Rotating About its Principal Axis (view from the axis)

The feedback mechanism is the reason for calling this vibration self-excited; its appearance is independent from any applied external force. This induced steady cross-

-
1. The fact that the vibration is subsynchronous in rocket engine turbopumps is not surprising as they are designed to operate at high power above the first natural frequency.
 2. Determination of the stability criteria for this particular example can be found in Appendix E.

force is proportional to the shaft's deflection from its rotation centerline, and the proportionality factor is a cross-coupled stiffness coefficient which is in general a function of the rotational velocity. At some particular velocity Ω_p , the induced force will grow to a value that exceeds the stabilizing damping force. The general motion of the shaft axis in the axial plane is a spiral movement with an exponentially increasing amplitude that occurs once the velocity Ω_p has been reached. This increase, however, is not indefinite because several non-linear mechanisms are likely to dissipate more energy as the amplitudes become larger; in general, a steady state value for the amplitude is reached after certain amount of time. Nevertheless, the final amplitudes are large enough to cause serious damage or destruction of the rotor or other parts of the turbomachinery. The appearance of whirling posses a considerable threat in the development of new turbomachinery; for example the HPFTP was unstable from initial design making it impossible to get close to the desired shaft velocity without destroying the equipment. From our current explanation we observe that the impact of whirling can be reduced if: (a) enough external damping is provided, this shifts Ω_p to a higher value, preferable higher than the operating speed, (b) or by increasing the rotor's stiffness or decreasing its mass, the effect of which is to increase its natural frequency, (c) or one could always operate the turbomachinery at lower speeds, this, however, is not desirable for the state-of-the-art components of today which are required to perform at higher and higher velocities, and (d) one could decrease the cross-coupled stiffness coefficient which involves decreasing the impact of the whole cross-force mechanism. The most satisfactory solution would be (d), however it has been very difficult to categorize and understand the origin and effects of the destabilizing forces that cause the appearance of the cross-forces in the first place. Some of them have been identified though, and in general they deal with fluid-mechanical and frictional interactions with the rotor. One of the most frequent and important mechanisms that is likely to be present in high speed axial turbomachinery is the one described by Thomas & Alford¹.

This mechanism arises when there are differential tangential forces acting on a turbine disc due to an uneven efficiency distribution about its perimeter. The origin of such

1. See reference [5].

unequal work extraction comes from small displacements that the shaft can have about its nominal position, this causes the tip of the turbine blades to be closer or farther from the casing at opposite locations at a given time as shown in **Figure 43**. If there is a larger gap between the blade tip and the casing, then leakage through the gap increases, decreasing the efficiency of the turbine in that particular section and increasing it in the opposite section where the blade tip is closer to the casing. Even though the work extraction difference can be quite small, the net effect which induces whirl is not; that is the reason why blade tip clearance is one of the most important sources of rotor instabilities.

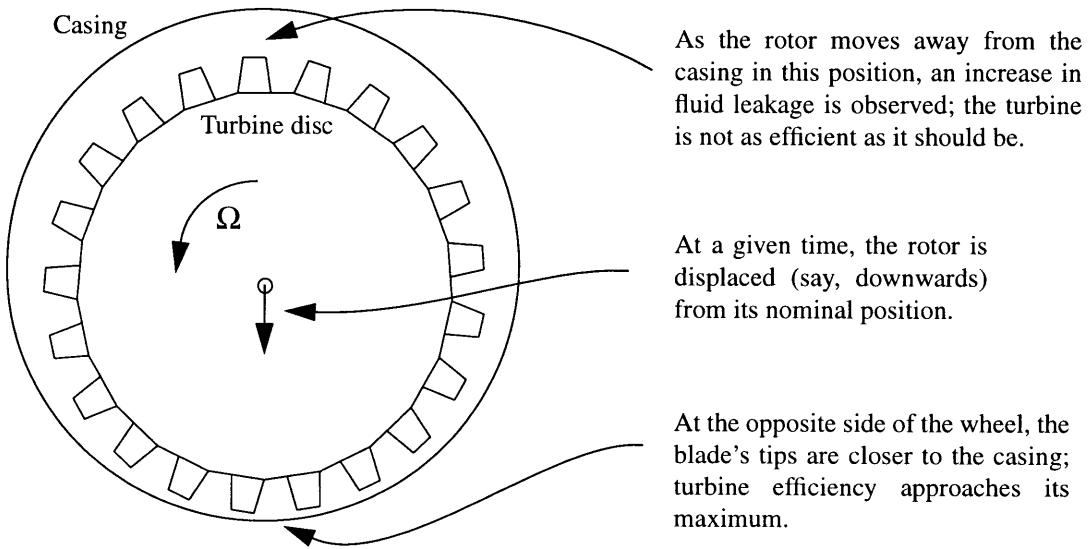


FIGURE 43. Visualization of the Tip-Clearance Destabilizing Mechanism (not in scale)

4.3 Calculation of Critical or Natural Frequencies

Both synchronous and sub-synchronous vibrations can be potentially dangerous for rocket engine turbomachinery and also the appearance of both depend in a strong way on the natural frequencies of the rotor. Because of this, there is a major interest in having a good knowledge of the engine's modal frequencies so vibrational instabilities can be avoided. One way of obtaining such frequencies is from direct experimental measurements of the turbomachinery components and assemblies, this however can be extremely expensive while in the design phase; it is always preferable to estimate the modal frequencies before

actually manufacturing the hardware. There are some elaborate finite element methods used for calculating these frequencies [4, 16, 17]. In the following pages, a simplified dynamic model which allows us to calculate the modal shapes and frequencies for the SSME's HPFTP rotor and casing is developed.

4.3.1 HPFTP Simplified Rotor Model

The rotor of the HPFTP consists of a complex assembly of different parts as shown in **Figure 40**: the three centrifugal pump stages are mounted on a single beam. One extreme of the beam is held by a bearing (pump bearing) which is attached to the rotor casing; the other extreme is fastened to the turbine's second and first stages. A second bearing (turbine bearing) is mounted at the end of the first stage. In our simplified lumped version, the pumps and turbines are considered as solid thin discs mounted over a single symmetric beam with certain density per unit length (ρ_b), geometrical moment of inertia (I), modulus of elasticity (E) and length (L); their position over the shaft (x_i), mass (m_i) and moments of inertia (J_i) are in agreement with the finite element model developed in [4].

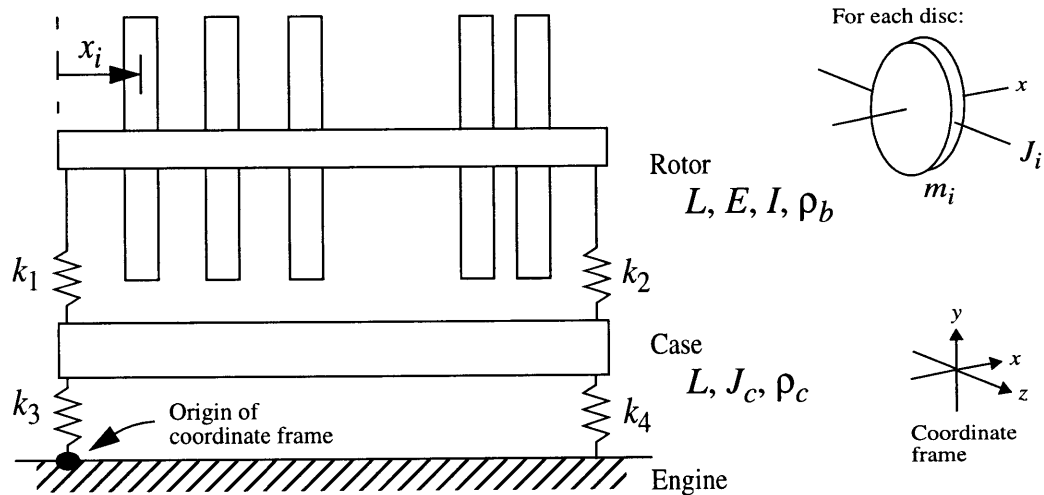


FIGURE 44. Simplified Model for the HPFTP

Figure 44 shows a visualization of the simplified model for the HPFTP. The bearings are substituted by elastic springs (with constants k_1 and k_2) which are attached to a heavy bar

of density per unit length (ρ_c) and moment of inertia (J_c), this bar is considered as a rough representation of the turbopump casing. Finally, the casing itself is attached to the engine via springs (with constants k_3 and k_4), in our case the engine is considered as ground, completely fixed.

In order to determine the dynamic behavior of this simplified model, we have to define the allowed number of degrees of freedom. As is shown in **Figure 45**, only five degrees of freedom will be considered: one for the first bending mode amplitude of the rotor beam (f) plus four for each of the spring displacements (e_1, e_2, e_3 and e_4). The bar representing the casing will be considered rigid enough to preclude it from bending.

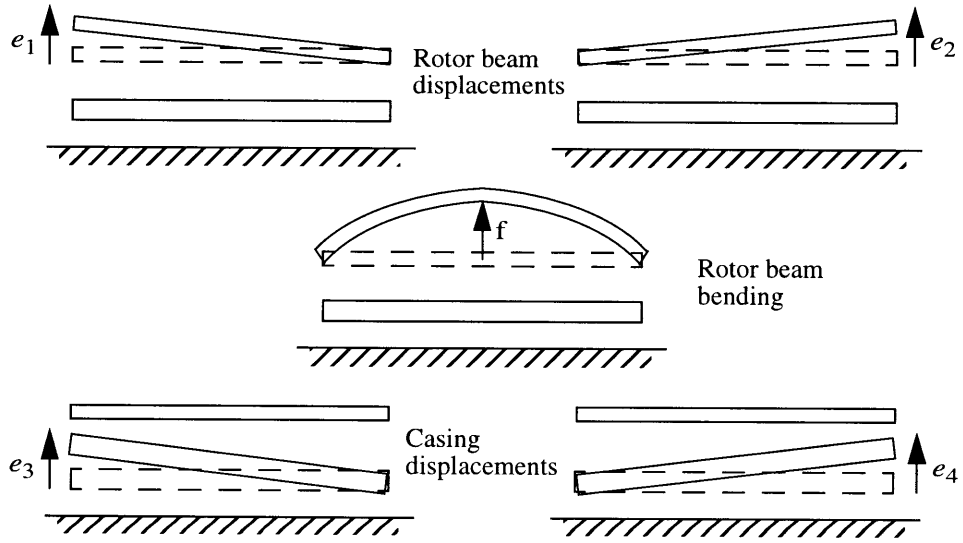


FIGURE 45. Degrees of Freedom for the HPFTP Simplified Rotor Model (discs omitted)

4.3.2 Lagrange Formulation of the Simplified Dynamic Problem

Based on the model information of section 4.3.1, we are in position of constructing a coupled system of five differential equations, one for each degree of freedom. In order to do so, the Lagrange formulation can be used:

$$\frac{d}{dt} \frac{\partial \mathcal{L}}{\partial \dot{q}_i} - \frac{\partial \mathcal{L}}{\partial q_i} = 0 \quad \text{where} \quad q_i \equiv \{f, e_1, e_2, e_3, e_4\} \quad (167)$$

The symbol \mathcal{L} represents the Lagrangian of the system, which is defined as

$$\mathcal{L} = T - V$$

where T and V are the total kinetic and potential energies of the system.

4.3.2.1 Calculation of the Potential Energy in the Simplified Model

Each one of the elastic springs that we are considering in our simplified model contributes with one term in the calculation of the potential energy. If we call V_s the total spring contribution to the potential energy, then we note immediately that

$$V_s = \frac{1}{2}[k_1(e_1 - e_3)^2 + k_2(e_2 - e_4)^2 + k_3e_3^2 + k_4e_4^2] \quad (168)$$

Neglecting gravitational potential, the remaining term depends on the elastic energy stored on the rotor as it bends. From beam theory considerations, this energy V_b is given by

$$V_b = \frac{1}{2} \int_0^L \frac{M^2}{EI} dx \quad (169)$$

where M is the bending moment given by

$$M = EI \frac{d^2 y_b}{dx^2} \quad (170)$$

where y_b is the beam position at any point x along its length. If we assume that the beam deformation is sinusoidal, then we have that

$$y_b(x) = f \sin \frac{\pi x}{L} + (e_1 + e_3) \left(\frac{L-x}{L} \right) + (e_2 + e_4) \left(\frac{x}{L} \right) \quad (171)$$

Substituting (171) into the bending moment equation (170), and the result into (169) we find the expression for the elastic energy stored in the rotor beam. After adding this result to (168) we obtain the total potential energy of the system¹

1. Of course, the 2nd and 3rd terms on the rhs of (171) do not contribute to the calculation of the potential energy stored in the beam, they however, will be used in subsequent developments of the model.

$$V = \frac{EI\pi^4}{4L^3}f^2 + \frac{1}{2}[k_1(e_1 - e_3)^2 + k_2(e_2 - e_4)^2 + k_3e_3^2 + k_4e_4^2] \quad (172)$$

4.3.2.2 Calculation of the Kinetic Energy in the Simplified Model

In the first place we have to determine the origin of the different terms that contribute to the calculation of the kinetic energy of the system. Once identified, classical mechanics considerations can be used to find the mathematical expression for each term. In our particular case, we expect contributions from:

- Beam displacement (including bending) $T_{bd} = \frac{1}{2} \int_0^L \rho_b \left(\frac{dy_b}{dt} \right)^2 dx$
- Beam inertia (about z) $T_{bi} = \frac{1}{2} J_b \left[\frac{d}{dt} \left(\frac{\partial y_b}{\partial x} \right) \right]^2$
- Disc displacement (for 5 discs) $T_{dd} = \frac{1}{2} \sum_{i=1}^5 m_i \left(\frac{dy_b}{dt} \Big|_{x_i} \right)^2$
- Disc inertia (about z) $T_{di} = \frac{1}{2} \sum_{i=1}^5 J_i \left[\frac{d}{dt} \left(\frac{\partial y_b}{\partial x} \Big|_{x_i} \right) \right]^2$
- Casing displacement (no bending) $T_{cd} = \frac{1}{2} \int_0^L \rho_c \left(\frac{dy_c}{dt} \right)^2 dx$
- Casing inertia (about z) $T_{ci} = \frac{1}{2} J_c \left[\frac{d}{dt} \left(\frac{\partial y_c}{\partial x} \right) \right]^2$

where the casing position y_c for any x is given by

$$y_c(x) = e_3 \left(\frac{L-x}{L} \right) + e_4 \left(\frac{x}{L} \right) \quad (173)$$

The total kinetic energy of the system results form adding all the contributions described above and making the required substitutions and calculations. We can use the final result along with (172) to write the Lagrangian of the system as

$$\begin{aligned}
\mathcal{L} = & \rho_b L \left\{ \frac{1}{4} \dot{f}^2 + \frac{\dot{f}}{\pi} (\dot{e}_1 + \dot{e}_2 + \dot{e}_3 + \dot{e}_4) + \frac{1}{6} [(\dot{e}_1 + \dot{e}_3)^2 + (\dot{e}_2 + \dot{e}_4)^2 + (\dot{e}_1 + \dot{e}_3)(\dot{e}_2 + \dot{e}_4)] \right\} \\
& \dots + \frac{J_b}{2L^2} [\dot{e}_2 + \dot{e}_4 - (\dot{e}_1 + \dot{e}_3)] + \frac{1}{2} \sum_{i=1}^5 m_i \left[f \sin \frac{\pi x_i}{L} + (\dot{e}_1 + \dot{e}_3) \left(\frac{L - x_i}{L} \right) + (\dot{e}_2 + \dot{e}_4) \left(\frac{x_i}{L} \right) \right] \\
& \dots + \frac{1}{2} \sum_{i=1}^5 \frac{J_i}{L^2} \left[\pi f \cos \frac{\pi x_i}{L} + \dot{e}_2 + \dot{e}_4 - (\dot{e}_1 + \dot{e}_3) \right]^2 + \frac{\rho_c L}{6} (\dot{e}_3^2 + \dot{e}_3 \dot{e}_4 + \dot{e}_4^2) \\
& \dots + \frac{J_c}{2L^2} (\dot{e}_4 - \dot{e}_3)^2 - \frac{EI\pi^4}{4L^3} f^2 - \frac{1}{2} [k_1 (e_1 - e_3)^2 + k_2 (e_2 - e_4)^2 + k_3 e_3^2 + k_4 e_4^2]
\end{aligned} \tag{174}$$

4.3.3 Calculation of the Normal Modes of Vibration

The next step is to substitute the Lagrangian (174) into (167) and perform the required partial and total derivatives to obtain a coupled system of five second order differential equations. This process is somewhat involved and tedious, so we present here the final result which can be written as a single vectorial equation

$$\ddot{\mathbf{Y}} + \mathbf{WY} = 0 \quad \text{with} \quad \mathbf{W} = \mathbf{M}^{-1} \mathbf{K} \tag{175}$$

where the vector and matrices are given by

$$\begin{aligned}
\mathbf{Y} &= \begin{bmatrix} f & e_1 & e_2 & e_3 & e_4 \end{bmatrix}^T \\
\mathbf{M} &= \begin{bmatrix} \mathbf{M}_1 & \mathbf{M}_2 & \mathbf{M}_3 & M_2 & M_3 \\ M_2 & \mathbf{M}_4 & \mathbf{M}_5 & M_4 & M_5 \\ M_3 & M_5 & \mathbf{M}_6 & M_5 & M_6 \\ M_2 & M_4 & M_5 & \mathbf{M}_7 & \mathbf{M}_8 \\ M_3 & M_5 & M_6 & M_8 & \mathbf{M}_9 \end{bmatrix} \quad \text{and} \quad \mathbf{K} = \begin{bmatrix} \frac{EI\pi^4}{2L^3} & 0 & 0 & 0 & 0 \\ 0 & k_1 & 0 & -k_1 & 0 \\ 0 & 0 & k_2 & 0 & -k_2 \\ 0 & -k_1 & 0 & k_1 + k_3 & 0 \\ 0 & 0 & -k_2 & 0 & k_2 + k_4 \end{bmatrix}
\end{aligned}$$

As we can observe, both matrices are symmetric. The mass matrix contains nine different elements which are:

$$\begin{aligned}
M_1 &= \frac{\rho_b L}{2} + \sum_{i=1}^5 \left[J_i \left(\frac{\pi}{L} \right)^2 \cos^2 \frac{\pi x_i}{L} + m_i \sin^2 \frac{\pi x_i}{L} \right] \\
M_2 &= \frac{\rho_b L}{\pi} + \sum_{i=1}^5 \left[m_i \left(\frac{L-x_i}{L} \right) \sin \frac{\pi x_i}{L} - \frac{\pi J_i}{L^2} \cos \frac{\pi x_i}{L} \right] \\
M_3 &= \frac{\rho_b L}{\pi} + \sum_{i=1}^5 \left[m_i \frac{x_i}{L} \sin \frac{\pi x_i}{L} + \frac{\pi J_i}{L^2} \cos \frac{\pi x_i}{L} \right] \\
M_4 &= \frac{\rho_b L}{3} + \frac{J_b}{L^2} + \sum_{i=1}^5 \left[m_i \left(\frac{L-x_i}{L} \right)^2 + \frac{J_i}{L^2} \right] \\
M_5 &= \frac{\rho_b L}{6} - \frac{J_b}{L^2} + \sum_{i=1}^5 \left[m_i x_i \left(\frac{L-x_i}{L^2} \right) - \frac{J_i}{L^2} \right] \\
M_6 &= \frac{\rho_b L}{3} + \frac{J_b}{L^2} + \sum_{i=1}^5 \left[m_i \left(\frac{x_i}{L} \right)^2 + \frac{J_i}{L^2} \right] \\
M_7 &= \frac{L}{3}(\rho_b + \rho_c) + \frac{1}{L^2}(J_b + J_c) + \sum_{i=1}^5 \left[m_i \left(\frac{L-x_i}{L} \right)^2 + \frac{J_i}{L^2} \right] \\
M_8 &= \frac{L}{6}(\rho_b + \rho_c) - \frac{1}{L^2}(J_b + J_c) + \sum_{i=1}^5 \left[m_i x_i \left(\frac{L-x_i}{L^2} \right) - \frac{J_i}{L^2} \right] \\
M_9 &= \frac{L}{3}(\rho_b + \rho_c) + \frac{1}{L^2}(J_b + J_c) + \sum_{i=1}^5 \left[m_i \left(\frac{x_i}{L} \right)^2 + \frac{J_i}{L^2} \right]
\end{aligned}$$

It follows from (175) that the normal modes of the rotor-casing system in our simplified model are completely determined by the information contained in the matrix \mathbf{W} . The five natural frequencies can be obtained after solving the eigenvalue problem

$$\omega_i^2 = [\text{eig}(\mathbf{W})]_i \quad \text{with} \quad i = 1, \dots, 5$$

in units of radians-per-second squared; in Hertz we simply have

$$v_i = \frac{\omega_i}{2\pi} \quad \text{with} \quad i = 1, \dots, 5 \quad (176)$$

To each frequency, there is an associated eigenvector which gives us information about the modal shapes

$$\mathbf{y}_i = [f \ e_1 \ e_2 \ e_3 \ e_4]_i^T \quad \text{with} \quad i = 1, \dots, 5 \quad (177)$$

4.3.4 Numerical Calculation

As our model represents a simplified version of the HPFTP rotor assembly, calibration is needed in order to find values of the natural frequencies that better match the real ones. From experimental measurements and calculations done in [4], it is known that in the case of the free rotor¹, the first bending mode occurs at 637.5 Hz. The first step is to introduce reasonable inertia and mass values for the rotor's beam and discs and set the stiffness coefficients to zero to represent a free rotor ($k_1 = k_2 = k_3 = k_4 = 0$). After several minor adjustments of the moment of inertia and mass of the beam, our model was calibrated to obtain a value of 637.5 Hz for the first bending mode with eigenvector²

$$\mathbf{y}_{free} = [1 \ -0.704 \ -0.565 \ 0 \ 0]^T$$

which can be represented graphically as shown in **Figure 46**.

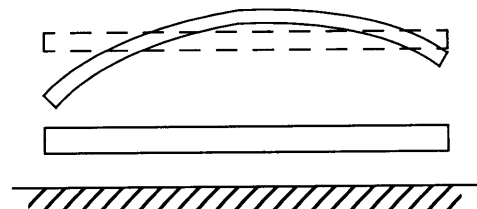


FIGURE 46. Graphic Representation of the First Bending Mode given by the Simplified Model

Tables 1 and **2** contain the beam and discs data used for this calculation. In particular, **Table 1** values are quite close to the real values. They describe a shaft of about 9 cms in diameter and density $\sim 8400 \text{ kg/m}^3$ which is close to *Inconel*, the material used in most parts of the rotor assembly.

1. By “free” we mean a rotor that is not attached to the casing.

2. Values normalized to the bending amplitude

Modulus of Elasticity (E)	1.7162×10^{11}	$\text{N}\cdot\text{m}^{-2}$
Geometric Moment of Inertia (I)	29.131×10^{-7}	m^4
Density (ρ_b)	42.4	$\text{kg}\cdot\text{m}^{-1}$
Moment of Inertia (J_b)	$\rho_b L^3/12$	$\text{kg}\cdot\text{m}^2$
Length (L)	0.60	m

TABLE 1. Beam Data Used in the Simplified Model (after calibration)

	Pump 1st	Pump 2nd	Pump 3rd	Turbine 2nd	Turbine 1st	
Position (x_i)	0.0814	0.2087	0.3320	0.4739	0.5386	m
Mass (m_i)	6.257	6.257	6.098	6.261	7.994	kg
Moment of Inertia (J_i)	3.643	3.643	3.535	3.161	3.307	$\times 10^{-2} \text{ kg}\cdot\text{m}^{-2}$

TABLE 2. Disc Data Used in the Simplified Model - from [4]

Once the rotor values have been chosen, we can assign values to the four spring constants in such a way that agreement with [4] is obtained for the lowest natural modes of the rotor-casing assembly; **Table 3** shows these values while the modal results are described in **Table 4**, where the frequencies reported in [4] are also shown. Just as an additional note of how reasonable these data are, the stiffness values used in the finite element procedure described in [4] are at least of the same order ($1.313 \times 10^8 \text{ N}\cdot\text{m}^{-1}$, for both bearings, and $2.6 \times 10^9 \text{ N}\cdot\text{m}^{-1}$ for the casing support to the engine - “powerhead” in [4]) as the spring constants found for our model.

Constant	Value ($\text{N}\cdot\text{m}^{-1}$)
k_1	2.1×10^8
k_2	1.5×10^8
k_3	1.9×10^9
k_4	2×10^9

TABLE 3. Spring Constants (after calibration)

Mode	Frequency (Hz)	Frequency from [4]	Representation
1	228.8	287.6	Rotor translation + bending
2	418.2	424.0	Rotor rocking
3	514.9	513.6	Rotor bending + casing translation
4	773.6	N.A.	Rotor/casing rocking
5	1076.7	N.A.	Rotor bending

TABLE 4. Modal Results

Chapter 5

Health Monitoring

In this chapter we present an overview of the application of dynamic models into a Health Monitoring (HM) scheme. HM is one of multiple terms commonly used to describe an involved process of verification of correct functionality of a given engineering system. In its most desirable form, HM works in real-time verifying that the system works as it should be, and in the case of failure, corrective measures should be taken to obtain a smart response to minimize the impact of that failure on the system integrity or to activate backup subsystems that eventually could help recover the system from its failed state. HM can also be used off-line to indicate the possibility that small failure signatures constitute themselves into trends that indicate the presence of deterioration of a specific subsystem. In a rocket engine, HM would provide operators with a health record of the engine that can be used to reduce operation costs as maintenance can be scheduled and directed to a particular element of the engine after analyzing it. In Section 5.1, we present a brief discussion about the historical background that supports the idea of HM implementation for rocket engines. In section 5.2, the concept of HM for Reusable Launch Vehicles (RLVs) is introduced. Sections 5.3 outlines the use of the thermodynamic nonlinear model developed in [3] to design linear plants and filters whose ultimate function is the detection and isolation of failures in the engine's operation. Finally, in section 5.4 we explore the use of rotordynamic models and several filter techniques to develop algorithms that are able to manipulate vibrational data from the engines, specifically, from the

turbomachinery. It is important to mention that most of the results presented in this chapter (particularly those in section 5.4) are preliminary only.

5.1 Historical Context

The US space industry remains in a state of constant evolution. Today's evolving path, however, is different from the one that prevailed during the early years of its existence. In those days the government constituted itself as the leader of the field, motivated by the cold war competition with the now extinct USSR. The space efforts were focused on accomplishing a series of political goals that allowed an unprecedented growth of scientific and technological resources that initiated the new "space era." Research, implementation and manufacturing costs were not the principal criterion for space technology development, they were actually far behind performance and schedule. If the political goals were to be met, funding had to be virtually unlimited. Almost all early manned programs, from Mercury to Apollo, were based on that premise. It was not until a few years ago that, with the cold war over, there were practically no more significant political incentives that sustained the idea of space exploration in the same fashion as before. The result of this evolution is a government that is slowly withdrawing its leading role from the space scenario. As dramatic as it can sound, it is very unlikely that the new policies will cause a slowdown of the space industry health; the reason is that many of the activities "abandoned" by governmental space agencies are being taken over by private investors who see a firmament (literally) full of business opportunities. It is expected that in the next decade or so, commercial space activities will show a near exponential growth as new concepts in communications, remote sensing and even tourism are implemented on space based platforms [28]. Of course, these platforms need to get on earth orbit first, which implies a growth in the space launch vehicles industry. Just as an example, the Teledesic constellation concept requires the launch of an average number of 300 satellites in a period of about one year to reach full functionality. Other constellations and "routine" spacecraft will be launched at the same time, and service to existing constellations also needs to be considered. This means that on peak times, daily launches can be expected. As of today, there is not enough launch vehicle capacity, in number of rockets, land

equipment, and support installations to supply such demand. A new and vigorous strategy needs to be developed in the immediate future in order to cover these launch requirements.¹

In a space industry motivated by profit, cost is no longer an additional requirement used to determine a specific concept configuration, but rather the main driver for design, implementation and operations. Rigid cost constraints involved in the development of new space systems and competitiveness among several satellite manufacturers and subcontractors have triggered the appearance of good number of creative ideas that consolidate into a general decrease of costs, meeting at the same time mission requirements with the required level of performance.

Launching those concepts into space is a different matter. The cost of launching a spacecraft of a given mass into earth orbit has not decreased as fast as the cost of the satellite itself. We do not need a lot of insight in this subject to acknowledge the need of imaginative approaches to the launch vehicle cost problem. For the first time in the space technology history, the orbit launch vehicle development can turn itself into a profitable industry.

5.2 Health Monitoring for Reusable Launch Vehicles

There are several companies that at the present time are looking for new formulas to decrease the costs involved in launching spacecraft into earth orbit. Without involving ourselves in a precise description of all the possible alternatives considered, we can start by recognizing the fact that reusability is one of the main factors that could ultimately allow a dramatic decrease of general launching costs. The goal of this strategy is the creation of a series of reusable launch vehicles (RLVs) that have practically no disposable components, in that way costs would eventually reduce to operations and maintenance. Airline type management can then be implemented, taking advantage of its relatively large

1. Satellites fail after certain amount of time and to maintain the constellation operability they need to be replaced. It turns out that maintainability creates a permanent launch requirement that would eventually sustain the growth of the launch vehicle industry.

experience with complex reusable systems. It is expected that such innovations would allow a decrease in space launch costs anywhere from 50 to 90% of actual costs.¹

For the development of new RLVs, considerable amount of experience can be extracted and applied from the first RLV ever devised, the Space Shuttle. Completely designed in the 70's, the Space Shuttle does not rely on much new technology in materials, electronics and systems developed in recent years, and also maintenance becomes extremely expensive given the enormous complexity involved in pre-launch issues. Even though the Space Shuttle is not a 100% reusable vehicle since the propellant tank is completely lost and a relatively large number of components need to be replaced after each launch, it is an excellent test bed for new developments.

One of the most critical elements implicated in the success of any space mission is the propulsion system. For RLVs this is particularly true since there are very strict requirements that the engines need to meet; overall, they need to be close to 100% in reliability, defined here as the probability that the engine will be fully functional and perform adequately along its mission lifetime. Besides this, the engines also need to be maintainable and cost-effective.

The Space Shuttle makes use of three SSMEs as its main propulsion system. The SSME itself was the first reusable rocket engine successfully employed. The high success rate of the SSME (close to 100% in flight performance) is due to a detailed verification process that operates between launches, including close inspections of each component. This usually means disassembling the whole engine as part of the flight validation process. A large number of tests are then performed to verify that the parts comply with the regulation standards that allow them to be used again in a new mission. During flight, the SSMEs are closely monitored to determine the occurrence of possible failures with a "redline" technique, in which several important parameters of the engine (state variables), such as pressures, temperatures and flow rates are observed simultaneously and a comparison

1. The high figure is particularly used by the developers of the "VentureStar", a single stage to orbit (SSTO) vehicle built with extra light materials that allow the integration of all subsystems (including engines and propellant tanks) into a single, completely reusable vehicle. Several new concepts involved in the vehicle's design are due to be tested with a half-scale demonstrator, the X-33, in 1999. A full description of this interesting project can be found in the internet at www.venturestar.com

procedure is used to determine whether these values are within an acceptable range of operation [26]. If one or more of these parameters change to a value outside the established range, then a failure is declared and appropriate actions are taken to force a safe and controlled shutdown of the engine. Depending on the point along the flight path in which the failure occurs, a mission abort is commanded or not. All this process is automatically controlled by a dual-redundant computer mounted on each engine linked with the Space Shuttle's main computer system.

In a way, the redline technique constitutes itself as the most basic form of Health Monitoring for rocket engines. For future generation RLV engines, HM will definitively turn into an important design requirement.

For illustration purposes, we limit our description of HM to the part involved in the tracking of the engine's state variables, in particular, we will show in section 5.3 how can this be used in a Failure Detection and Isolation (FDI) scheme.

5.3 Failure Detection and Isolation

As we mention in section 5.2, the “redline” is one of multiple techniques that can be used for failure detection, however, it is not unique in the sense that there are several other ways in which failures can be detected; other methods include pattern recognition, data trending using neural networks [18, 19], plume spectroscopy, vibration monitoring [20], and model-based failure detection [21, 22]. Full confidence of a HM FDI scheme would be attained by using these, or maybe more, techniques together as in some instances their functions become complementary. Almost all these techniques involve the tracking and estimation of the engine's state variables, for example, redlines track the states with sensors verifying that their values remain within safe intervals; neural networks use a series of complex associations that correlate a change of a particular variable with changes in the rest of variables and then mark trends that can be categorized as failures. In particular, the most analytic method is the model based estimation in which a mathematical model is used to estimate the state variables. In the particular case of the

SSME, this technique was used by N. Ho [23] to look for failures and their origin in sensors and control valves based on the model developed by Rocketdyne [3].

The problem of having sensor and valve failures is not trivial. In [24] an assessment of different SSME's failures was done, and it was found that simple sensor failures can result in catastrophic situations. For example, in the SSME test number 901-284, with engine 0010, the MCC chamber pressure sensor seal broke at some point during the engine start sequence, as a result the sensor measured the significantly higher pressure inside the coolant jacket of the MCC. The engine's computers indicated an unexpected increase in RPL, in response closed-loop operation commanded a throttle decrease to the FPV and OPV actuators. As a result, an anomalous oxidizer to fuel mixture ratio resulted in the MCC. Specifically, the mixture ratio dropped from 6 to 3.5, the chamber pressure dropped from 3000 to 1800 psi, causing complete off-design behavior in the whole engine. As a consequence, the HPOTP cooling subsystem overcooled the turbine section; ice formed resulting in an increase of axial loads, thus overloading the balance pistons, causing the turbine to rub with its casing, extreme friction led to a fire and ultimately an explosion that damaged most of the engine; all because of a simple sensor failure.

In another occasion, a redline sensor failure almost caused a mission abort while the Space Shuttle was in its climb phase, but fortunately control personnel determined (using their own experience) that the failure was not in an engine component. Other sensor failures had caused the engine to shutdown even at the critical time between the engine start-up and the ignition of the SRBs.

As we emphasized in chapters 2 and 3, the SSME operates at extreme conditions, therefore, the positioning of sensors becomes a critical issue as their presence must in no way interfere with the engine's operation. Drilling holes inside the MCC and cooling jacket is something that engineers do not like to do very much. When necessary, they prefer to make a single, minute hole. This is one of the reasons for the absence of sensor redundancy in rocket engines. In its place, a FDI system can be implemented to increase as much as possible the reliability of the engine.

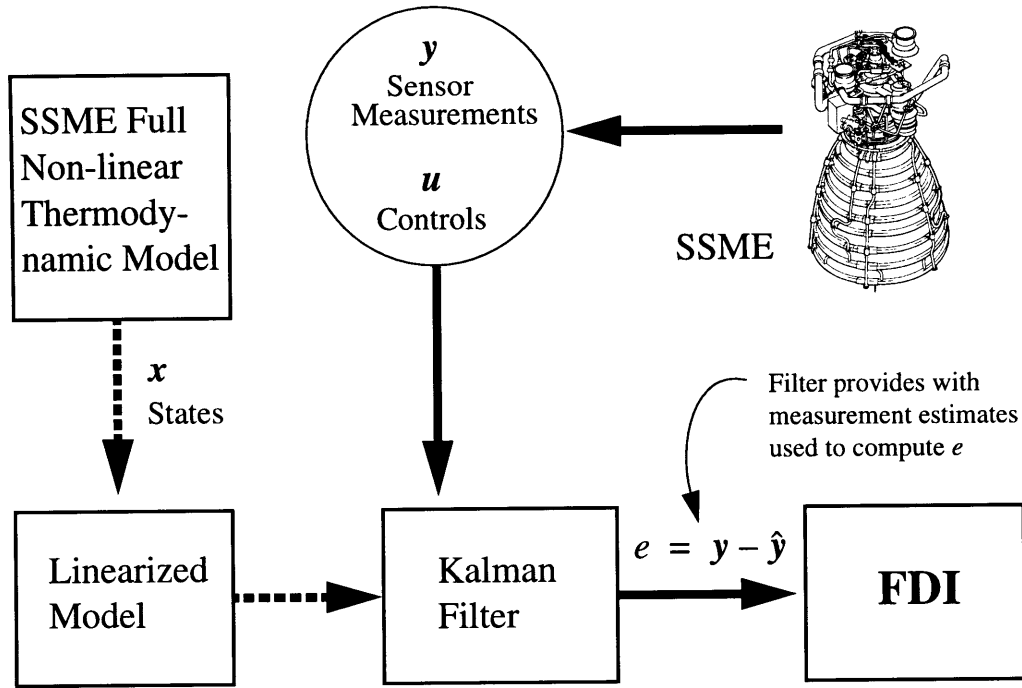


FIGURE 47. Model-Based FDI Strategy

The FDI model-based approach used in [23] is described in **Figure 47**. The SSME thermodynamic nonlinear model described in chapter 3 can be written as

$$\dot{x} = f(x(t), u(t)) \quad (178)$$

A set of sensors also needs to be selected. In general, a sensor can measure a state variable or an “intermediate” variable which is function of several state variables. In this way, the measurement equations are

$$y = h(x(t)) + v(t) \quad (179)$$

where h can be a nonlinear function of the state variables and v is the measurement noise, which is assumed in [23] as Gaussian, white with zero mean and known covariance. Once the nonlinear state and sensor models are developed, they can be linearized about a specific operating point or RPL, the linearization allow us to write (178) and (179) in a discretized form

$$\begin{aligned}x_{k+1} &= A_k x_k + U_k u_k + B_k r_k \\y_k &= C_k x_k + W_k u_k + D_k r_k\end{aligned}\tag{180}$$

where the matrices A , U , C and W are the Jacobians of (178, 179) evaluated at the selected operating point; the terms $B_k r_k$ and $D_k r_k$ represent exterior disturbances to the model, such as linearization errors and measurement noise.

Once the linear plant (180) is obtained, it can be used to design linear Kalman filters whose inputs are the sensor measurements.¹ The Kalman filter provides least-squares estimates of the engine's state variables and sensor outputs. The question of how close these estimates are to the real (nonlinear) states depends on the quantity and type of sensed variables. Therefore, the model based technique also gives a good indication of the minimum number of sensors n and their locations that maximize system observability and traceability; this can be particularly useful while in the design stage of a rocket engine or any other complex engineering system. In [23] it is found that a set of $n = 15$ sensors is enough to ensure good observability of the system's 38 state variables.

Failure detection is then implemented by observing the sensor residual e , which can be defined as the difference vector between the real measurements and their estimates

$$e_k = (y - \hat{y})_k \quad \text{for } k = 1, \dots, n\tag{181}$$

When there is no failure, the values of e_k remain close to zero given that the estimates are accurate. If at some particular time, a sensor fails, the residual will experience a departure from its nominal close to zero position. In practice, each sensor failure produces a different signature in the change of e . A threshold value can be set; if the residual crosses it, a failure is declared.² The residual signatures can then be categorized with the aid of hypothesis testing to isolate the origin of the failure. The magnitudes of such tests provide

1. In [23] the measurements are taken from the nonlinear plant (179). In practice, real-time or stored SSME measurement data can be used instead; the algorithm remains unchanged regardless of the origin of the sensor data.
2. There is of course a trade-off in the threshold selection; a small value would maximize detection at the expense of an increase in false alarm event probability, on the other hand a high value could cause an increase of missed alarm probability.

more useful information. For example, they give an indication of the degree of distinguishability that a particular failed sensor has with the rest of the sensors in the set. Once more this is particularly helpful to select the most effective set of sensors for the engine. The same procedures can be directly applied to control valves. Model-based approach for FDI was extended to SSME's component or plant failures by N. Ho [25].

5.4 The Use of Liquid Rocket Engine Vibration Data

The thermodynamic quantities obtained in the model development of chapter 3 have the characteristic of possessing heavily damped dynamics (see for example **Appendix C**); this is particularly important for the FDI algorithms discussed in section 5.3 because they are allowed to work with practically steady-state values. This is not the case for vibration data from liquid rocket turbomachinery, very small damping is present and a time-accurate tracking of the modes becomes a necessity. Rocket engine turbomachinery has in general a very rich vibratory spectrum, and so, a considerable amount of information can be extracted from it. In some cases there is also overlapping of vibratory frequencies with those of the thermodynamic variables, therefore coupling is possible, increasing the importance of the ability to monitor and manipulate vibration data.

By the mid 80's, vibratory data were considered by Cikanek [26] as "very difficult to characterize and interpret; taking substantial computational effort and expert analysis." In that way, the only part of HM involved with vibratory data analysis was the root-mean-square (RMS) thresholding, which is just another type of redline technique for failure detection; the vibrations are monitored and their amplitudes averaged out throughout time. If it happens that the signal crosses a given threshold, a failure may be declared. It was predicted in [26] that this kind of vibration data analysis would be the only one feasible for years to come. Of course, since 1985 substantial advance in computing capabilities have been achieved, and Cikanek's argument may not be valid anymore. With today's computers it is possible to analyze vibration data in a more sophisticated way, and the possibility may exist of doing so in real-time.

Although, vibration amplitude is what causes structural damage to a rocket engine, it is important to acknowledge that large amplitudes in systems with low damping constitute a response to operation at unstable conditions. It is more useful to characterize the origin of such instabilities instead of monitoring the absolute amplitudes of the oscillations. As we mention in chapter 4, among several sources of vibration in a rocket engine, the most recurrent and important is the one that comes from the turbomachinery. We also pointed out earlier that in order to avoid such instabilities a closer look at the operational frequencies of the rotor-casing subsystems should be taken. In this direction, the most desirable form of data analysis is the one involving spectral tracking. We can use a Fourier analysis to transform a time-domain signal coming from integrated accelerometer or proximity sensors mounted on the engine into frequency-domain data. The most general method for doing so would be to take the Fourier transform of the signal over a given time *window*. There are two ways in which this can be done; (a) in **Figure 48a**, a window covers certain time interval Δt_w in which the transformation is performed, after the calculations leading to the mapping of the window's time-domain data into a point in the frequency domain are made, the window is shifted an interval Δt_s ahead and the process is repeated, in this particular case $\Delta t_w = \Delta t_s$; (b) in **Figure 48b**, a similar window is used to perform the mapping, and once done, the window shifts slightly, overlapping with old time-domain data, such that $\Delta t_w > \Delta t_s$. It is clear that procedure (a) maps fewer points in the frequency domain, therefore ignoring probable changes in the oscillation characteristics that could happen in a particular region of a single window. Turbomachinery rotordynamics are quite fast, allowing instabilities to develop rapidly, and it is possible that such events would remain hidden from tracking using (a). In (b), such concealing can be reduced at no expense if an algorithm which does not re-uses already processed data is considered.

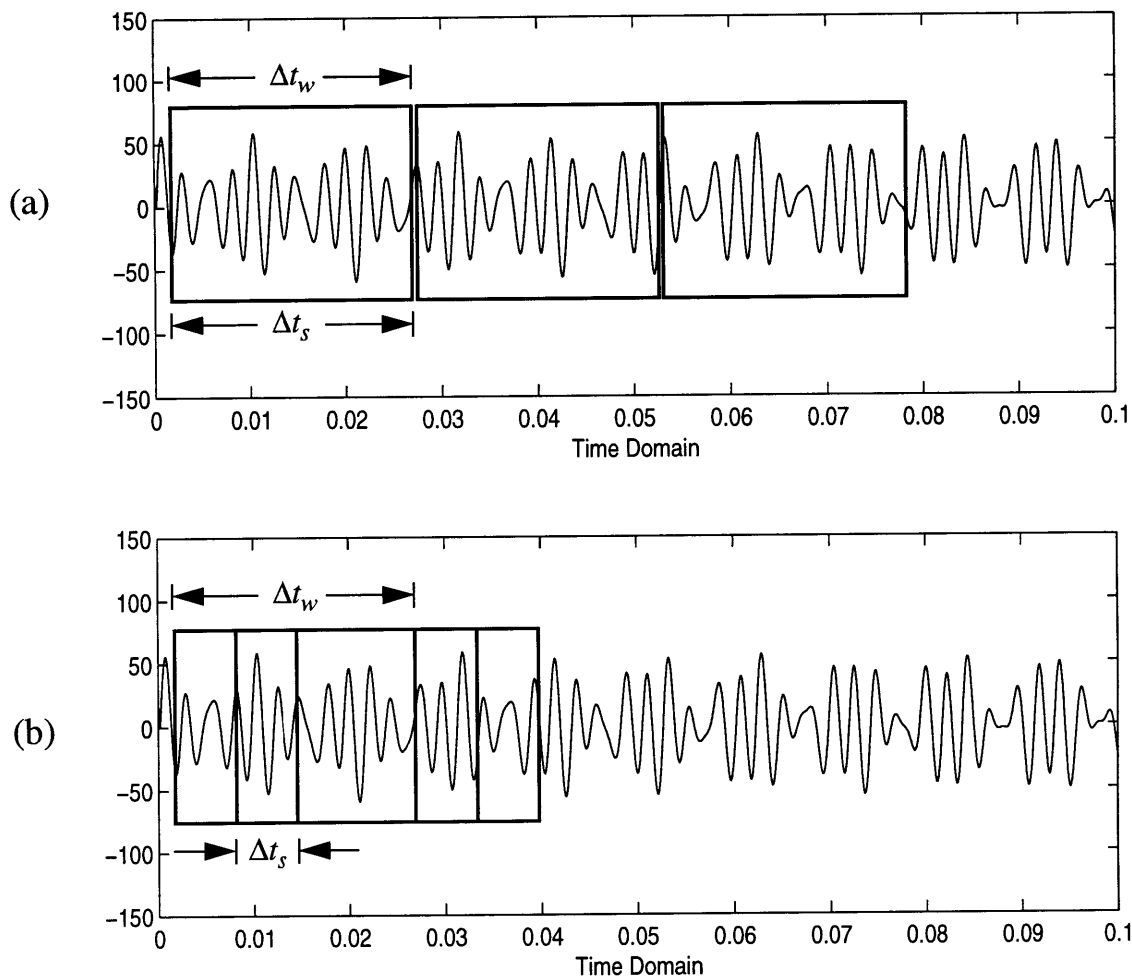


FIGURE 48. Fourier Transformation of Time Domain Data (3 windows, same size)

Another type of signal processing in real-time can be implemented besides the Fourier transform; the main idea is to track the signal components in the time domain. An analysis of this type can provide us with all the information needed to determine the characteristics of the vibrational spectrum. In particular, we are interested in tracking the oscillatory response of the turbopumps in frequency bands near to the known natural modes. In a very general form, this tracking algorithm should be able to separate individual modes from a given signal; this strategy is depicted in **Figure 49**.

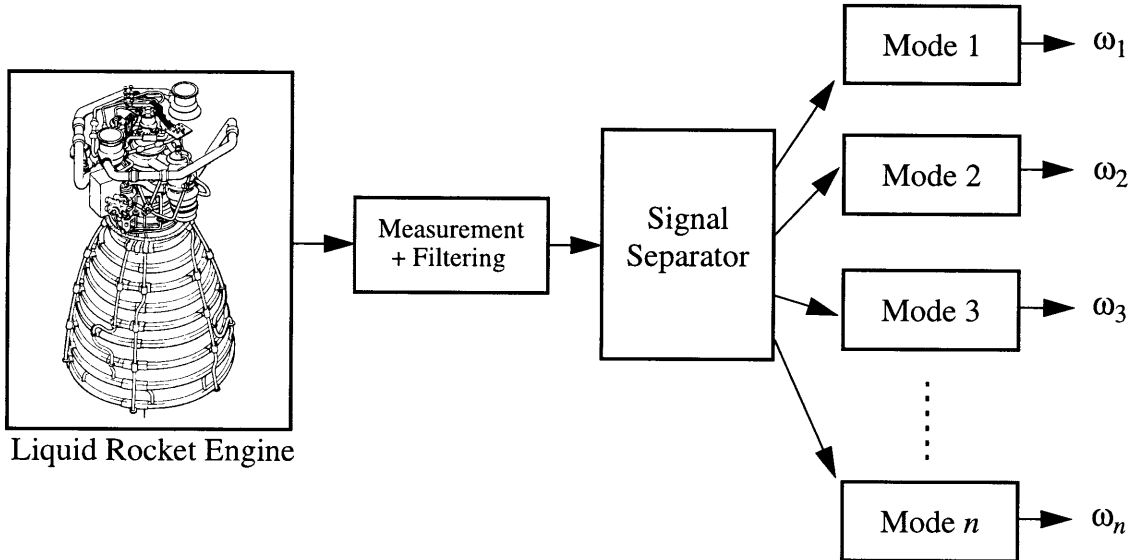


FIGURE 49. Vibrational Data Tracking Strategy for n Modes

Data are first taken from the rocket engine sensors which are placed in specific locations determined by their ability to detect the vibrations of interest.¹ Raw data are then measured while unimportant bands (those bands with which we are not concerned, such as extremely high or low frequencies) are filtered out. The filter's output is the vibration signal containing all the spectral information. A signal separator can be then implemented to obtain, say, n estimates of n individual modes, each one of them has a distinctive frequency, which is then also known.

A well known adaptive algorithm which can be used to perform such separation was extracted from [27]. Let us assume that n sinusoids $x(t)$, each one with a distinctive frequency and with arbitrary amplitude, are added together to conform the source signal S measured by the instrumentation. In a discretized form,

$$S_{k+1} = \sum_{j=1}^n x_{k+1}^j + \sigma_x N \quad (182)$$

1. For example, sensors can be placed near to the turbopump's bearing supports to acquire data concerning the rotor's rocking, translation and, possibly, bending vibration modes.

where $\sigma_x N$ is the measurement noise, which is assumed here to be equal to zero for simplicity purposes. Note that an undamped j^{th} sinusoid component of frequency ω^j satisfies the following difference equation

$$\begin{aligned} x_{k+1}^j &= ax_k^j - x_{k-1}^j \\ \text{with } a^j &= 2\cos(\omega^j t_s) \end{aligned} \quad (183)$$

where t_s the length of the time step. An algorithm that uses the above representation to track the signal will now be described. It consists of two laws: tracking and adaptation. The tracking part is concerned with estimating x_k using the most current estimate of a , while the adaptation law is concerned with updating the estimate of a . Specifically, the tracking part is given by

$$\hat{S}_{k+1} = \sum_{j=1}^n \hat{x}_{k+1}^j \quad (184)$$

in which \hat{x}_{k+1}^j represents the estimate of the j^{th} sinusoid component. These are updated according to

$$\hat{x}_{k+1}^j = \hat{a}_k^j \hat{x}_k^j - \hat{x}_{k-1}^j + c_g (\varepsilon_k - \varepsilon_{k-1}) \quad (185)$$

where c_g is the gain on the error, which is defined here as

$$\varepsilon_k = S_k - \hat{S}_k \quad (186)$$

and the update of \hat{a}_k^j is given by the following adaptation law

$$\hat{a}_k^j = \hat{a}_{k-1}^j + k_g^j \text{sign}(\hat{S}_{k-1}) \varepsilon_k \quad (187)$$

where k_g^j is the adaptation gain and the sign function is given by

$$\text{sign}(\alpha) = \begin{cases} 1 & \text{if } \alpha > 0 \\ 0 & \text{if } \alpha = 0 \\ -1 & \text{if } \alpha < 0 \end{cases}$$

The main question is whether an algorithm such as the outlined above converge. That is, does $\hat{a}_k^j \rightarrow a^j$? We shall not dwell into the subject, but sufficient conditions for the convergence of these algorithms are too stringent. Algorithms that deal with fast converging properties are an open research area. It is possible however, to perform extensive simulations and determine the range of frequencies and amplitude ratios for which such algorithms converge successfully. In the remainder of this section, we shall present some numerical results concerning the use of such algorithms, and we shall suggest possible experimental improvements.

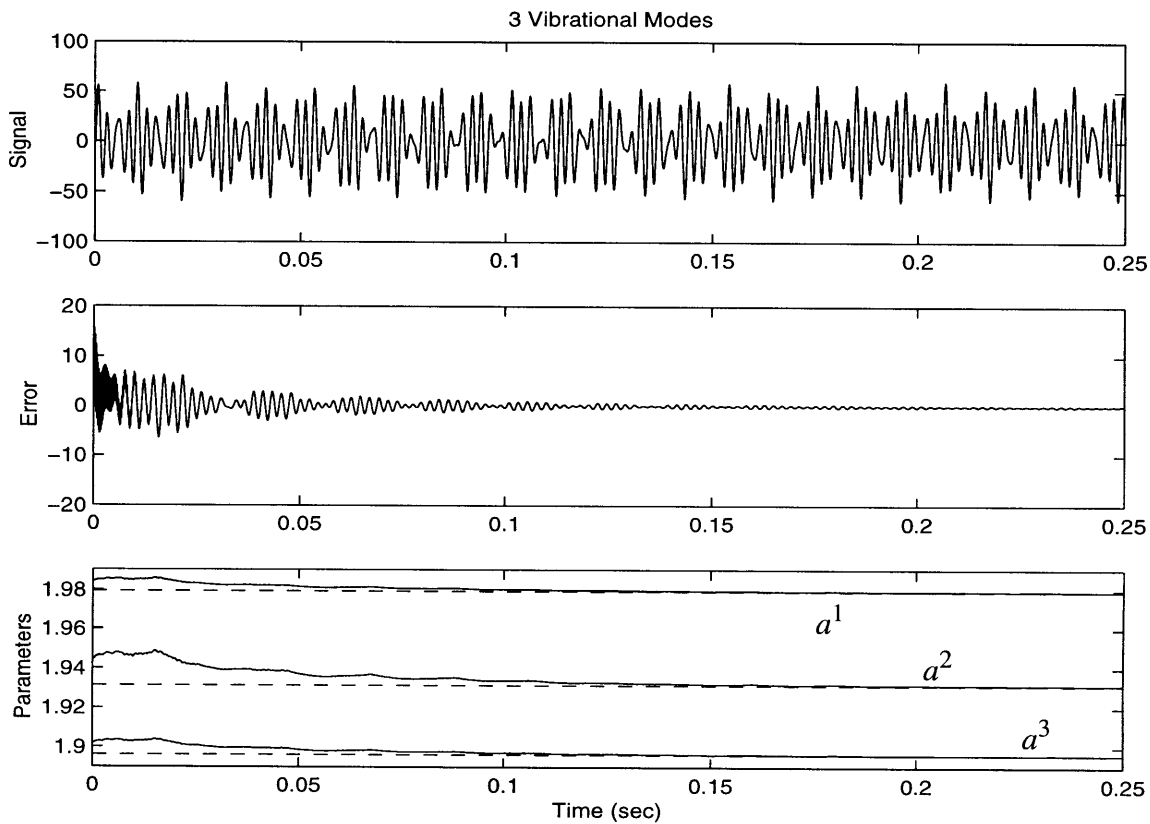


FIGURE 50. Results from the Tracking Algorithm (3 Modes, exact gains)

Figure 50 shows the results of using the algorithm of eqs. (184-187) with the 3 first normal modes of the HPFTP shown in **Table 4**, section 4.3.4. The gains used here are

$$k_g^1 = 0.000015, k_g^2 = 0.000041, k_g^3 = 0.0000185, \text{ and } c_g = 0.65 \text{ with } t_s = 0.0001.$$

The amplitudes for this example were arbitrarily selected as 10, 30 and 20 units. As we can see the error converges to zero in time, allowing the parameters to approach the dashed lines which represent the correct frequencies. This procedure has, however, a major problem concerned with the selection of the adaptation gains k_g^j . It turns out that only a unique selection of gains results in convergence of the error to zero for a given signal composed of sinusoids with given amplitude and frequency. Any other combination of gain values causes the error to oscillate around zero without decaying, as the parameters converge to erroneous frequency values if close to them, or simply oscillate also without decaying.

This algorithm, however, possesses the advantage of working with the signal at the same time that it is acquired by the sensors, unlike the Fourier transform which requires “windowing.” The question of which method is best for a tracking application depends on the speed and accuracy from each of them. While calculations (184-187) appear to be simple and fast, Fourier transforms are much better understood, reliable and robust. If speed precludes the use of Fourier transforms for vibration analysis in real-time, then perhaps a combination of both methods is the best solution; we can increase the accuracy of the tracking method if the initial conditions for \hat{a}_k^j are quite close to the decomposed signal values. To obtain these, we can use a Fourier transform performed only once during a given time at the beginning of the signal generation.

Figure 51a shows the resulting signal error (186) when introducing arbitrary gain values ($k_g^j = 0.0001$ for $j = 1, 2$ and 3) in the same example described above. In **Figure 51b** the same values and algorithm were used with the difference that the \hat{a}_k^j initial conditions were obtained from a Fast Fourier Transform (FFT) performed while in the first 0.05 seconds of the signal generation. This initial value selection allows the algorithm to reach fast convergence without the need of optimizing the gain values.

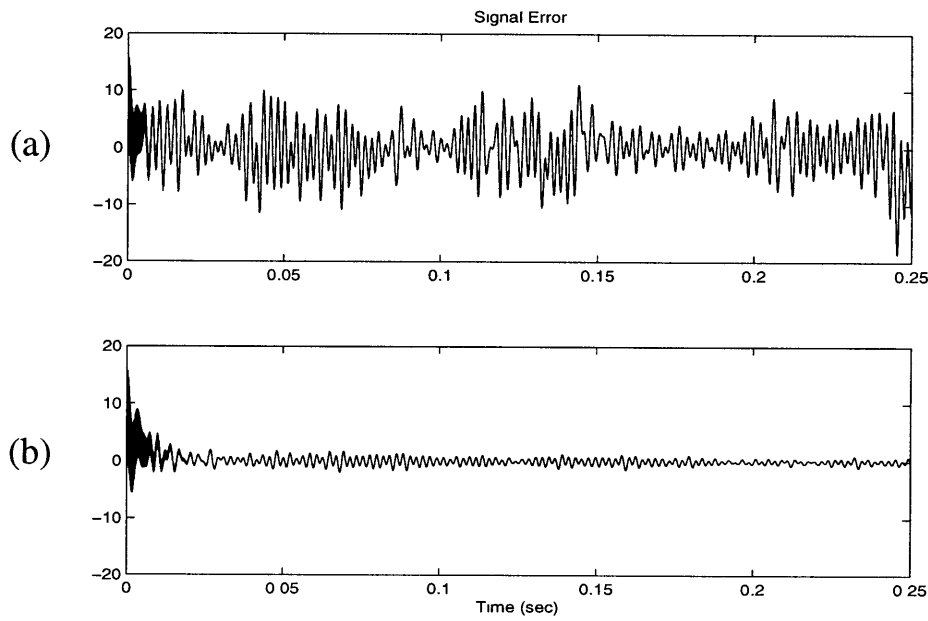


FIGURE 51. Error Signals From the Tracking Algorithm (using FFT)

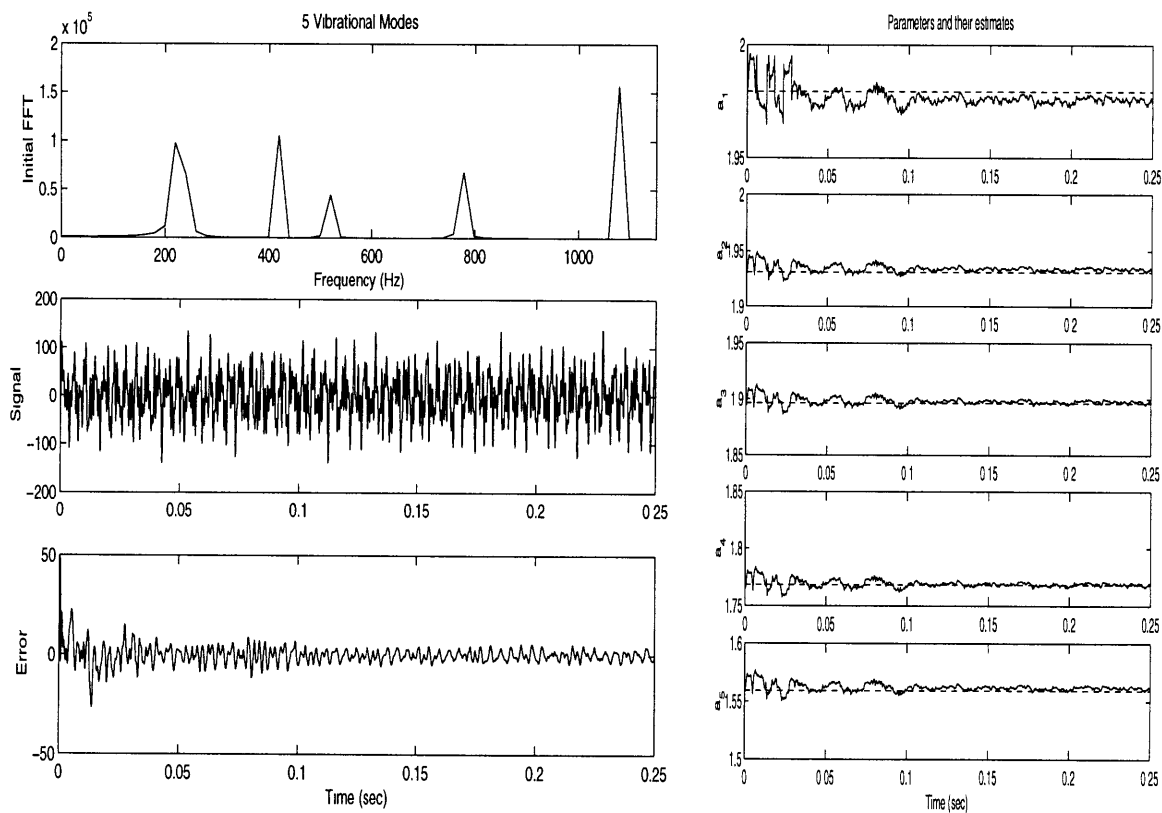


FIGURE 52. Results for the Five Modes of the HPFTP (using FFT)

Figure 52 shows the results of using this modified algorithm to track the five vibration modes of the HPFTP rotordynamic model of chapter 4 departing from the same arbitrarily selected gain values (k_g 's = 0.0001), and c_g = 0.35. The amplitudes used were (from lowest to highest mode) 40, 30, 20, 25, and 35 units.

It is very likely that, in real turbomachinery systems, one or more of the modes are dominant over others (a single frequency in the presence of noise, for example). One of the requirements for the tracking algorithm is stability even if such event occurs. **Figure 53** shows the results of the five mode adaptive tracking algorithm initialized with an FFT introducing one dominant mode, in this case the one with highest frequency. The amplitudes used in this example were modified to 1, 1, 1, 1, and 100 units. By looking at the time scale we note that for this particular example convergence is obtained relatively fast as compared with the case shown in **Figure 52**.

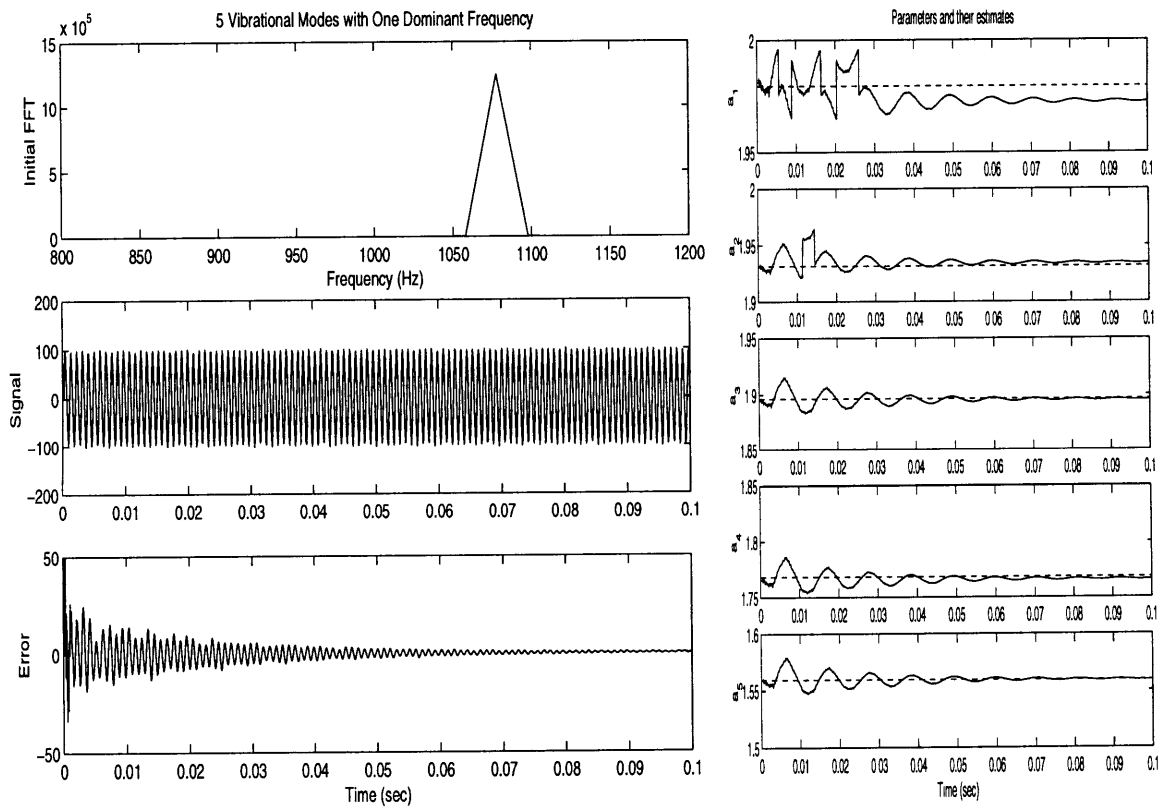


FIGURE 53. Results for the Five Modes of the HPFTP (with highest dominant mode)

If the dominant mode is the one with the lowest frequency the algorithm does not converge with the same values of c_g and t_s . **Figure 54** shows the results where the dominant mode is the one with the lowest frequency. For this case $c_g = 0.16$ and $t_s = 0.0004$. The results appear satisfactory, but it must be noted that the selection of the appropriate new values of c_g and t_s required additional trial and error, and that no method is at hand to do this automatically.

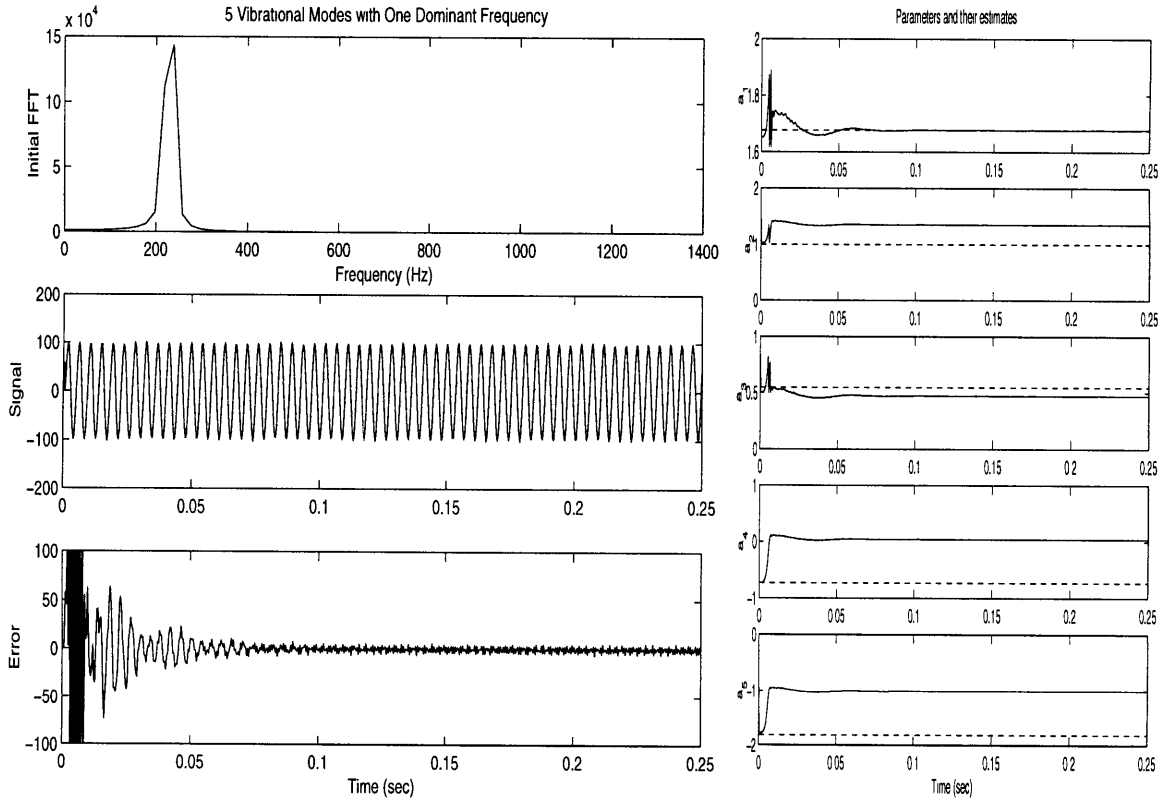


FIGURE 54. Results for the Five Modes of the HPFTP (with lowest dominant mode)

There is still more work to be done regarding the development of tracking algorithms and their potential use in a HM scheme. In this direction, an experiment was performed in which the Fourier initialized tracking scheme was used to follow a single frequency while it changed its value in an abrupt way.

Figure 55 shows the results of this experiment. Initially, an FFT was used to obtain the initial \hat{a}_k^j values from a sinusoid signal with a frequency of 229 Hz and an amplitude of

10 units. Immediately after this, the tracking algorithm adjusted itself to follow the mode. Suddenly, at $t = 0.1$ sec, an abrupt change in the measured signal occurs. The change is categorized as a frequency shift from 229 Hz to 249 Hz and an amplitude shift from 10 to 30 units.

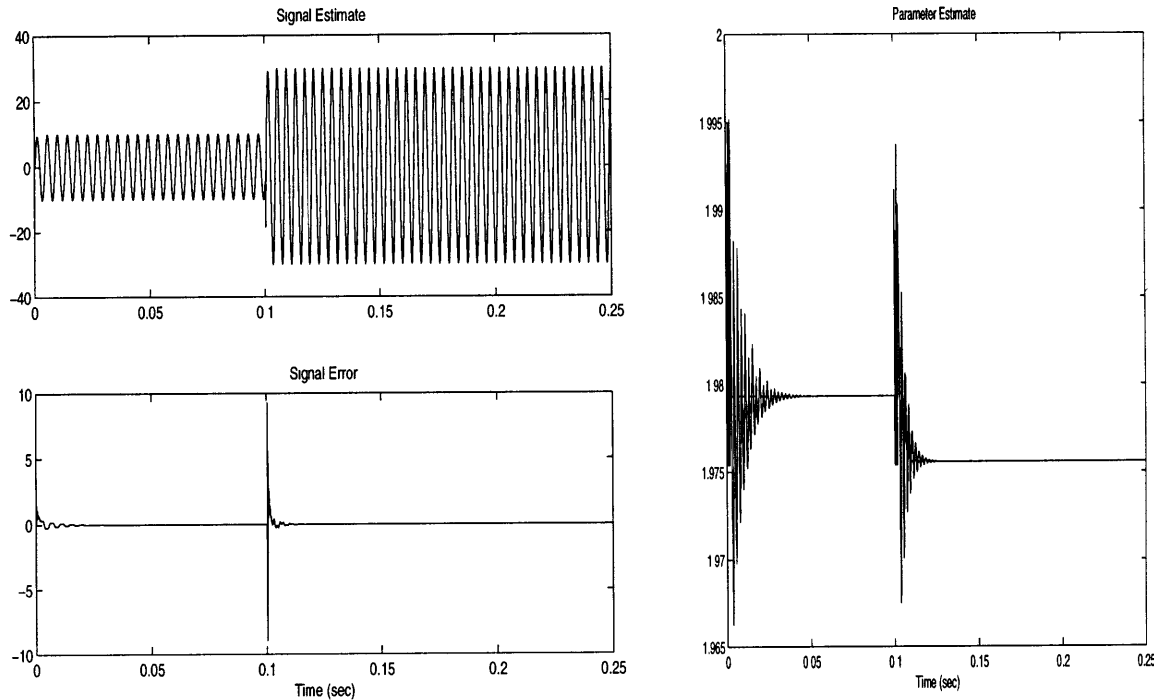


FIGURE 55. Response of the Tracking Algorithm to an Unknown Anomaly

This kind of signal degeneration can be associated with a system's malfunction. With this kind of results we can start thinking about an FDI strategy using the tools presented in this section. This, however, requires more experimentation time and analytic development of algorithms such as the one introduced here.

The final point would be to answer the question on what a particular signal degeneration means, in other words, what are the causes for its appearance? Rotordynamic models such as the one developed in chapter 5 could help us to determine the relationships among signal degradation and component failures.

It is important to acknowledge that the results presented in this section are preliminary only, there are unresolved issues in the air and more experimentation and analysis to be

done concerning the adaptation algorithms presented, and that is the subject for further research beyond the time-line of this thesis.

Chapter 6

Conclusions

In this thesis, we have been able to develop, from first principles, a detailed liquid rocket engine thermodynamic model for the SSME; a comparison with the model reported by Rocketdyne [3] was made to verify its accuracy and completeness. In this way, the systematic approach used here can be repeated and extended to develop the same type of models for other rocket engines, such as the main propulsion systems for future reusable launch vehicles, or any other liquid rocket engine in use today.

Perhaps the most valuable aspect of this work is the fact that a considerable amount of information regarding the operation and modeling of liquid rocket engines has been put together in a single document; it is difficult to find in the literature a volume dedicated to find end-to-end mathematical expressions that describe a complex propulsion system such as the SSME. We have tried to find these expressions giving, at the same time, a physical interpretation of the phenomena involved, marking at all times the limitations of an analytic approach.

With the same spirit, simple rotordynamic models for liquid rocket engine turbomachinery were also developed and compared with more complex finite element calculations [4]; a review of the vibration problem was made to justify the introduction and importance of having good knowledge of a turbomachine's normal modes characteristics.

Such knowledge is required to avoid dynamic instabilities that could have serious consequences in the overall engine's operation.

The thermodynamic and rotordynamic models developed here can be used for simulation purposes to determine the best way in which the physical systems should be operated to maintain safety and performance. On the other hand, we have reviewed the alternative of applying the thermodynamic model as a part of a health monitoring scheme in which the state variables are observed and estimated to determine possible failures in sensors, controls valves or components. Some preliminary real-time algorithms for tracking the vibration modes from the turbopumps were also reviewed, and their possible application into a health monitoring scheme was discussed.

Future work in this topic includes the development or improvement of dynamic models for different liquid rocket engines and their application into a self-consistent health monitoring strategy, which should include an analytic approach to tackle the elusive problem of tracking and using in an efficient manner complex vibration data.

Appendix A.

Glossary of useful abbreviations

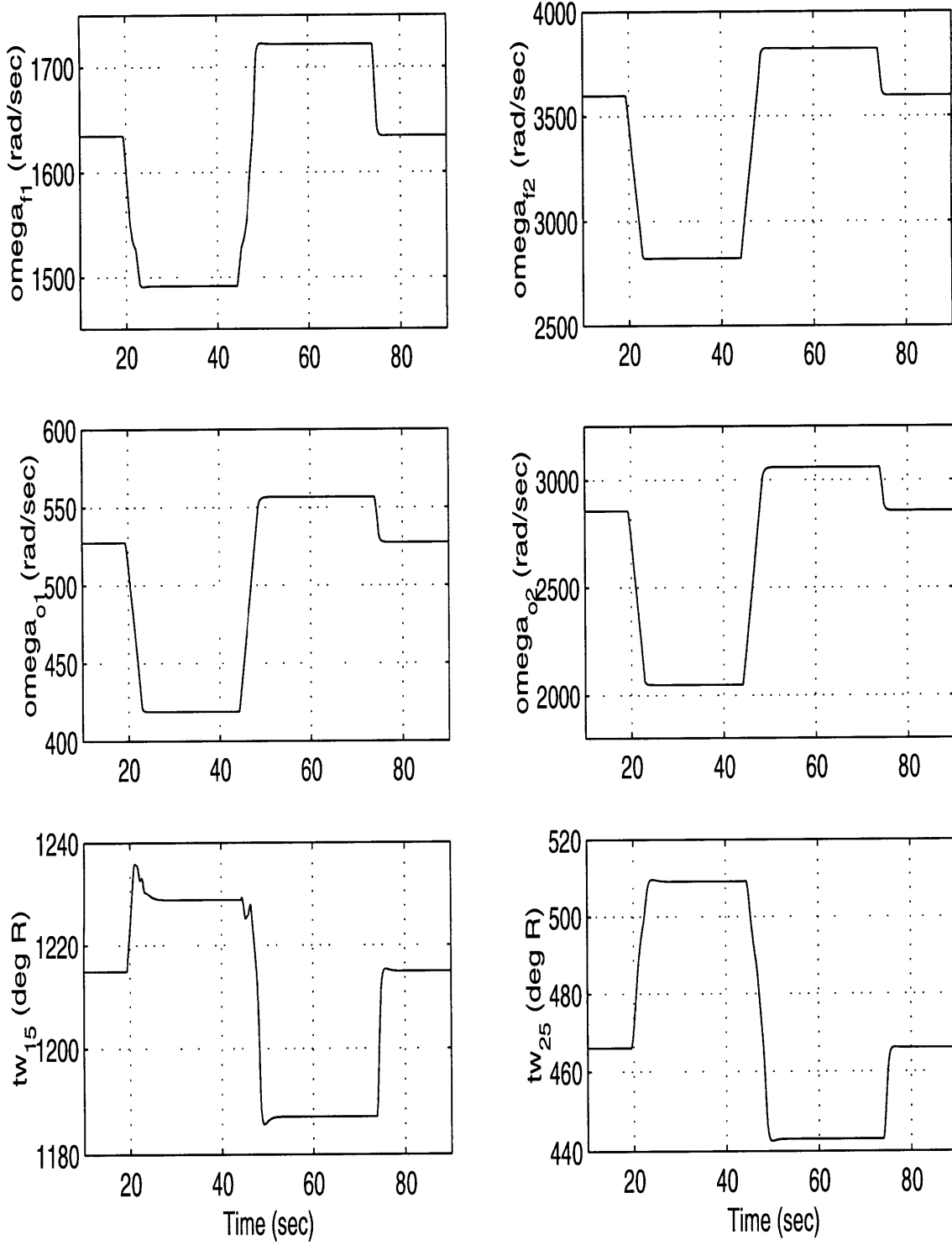
ASI	Augmented Spark Igniters
CCV	Chamber Coolant Valve
ET	External Tank
FDI	Failure Detection and Isolation
FFT	Fast Fourier Transform
FNBP	Fuel Nozzle By-Pass
FP	Fuel Preburner
FPV	Fuel Preburner Valve
GG	Gas Generator
HE	Heat Exchanger
HFR	Heat Flow Rate
HGM	Hot Gas Manifold
HM	Health Monitoring
HPFTP	High Pressure Fuel Turbopump
HPOTP	High Pressure Oxidizer Turbopump
LH	Liquid Hydrogen
LOX	Liquid Oxygen
LPFTP	Low Pressure Fuel Turbopump
LPOTP	Low Pressure Oxidizer Turbopump
MCC	Main Combustor Chamber
MFV	Main Fuel Valve
MOV	Main Oxidizer Valve
OMS	Orbital Maneuvering System
OP	Oxidizer Preburner
OPV	Oxidizer Preburner Valve
RLV	Reusable Launch Vehicle
RPL	Rated Power Level
SRB	Solid Rocket Booster
SSME	Space Shuttle Main Engine
SSTO	Single Stage to Orbit

Appendix B. Steady State Values from the SSME Thermodynamic Model

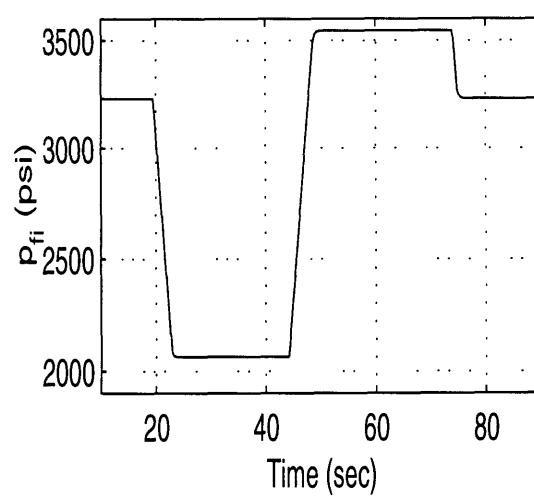
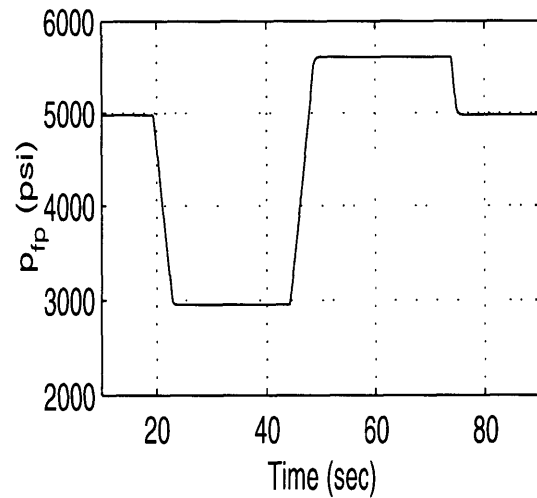
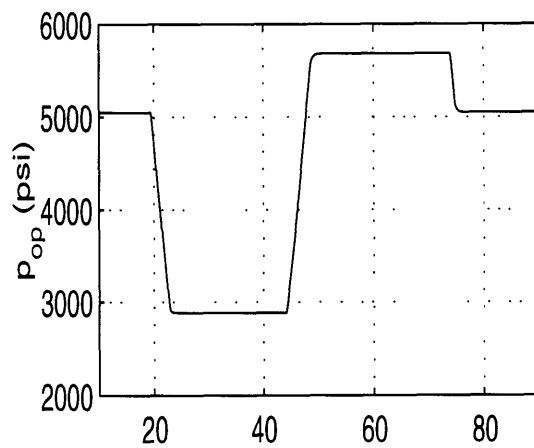
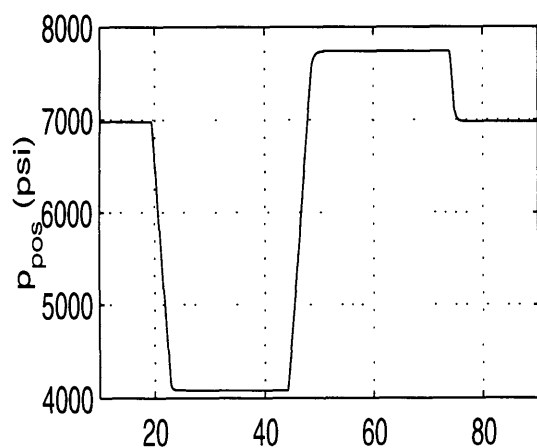
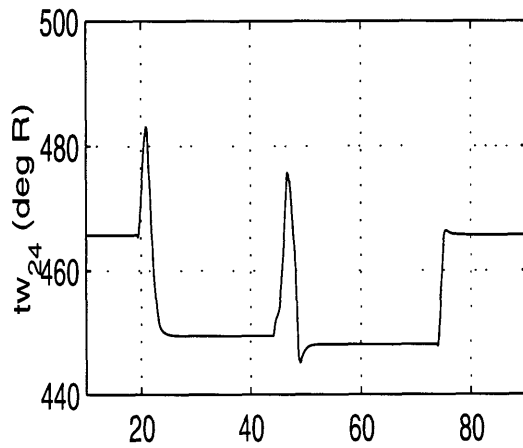
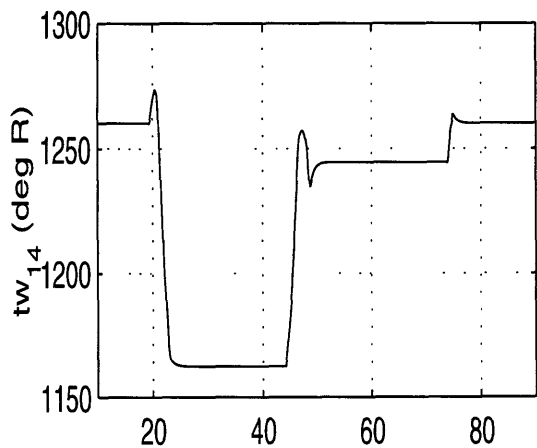
Variable	State	Description	Units	65% RPL	100% RPL	104% RPL	109% RPL
x_fpv	Cntrl	Fuel preburner valve	fraction	0.692	0.782	0.802	0.820
x_opv	Cntrl	Oxidizer preburner valve	fraction	0.543	0.641	0.659	0.683
x_mov	Cntrl	Main oxidizer valve	fraction	1.000	1.000	1.000	1.000
x_mfv	Cntrl	Main fuel valve	fraction	1.000	1.000	1.000	1.000
x_ccv	Cntrl	Coolant control valve	fraction	0.664	1.000	1.000	1.000
omega_f1	X	LPFTP turbine speed	rad/sec	1,491.8	1,634.6	1,671.5	1,722.0
omega_f2	X	HPFTP turbine speed	rad/sec	2,824.3	3,596.6	3,695.6	3,822.2
omega_o1	X	LPOTP turbine speed	rad/sec	419.2	527.5	540.4	556.7
omega_o2	X	HPOTP turbine speed	rad/sec	2,049.3	2,856.6	2,947.0	3,059.0
t_4		Fuel temp. inside nozzle HE	R	449.5	465.8	456.4	448.1
t_5		Fuel temp. inside MCC HE	R	509.0	466.0	455.9	443.1
t_9		Preburners fuel supply line temp.	R	295.4	276.4	276.4	276.5
t_op		Oxidizer preburner temperature	R	1,057.0	1,440.3	1,475.8	1,517.6
t_fp		Fuel preburner temperature	R	1,633.5	1,753.9	1,796.1	1,854.8
t_fi		Fuel injector temperature	R	1,392.7	1,560.7	1,593.1	1,636.2
t_c		Main chamber (MCC) temperature	R	6,400.0	6,400.0	6,400.0	6,400.0
tw_15	X	Hot wall temp. at MCC HE	R	1,228.8	1,214.9	1,203.1	1,187.1
tw_25	X	Cold wall temp. at MCC HE	R	509.0	466.0	455.9	443.1
tw_14	X	Hot wall temp. at nozzle HE	R	1,162.5	1,260.3	1,250.4	1,244.5
tw_24	X	Cold wall temp. at nozzle HE	R	449.5	465.8	456.4	448.1
p_od1		LPOTP discharge pressure	psia	334.5	410.3	418.6	430.4
p_od2		HPOTP discharge pressure	psia	2,440.4	4,110.0	4,314.3	4,573.0
p_od3		HPOTP boost discharge pressure	psia	4,089.5	6,985.3	7,316.2	7,750.8
p_f1		LPFTP discharge pressure	psia	256.1	287.1	296.7	310.0
p_f2		HPFTP discharge pressure	psia	3,910.1	6,095.5	6,415.1	6,834.8
p_pos	X	OP & FP supply line pressure	psia	4,087.6	6,978.7	7,308.6	7,741.8
p_op	X	Oxidizer preburner pressure	psia	2,884.4	5,047.5	5,326.0	5,685.7
p_fp	X	Fuel preburner pressure	psia	2,956.4	4,976.9	5,251.8	5,611.4
p_fi	X	Fuel injector pressure	psia	2,064.1	3,230.0	3,369.1	3,545.3
p_c	X	Main chamber pressure	psia	1,953.9	3,006.0	3,126.2	3,276.5
p_cl	X	Coolant liner pressure	psia	2,094.4	3,277.0	3,419.0	3,599.2
p_4		Nozzle heat exchanger (HE) press.	psia	3,266.1	5,594.1	5,928.9	6,348.7
p_5		MCC heat exchanger pressure	psia	3,008.6	4,675.4	4,904.5	5,202.3
p_9	X	Preburners fuel supply line press.	psia	3,243.4	5,499.6	5,793.6	6,175.1
p_os	X	LPOTP pump inlet pressure	psia	103.5	99.9	99.5	99.0
su_4	X	Fuel sp. int. energy at nozzle HE	Btu/lbm	1,003.5	1,037.3	1,008.5	983.1
su_5	X	Fuel sp. int. energy at MCC HE	Btu/lbm	1,171.8	1,042.0	1,012.5	974.7
dq_14		Hot wall to fuel HFR at nozzle HE	Btu/sec	54,860.5	75,959.7	78,543.1	81,662.9
dq_24		Cold wall to fuel HFR at nozzle HE	Btu/sec	0.362	0.362	-0.362	-0.363
dq_tc4		Hot gas to wall HFR at nozzle HE	Btu/sec	54,859.8	75,959.2	78,543.8	81,663.5
dq_15		Hot wall to fuel HFR at MCC HE	Btu/sec	28,419.2	40,205.2	41,587.3	43,323.0
dq_25		Cold wall to fuel HFR at MCC HE	Btu/sec	0.369	0.367	-0.367	-0.370
dq_tc5		Hot gas to hot wall HFR at MCC HE	Btu/sec	28,418.9	40,204.9	41,587.6	43,323.4
rho_4	X	Fuel density at nozzle HE	lbm/in^3	0.000681	0.001024	0.001089	0.001163
rho_5	X	Fuel density at MCC HE	lbm/in^3	0.000566	0.000889	0.000941	0.001009
dm_ft1		LPFTP turbine flow rate	lbm/sec	18.3	28.4	30.1	32.4
dm_ft2		HPFTP turbine flow rate	lbm/sec	84.3	146.2	153.7	163.2
dm_ot1	X	LPOTP turbine flow rate	lbm/sec	132.8	176.0	180.6	186.3
dm_ot2		HPOTP turbine flow rate	lbm/sec	36.9	58.3	61.0	64.5
dm_fd2		HPFTP pump fuel flow rate	lbm/sec	93.3	144.5	150.3	157.4
dm_op3	X	HPOTP boost pump LOX flow rate	lbm/sec	52.3	96.7	103.1	111.6
dm_fpo	X	Fuel preburner oxidizer flow rate	lbm/sec	36.1	66.5	71.2	77.4
dm_opo	X	Oxidizer preburner LOX flow rate	lbm/sec	11.2	23.3	24.8	26.7
dm_fpf	X	Fuel preburner fuel flow rate	lbm/sec	47.1	78.3	81.1	84.3
dm_opf	X	Oxidizer preburner fuel flow rate	lbm/sec	25.3	34.9	36.1	37.7
dm_mov	X	Main oxidizer valve flow rate	lbm/sec	532.6	802.4	832.3	869.5
dm_fi	X	Main fuel injector flow rate	lbm/sec	128.6	214.7	225.6	239.7
dm_cli	X	Coolant liner inlet flow rate	lbm/sec	0.526	0.655	0.675	0.702
dm_clo	X	Coolant liner outlet flow rate	lbm/sec	0.526	0.655	0.675	0.702
dm_mc	X	MCC heat exchanger fuel flow rate	lbm/sec	18.3	28.4	30.1	32.4
dm_fn	X	Nozzle HE inlet fuel flow rate	lbm/sec	40.6	52.2	55.1	58.3
dm_4	X	Nozzle HE outlet fuel flow rate	lbm/sec	40.6	52.2	55.1	58.3
dm_fnbp	X	Nozzle HE bypass fuel flow rate	lbm/sec	31.8	61.1	62.1	63.7
dm_asifp	X	Fuel preburner ASI flow rate	lbm/sec	0.920	0.969	0.986	1.008
dm_asiofp	X	Oxidizer preburner ASI flow rate	lbm/sec	0.977	0.956	0.972	0.996
dm_asimc	X	MCC ASI flow rate	lbm/sec	0.733	0.915	0.944	0.982
dm_os	X	LPOTP pump inlet flow rate	lbm/sec	584.9	899.1	935.4	981.0
dm_cn		Thrust chamber nozzle flow rate	lbm/sec	662.0	1,017.9	1,058.9	1,110.1

Appendix C.

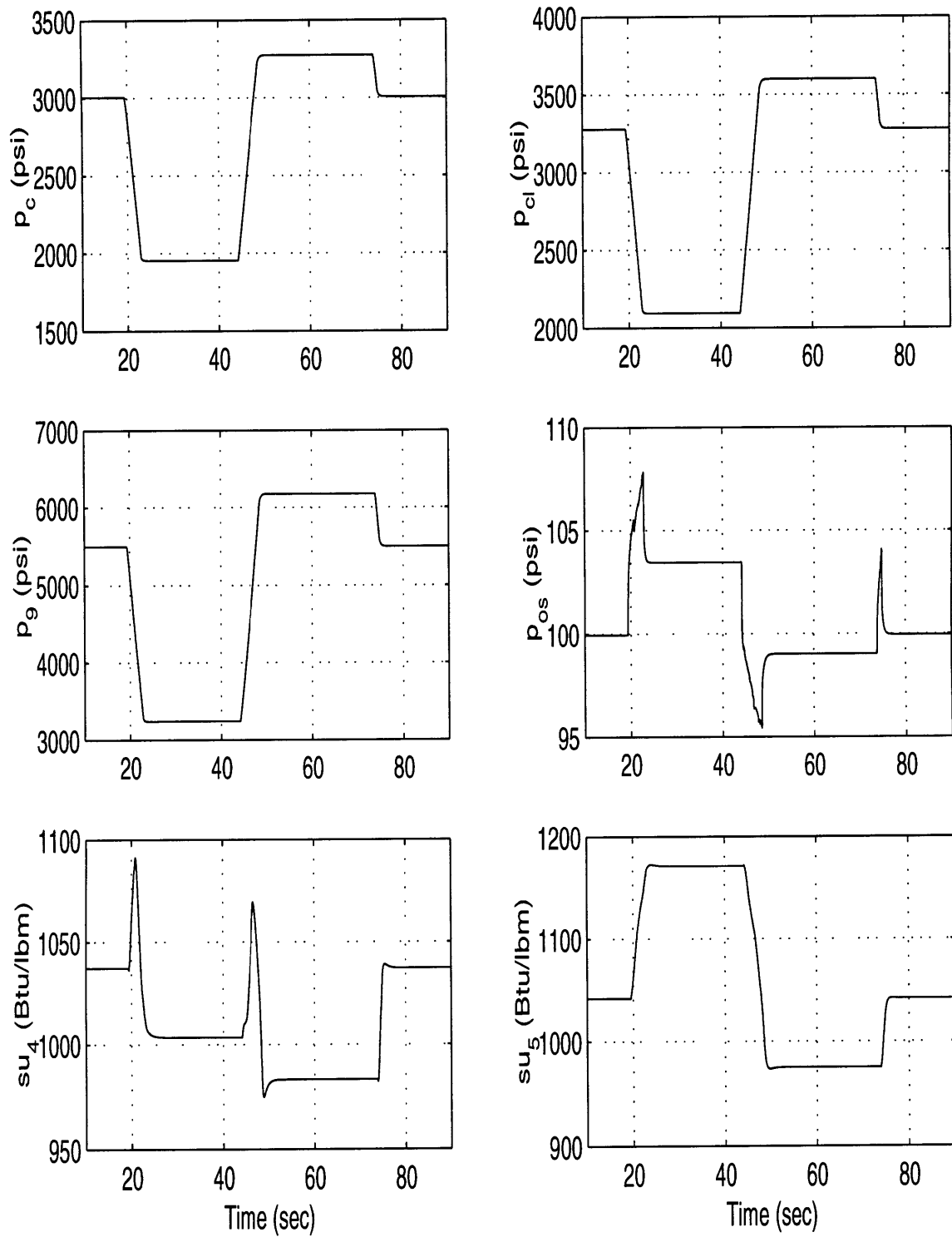
State Variables in a Simulated Throttling Sequence



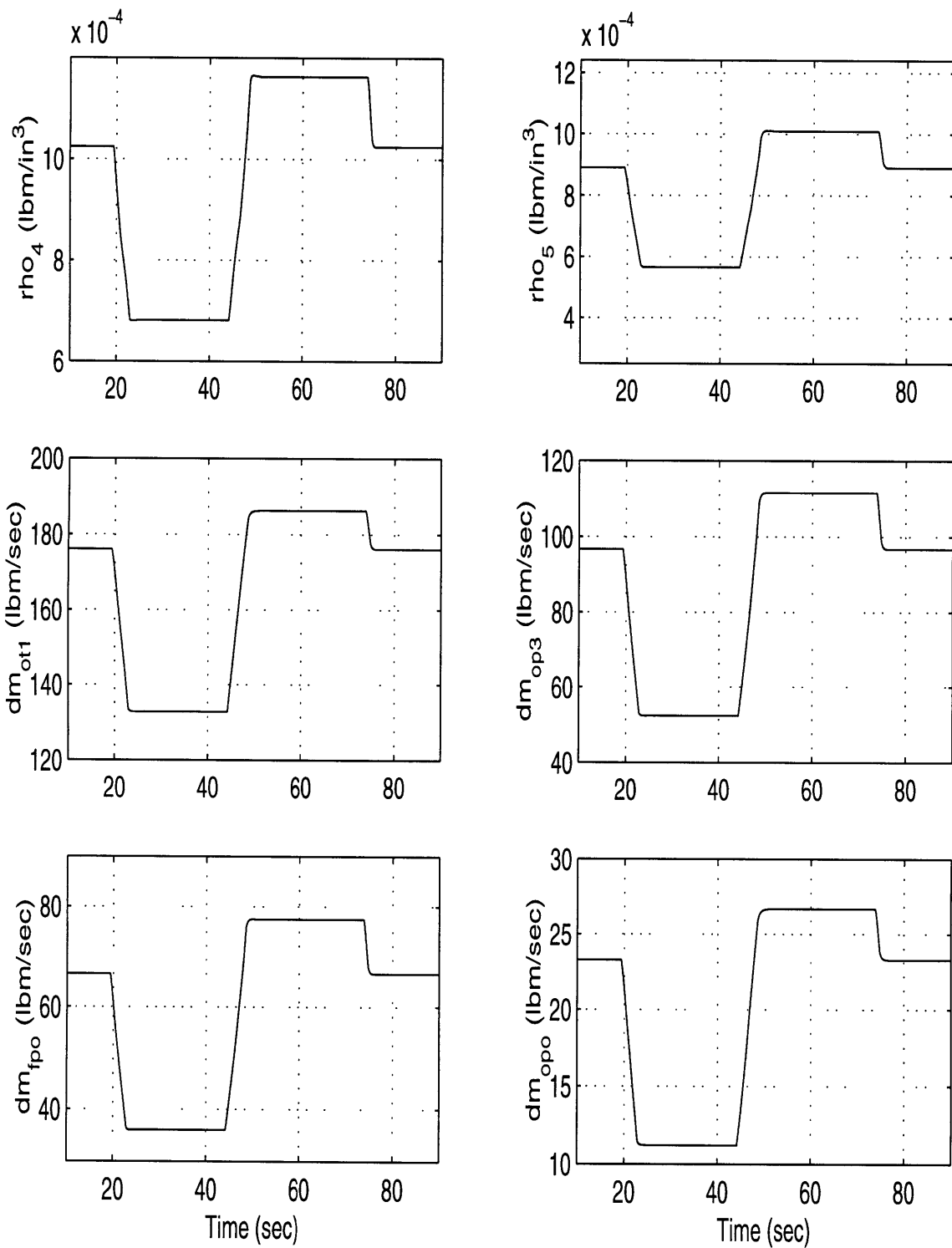
Appendix C. (2)



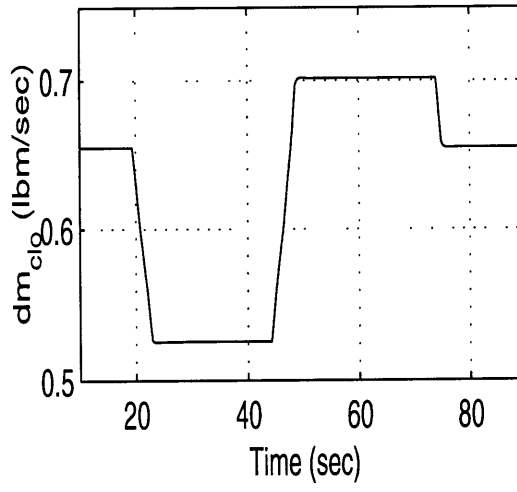
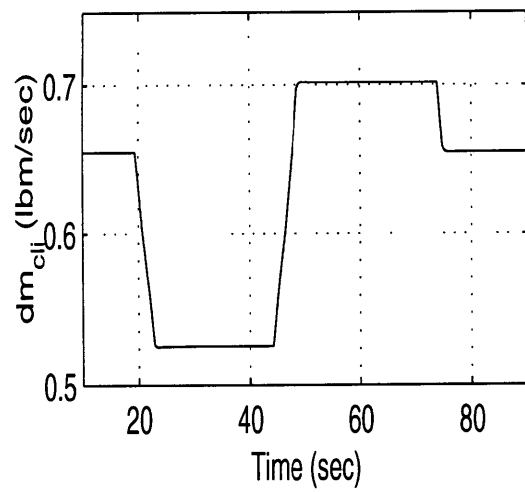
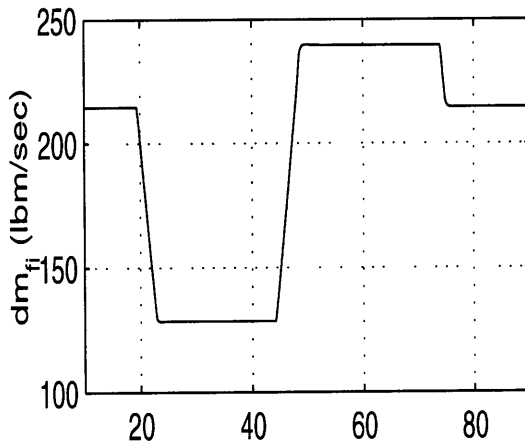
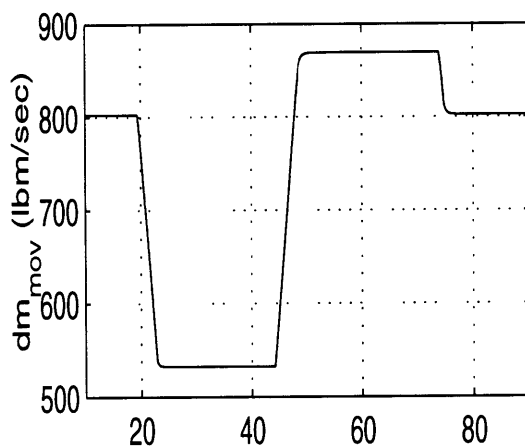
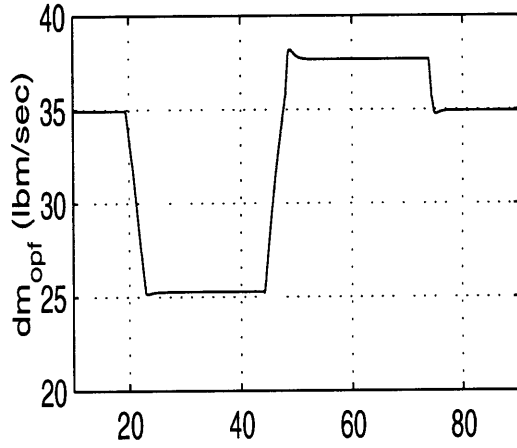
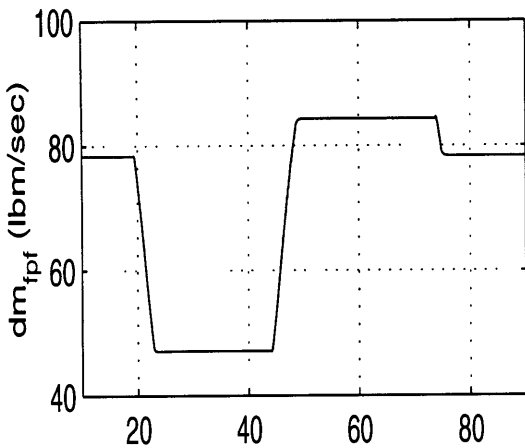
Appendix C. (3)



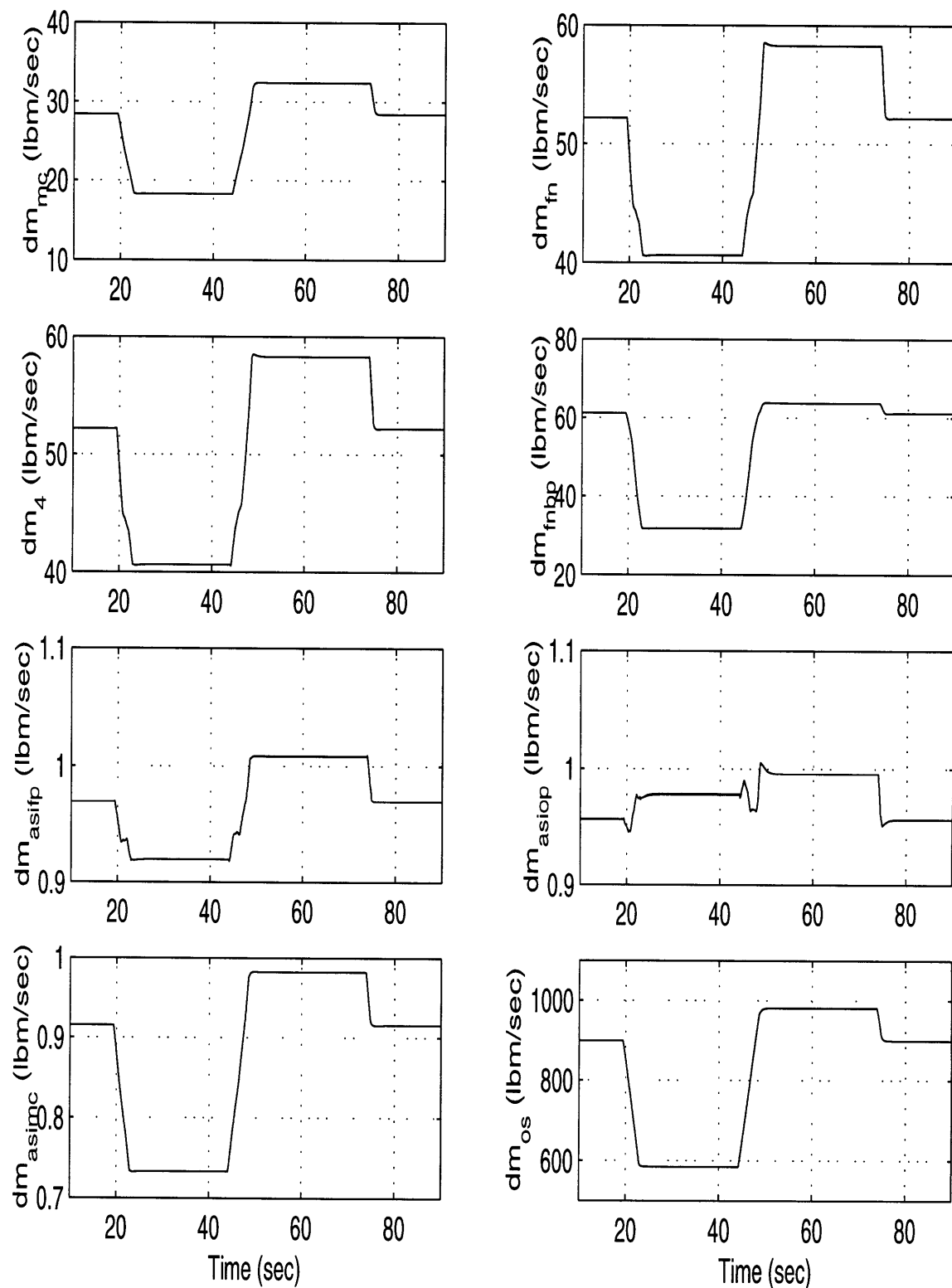
Appendix C. (4)



Appendix C. (5)



Appendix C. (6)



Appendix D. Characteristic Times (approx.) for the SSME Dynamic Model

Variable	Description	Characteristic Time (msec)	Dynamic Category
omega_f1	LPFTP turbine speed	120	very slow
omega_f2	HPFTP turbine speed	105	very slow
omega_o1	LPOTP turbine speed	74.8	very slow
omega_o2	HPOTP turbine speed	57.7	very slow
tw_15	Hot wall temperature at MCC heat exchanger (HE)	98.2	very slow
tw_25	Cold wall temperature at MCC HE	infinite	indeterminate
tw_14	Hot wall temperature at nozzle HE	99.7	very slow
tw_24	Cold wall temperature at nozzle HE	infinite	indeterminate
p_pos	OP & FP LOX supply line pressure	2.0	fast
p_op	Oxidizer preburner pressure	8.5	medium
p_fp	Fuel preburner pressure	2.09	fast
p_fi	Fuel injector pressure	5.0	medium
p_c	Main chamber pressure	0.74	very fast
p_cl	Coolant liner pressure	17.8	slow
p_9	Preburners fuel supply line pressure	4.76	medium
p_os	LPOTP pump inlet pressure	0.75	very fast
su_4	Fuel sp. int. energy at nozzle HE	2.5	fast
su_5	Fuel sp. int. energy at MCC HE	21.1	slow
rho_4	Fuel density at nozzle HE	38.6	slow
rho_5	Fuel density at MCC HE	32.5	slow
dm_ot1	LPOTP turbine flow rate	35.7	slow
dm_op3	HPOTP boost pump LOX flow rate	0.13	very fast
dm_fpo	Fuel preburner oxidizer flow rate	4.82	medium
dm_opo	Oxidizer preburner LOX flow rate	3.36	fast
dm_fpf	Fuel preburner fuel flow rate	0.72	very fast
dm_opf	Oxidizer preburner fuel flow rate	0.64	very fast
dm_mov	Main oxidizer valve flow rate	7.8	medium
dm_fi	Main fuel injector flow rate	20.0	slow
dm_cli	Coolant liner inlet flow rate	1.07	fast
dm_clo	Coolant liner outlet flow rate	1.98	fast
dm_mc	MCC heat exchanger fuel flow rate	0.94	fast
dm_fn	Nozzle HE inlet fuel flow rate	0.59	very fast
dm_4	Nozzle HE outlet fuel flow rate	0.46	very fast
dm_fnbp	Nozzle HE bypass fuel flow rate	51.5	very slow
dm_asifp	Fuel preburner ASI flow rate	1.63	fast
dm_asiop	Oxidizer preburner ASI flow rate	1.59	fast
dm_asimc	MCC ASI flow rate	1.64	fast
dm_os	LPOTP pump inlet flow rate	376.8	extremely slow

Appendix E.

Stability Criteria for the Problem of the Simple Disc

Figure 42 is repeated here for simplicity purposes:

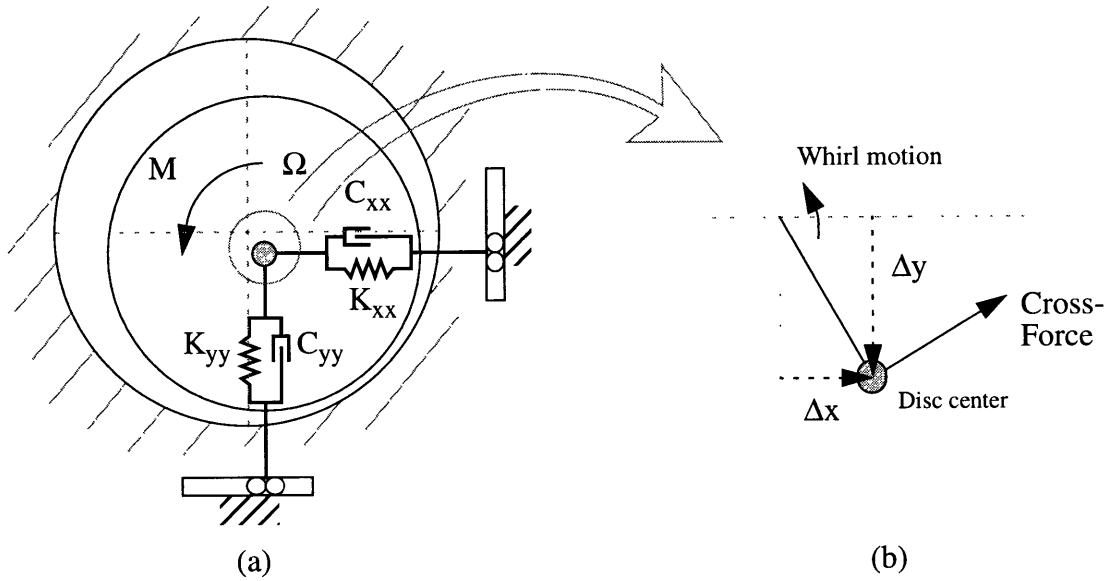


FIGURE 42. Disc Rotating About its Principal Axis (view from the axis)

Clearly this is a two dimensional problem, we need to solve the following coupled system of differential equations

$$M \begin{bmatrix} \ddot{x} \\ \ddot{y} \end{bmatrix} = \begin{bmatrix} -K_{xx} & K_{xy} \\ -K_{xy} & -K_{xx} \end{bmatrix} \begin{bmatrix} x \\ y \end{bmatrix} + \begin{bmatrix} -C_{xx} & C_{xy} \\ -C_{xy} & -C_{xx} \end{bmatrix} \begin{bmatrix} \dot{x} \\ \dot{y} \end{bmatrix} \quad (\text{E.1})$$

Where we have assumed that $K_{xx} = K_{yy}$ and $C_{xx} = C_{yy}$ and due to the disc displacement K_{xy} and C_{xy} appear as cross coupled stiffness and damping coefficients respectively. In order to find the eigenvalues (or normal modes in our problem) of the dynamic system, we take solutions in x and y of the form $\exp[i\omega t]$. Substituting this into (E.1) we find that the resulting determinant should vanish if non-trivial solutions exist for this problem

$$\det \begin{bmatrix} -\omega^2 + \frac{K_{xx}}{M} + i\omega \frac{C_{xx}}{M} & -\frac{K_{xy}}{M} - i\omega \frac{C_{xy}}{M} \\ \frac{K_{xy}}{M} + i\omega \frac{C_{xy}}{M} & -\omega^2 + \frac{K_{xx}}{M} + i\omega \frac{C_{xx}}{M} \end{bmatrix} = 0 \quad (\text{E.2})$$

After solving this determinant we obtain

$$\omega = i \frac{C_{xx}}{2M} \mp \frac{C_{xy}}{2M} \pm \sqrt{\left(-i \frac{C_{xx}}{2M} \pm \frac{C_{xy}}{2M}\right)^2 - \left(\mp i \frac{K_{xy}}{M} - \frac{K_{xx}}{M}\right)} \quad (\text{E.3})$$

Considering the physical picture in which the direct stiffness K_{xx} is the dominant term inside the square root, then we can write (E.3) as

$$\frac{\omega}{\sqrt{K_{xx}/M}} = \pm \left(\pm 1 - \frac{C_{xy}}{2\sqrt{K_{xx}M}} \right) + i \left(\pm \frac{1}{2} \frac{K_{xy}}{K_{xx}} + \frac{C_{xx}}{2\sqrt{K_{xx}M}} \right) \quad (\text{E.4})$$

to first order, as $K_{xx} \gg K_{xy}$ and $K_{xx} \gg \frac{C_{xx}^2}{M}, \frac{C_{xy}^2}{M}$. The plus/minus signs in (E.4) are independent of each other.

We can reformulate the solution of the problem in the following way. Instead of solving a system of two differential equations we can take advantage of the symmetry involved and make the changes of variables

$$z = x + iy \quad \hat{K} = K_{xx} + iK_{xy} \quad \text{and} \quad \hat{C} = C_{xx} + iC_{xy} \quad (\text{E.5})$$

By doing this, the problem reduces to the one of solving a single differential equation

$$M\ddot{z} + \hat{C}\dot{z} + \hat{K}z = 0 \quad (\text{E.6})$$

Once more, assuming solutions of the form $\exp[i\omega t]$ we get the characteristic equation

$$M\omega^2 - i\omega\hat{C} - \hat{K} = 0 \quad (\text{E.7})$$

which can be easily solved to obtain

$$\omega = i \frac{\hat{C}}{2M} \pm \sqrt{-\left(\frac{\hat{C}}{2M}\right)^2 + \frac{\hat{K}}{M}} \quad (\text{E.8})$$

A good interpretation of the results is important to avoid confusions. Substituting back (E.5) into (E.8) we get

$$\omega = i \frac{C_{xx} + iC_{xy}}{2M} \pm \sqrt{-\left(\frac{C_{xx} + iC_{xy}}{2M}\right)^2 + \frac{K_{xx} + iK_{xy}}{M}} \quad (\text{E.9})$$

As in (E.4) we assume K_{xx} to be the dominant quantity, therefore

$$\frac{\omega}{\sqrt{K_{xx}/M}} = \pm 1 - \frac{C_{xy}}{2\sqrt{K_{xx}M}} + i\left(\pm \frac{1}{2} \frac{K_{xy}}{K_{xx}} + \frac{C_{xx}}{2\sqrt{K_{xx}M}}\right) \quad (\text{E.10})$$

Of course, a similar treatment could be used for the independent combination $z^* = x - iy$. The compatibility equation would then be the complex conjugate of (E.6), with solutions where $i\omega$ must be replaced by $(i\omega)^*$:

$$\begin{aligned} \text{therefore as } & (i\omega) = i\omega_R - \omega_I \\ \text{then } & (i\omega)^* = -i\omega_R - \omega_I \end{aligned}$$

The real part of the complex frequency changes its sign, therefore we have that (E.10) should read

$$\frac{\omega}{\sqrt{K_{xx}/M}} = \pm \left(\pm 1 - \frac{C_{xy}}{2\sqrt{K_{xx}M}} \right) + i\left(\pm \frac{1}{2} \frac{K_{xy}}{K_{xx}} + \frac{C_{xx}}{2\sqrt{K_{xx}M}}\right) \quad (\text{E.11})$$

We see that there are four oscillatory solutions, two for forward whirling with slightly different velocity and two for backward whirling. The solution coincides with (E.4).

Now, from (E.4) or (E.11) we observe that the solution contains real and an imaginary parts. From the general form $\exp[i\omega t]$ we see that the real term in (E.11) contributes to the oscillatory solution. On the other hand, the imaginary part yields an exponential behavior which can cause instabilities if its argument's sign results positive. Therefore, stability is maintained as long as

$$\pm K_{xy} > -C_{xx} \sqrt{\frac{K_{xx}}{M}} \quad (\text{E.12})$$

References

- [1] Jackson, Eugene, "SSME Overview", Rockwell International Corporation, Rocketdyne Division, AIAA, 1992
- [2] Jackson, Eugene, "Rocketdyne Turbomachinery", von Karman Institute for Fluid Dynamics, Lecture Series 1993-01: Spacecraft Propulsion
- [3] Hybrid Systems Analysis Unit and System Dynamics Unit, "Engine Balance and Dynamics Model", Rockwell International Corporation, Rocketdyne Division, report number RL00001, January 1992
- [4] Mueller, G. R., "Finite Element Models of the Space Shuttle Main Engine", NASA TM-78260, January 1980
- [5] Martinez-Sanchez M., Jaroux B., Song S.J., and Yoo S., "Measurement of Turbine Blade-Tip Rotordynamic Excitation Forces", ASME Journal of Turbomachinery, Vol. 117, No. 3, July 1995, pp. 384-393
- [6] Glassman, Arthur J., Editor, "Turbine Desing and Application", Scientific and Technical Information Office, National Aeronautics and Space Administration, NASA SP 290, Washington, 1993
- [7] NASA Space Vehicle Design Criteria (Chemical Propulsion), "Liquid Rocket Engine Centrifugal Flow Turbopumps", NASA SP-8109, December 1973
- [8] Munson B.R., Young D.F., and Okiishi T.H., "Fundamentals of Fluid Mechanics", John Wiley & Sons, 1990
- [9] Kerrebrock, Jack L., "Aircraft Engines and Gas Turbines", Second Edition, The MIT Press, Cambridge, MA, 1996
- [10] Sutton, George P., "Rocket Propulsion Elements: An Introduction to the Engineering of Rockets", Sixth Edition, John Wiley & Sons, 1992

- [11] Anderson, John D., "Modern Compressible Flow: With Historical Perspective", McGraw-Hill Book Company, 1982
- [12] McBride B. J. and Gordon S., NASA Program CEA: Chemical Equilibrium with Applications, "Part II: Users Manual and Program Description", NASA RP 1311, 1996
- [13] Bradley, M. A., "SSME Off-Nominal Low Power Level Operation", AAIA Paper 97-2685, Seattle, WA, 1997
- [14] McAdams, William H., "Heat Transmission", McGraw-Hill Book Company, 1954
- [15] McCarty, Robert D., "Hydrogen Technological Survey - Thermophysical Properties", Aerospace Safety Research and Data Institute, NASA Lewis Research Center, NASA SP-3089, 1975
- [16] Childs, Dara W., "Turbomachinery Rotordynamics: Phenomena, Modeling and Analysis", Wiley-Interscience, New York, 1993
- [17] Rao, J.S., "Rotor Dynamics", Wiley, New York, 1991
- [18] Duyar A., Merrill, "Fault Diagnosis for the Space Shuttle Main Engine", Journal of Guidance, Control and Dynamics, Vol. 15, No.2, March-April, 1992, pp. 384-389
- [19] Meyer C., Maul W., Dhawan A., "SSME Parameter Estimation and Model Validity Using Radial Basis Function Networks", Advanced Earth to Orbit Propulsion Technology Conference, May 1994
- [20] Lo F., Wu K., Whitehead A., "Identification and Interpretation of Patterns in Rocket Engine Data", Final Report under NASA Marshall Space Flight Center NAG 8-166, Marshall Flight Center, Al 35812, July 1993
- [21] Jianjun W., Yulin Z., and Qizhi C., "A Real-Time Verification System on Fault Diagnosis Methods for Liquid Propellant Rocket Engine", 32nd AIAA/ASME/SAE/ASEE Joint Propulsion Conference, Lake Buena Vista, Florida, July 1996

- [22] Walker B., and Huang K.Y., "Fault Detection Performance of a FDI Strategy Based on Nonlinear Parameter Estimation for the Space Shuttle Main Engine", presented at the 31st CDC, Tucson, Arizona
- [23] Ho N., Lozano P., Mangoubi R. and Martinez-Sanchez M., "Failure Detection and Isolation for the Space Shuttle Main Engine", AAIA Paper 97-2821, Seattle, WA, 1997
- [24] Cikanek, H.A., "Characteristics of Space Shuttle Main Engine Failures", AIAA-87-1939, San Diego, CA, June, 1987
- [25] Ho, Nhut, "Failure Detection and Isolation for the SSME", SM Thesis, Mechanical Engineering Department, Massachusetts Institute of Technology, May, 1998
- [26] Cikanek H.A., "Space Shuttle Main Engine Failure Detection", American Control Conference, Boston, MA, June, 1985
- [27] Treichler J.R., Johnson C.R., Larimore M.G., "Theory and Design of Adaptive Filters", Topics in digital signal processing, John Wiley & Sons, 1987
- [28] Parsons K.K., "A systems approach to space tourism vehicle development", SM Thesis, Aeronautics and Astronautics Department, Massachusetts Institute of Technology, August, 1997